UNIVERSITY OF OKLAHOMA

GRADUATE COLLEGE

# POLARIMETRIC MEASUREMENTS OF ICE PELLETS AND AGGREGATED SNOW

A DISSERTATION

SUBMITTED TO THE GRADUATE FACULTY

in partial fulfillment of the requirements for the

Degree of

DOCTOR OF PHILOSOPHY

By

PETAR BUKOVČIĆ
Norman, Oklahoma
2017

Downloaded from SHAREOK. Persistent Handle URL: https://hdl.handle.net/11244/52406

POLARIMETRIC MEASUREMENTS OF ICE PELLETS AND AGGREGATED SNOW

A DISSERTATION APPROVED FOR THE
SCHOOL OF METEOROLOGY

BY

_____
Dr. Guifu Zhang, Chair

_____
Dr. Dušan Zrnić, Co-chair

_____
Dr. Alan Shapiro

_____
Dr. Ming Xue

_____
Dr. Yan Zhang

© Copyright by PETAR BUKOVČIĆ 2017
All Rights Reserved.

## Acknowledgements

The greatest appreciation in completing this project goes to my advisors. Dr. Dušan Zrnić was always there to trace the path of this research. When things were not going as smooth as they should, he cheered me up and gave me well-considered and thoughtful points to think about along the way. He readily participated in talks not only about science, but the small things which make life so interesting. While Dr. Zrnić traced the path of the research, Dr. Guifu Zhang built it, providing the insight about leading ideas. He was always available to discuss the meaning of every problem and result, plotting the path forward. Not only did Dr. Zhang provide practical help, he's always been giving me additional dose of confidence when things went well, also giving the encouragement when the work was not going as planed. In the beginning of my studies, there were points in time when I just stared at these professors, listening to their conversations about the ongoing issues and future work, trying to figure out what they were talking about. Now, I'm very happy that my ideas can contribute to these talks.

In addition, my deepest gratitude goes to my Ph.D. committee members: Dr. Alan Shapiro for meaningful comments and suggestions about my work and everyday's life (including the multiple, out of this world, barbeque experiences), Dr. Ming Xue for helpful talks about ongoing issues, and ups and downs in my research, and Dr. Yan (Rockee) Zhang for the provided encouragement and support.

I want to express special thanks to Dr. Alexander Ryzhkov for numerous inspiring discussions about the polarimetric signatures, especially in QVPs, and the potential of polarimetric snow measurements. Not only did he help me understand the

essence of polarimetric “fingerprints” in snow and other precipitation, but he also provided useful ideas which enormously contributed to this research.

My thankfulness also goes to Dr. Pengfei Zhang for polarimetric radar data acquisition, computations, and QVPs processing codes; John Krause for the insights in technical aspects of polarimetric radar data measurements and processing; Dr. Terry Schuur for collecting the KOUN and NSSL disdrometer data; Dr. Valery Melnikov for KOUN calibration; Dr. Richard Doviak for pleasant and enlightening talks.

I would like to express deepest gratitude to Krysta Bruehl, Lauren White, Jo Ann Mehl, Celia Jones, Marcia Palluto, Judy Hendry, Becky Steely, Debbie Barnhill, and Christie Upchurch. They were always ready to talk not only about the administrative work, which was and still is highly confusing but to give a piece of advice how to overcome some challenges from every day’s life.

I’d also like to thank numerous people I’ve worked alongside during the course of my Ph.D. studies. Special thanks goes to Qing Cao for the OU disdrometer data collection, and the help provided concerning the disdrometer operation and data processing, as well as the basics of radar microphysics retrieval. Ben Root, one of my former office-mates and my “programming guru”, brought me up to speed in MATLAB usage and other related things. Without his help, I would hardly know as much about programming as I do now. My colleagues and I can proudly say friends, Jeff Duda and Dan Betten, were and are always there to talk about the classes, research, and everything else going on in our lives. They helped me a lot to understand American culture and the way of living, and for that, I am deeply grateful. I also appreciate all the conversations and encounters I’ve had with the former and current office-mates, Sean

Luchs, Brad Isom, Yinguan Li, Lei Lei, Tim Bonin, Mohammad-Hossein Golbon-Haghighi, Emad Hasan, and Ryan Lagerquist. I want to thank Charlotte Wainwright, Matthew Kumjian, Alex Schenkman, Jeremy Gibbs, Ryan Sobash, Chris Schwarz, Erica Griffin, Jelena Andrić, Igor Ivić, Dragan Nikić, Almedin Čandić, Mirko Ivančić, Danilo Gojković, Tonči Maleta, Jelena Milisavljević, and everyone else who've helped make my graduate school and after hours experience enjoyable and fulfilling.

The most treasured things are always left for the end. I'm deeply grateful for the love and support of my family and friends from Serbia. Norman and Oklahoma are far away from Stubline, Obrenovac, and Beograd (Belgrade) – but further the home, greater the appreciation of and for the family and friends is. Personal thankfulness goes to my dear mom and dad, Snežana and Jovan, family members Sandra Pavlović, Valentina Petrović, Aleksandar Blagojević, Mirjana Popović, Aleksandar and Radovan Bukovčić among many close ones, along with my cherished friends Branko Mitrović, Goran Udovičić, Maja Madžarac, Dejan Nedin, Predrag Sindjić, Djordje Mirković, and especially dear Hristina Nikolić. They are the people that most contributed to who I am today. However, the experience of the graduate school traced the path of who I am going to become.

This work was supported by NOAA/the Office of Oceanic and Atmospheric Research under NOAA-University of Oklahoma Cooperative Agreement NA11OAR4320072, the U.S. Department of Commerce. Additional funding came from the National Science Foundation (grants 1143948 and AGS-1046171) and the Department of Energy grant DE-SC0008811.

# Table of Contents

Acknowledgements ..... iv

Table of Contents ..... vii

List of Tables ..... ix

List of Figures ..... x

Abstract ..... xv

Chapter 1: Introduction ..... 1

Chapter 2: Winter Precipitation Liquid-Ice Phase Transitions Revealed with Polarimetric Radar and Disdrometer Observations in Central Oklahoma ..... 5

1. Introduction ..... 5

2. Dataset and synoptic setting ..... 8

3. Methodology ..... 9

4. Results ..... 16

5. Discussion ..... 39

6. Summary ..... 41

Chapter 3: Polarimetric Relations for Quantification of Snow Based on Disdrometer Data ..... 43

1. Introduction ..... 43

2. Datasets and 2DVD processing ..... 46

3. Methodology ..... 50

4. Parameterization of the *Z*-*S* and *Z*-IWC relations for dry snow ..... 54

5. Disdrometer measurements-estimations and expected values of *S* and IWC ..... 60

6. Discussion ..... 73

7. Summary ..... 76

Chapter 4: Verification of Polarimetric Relations for Snow Quantification with Polarimetric Radar Measurements ..... 79

1. Introduction ..... 79

2. Methodology ..... 79

3. Sensitivity of $S(K_{DP}, Z)$ and IWC($K_{DP}$, $Z$) relations on particle's aspect ratio $b/a$ and the width of the canting angle distribution σ ..... 81

4. Verification of the polarimetric radar relations for snow on polarimetric radar data ..... 84

5. Discussion ..... 96

6. Summary ..... 97

Chapter 5: Summary of Conclusions and Future work ..... 100

References ..... 107

Appendix: Theoretical Relations ..... 116

# List of Tables

Table 3.1: Summary of $Z(S)$ relations for dry snow listed in literature and utilized by the WSR-88D network in the US. ..... 44

# List of Figures

Figure 2.1: $\mu$-$\Lambda$ scatterplot - blue dots are estimated values of $\mu$ and $\Lambda$ from 2DVD measurements using the 2nd, 4th, and 6th moments of the measured distributions during the IP periods (0645 to 1100 UTC, and 1730 to 2130 UTC), whereas red line denotes 2nd degree polynomial data fit during these periods. The black line represents the rain $\mu$-$\Lambda$ relation from Cao et al. (2008). ..... 12

Figure 2.2: Diagram explaining computation of the Slant Vertical Profile and its interpretation. For simplicity, a flat earth is assumed in the sketch whereas in actual computations earth's curvature is accounted for via the 4/3 equivalent radius model. The vertical plane bisects the radar and disdrometer locations. The projection of the conical section over which the data are averaged is at the bottom of the figure. The disdrometer is located at 29 km from the radar, the extent of averaging in azimuth $az_e$-$az_b$ = 20°. In the data interpretation, the band of values 5sin($e_l$) km wide and centered at the height above the disdrometer is examined. ..... 14

Figure 2.3: Comparison of radiosondes and RUC analysis soundings for Norman (OUN) at 0000 (a), 1200 (b), and 1800 (c) UTC. Evolution of temperature (d) and relative humidity (e) profiles over KAEFS. Temperature profiles from RASS soundings Purcell profiler (f) at KAEFS. ..... 17

Figure 2.4: Images of IP and raindrops from 2DVD (not in scale). Typical silhouettes of: (a)-(i) slow-falling IP; (j)-(m) fast-falling IP; and (n)-(o) raindrops. The particles in (c), (i), (l), and (o) are less or equal to 1 mm whereas the other particles dimension is between 1.5 and about 3 mm. The fast particles fall speeds are about the same as those of raindrops. The slow particles fall speeds were between 55 % and 80 % smaller than those of equivalent size raindrops. ..... 20

Figure 2.5: Evolution of: (a) DSD [$\log_{10}(m^{-3}\ mm^{-1})$], (b) mass [$\log_{10}(g\ m^3\ mm^{-1})$], (c) $Z_H$ [$\log_{10}(mm^6\ m^{-3}\ mm^{-1})$], and (d) $Z_{DR}$ [dB] distribution measured with 2DVD; thin black lines denote main ice pellets periods from ~0645 until 1100 UTC and 1730 to 2130 UTC. ..... 21

Figure 2.6: PPI of $Z_H$ (a), $Z_{DR}$ (b) and $\rho_{hv}$ (c) at 0730 UTC and elevation of 0.41°. The magenta colored x represent 2DVD location (KAEFS). The high values of $Z_H$ extending diagonally from NW to SE at about 10 km off the radar is an orographic ridge which in this case shields the disdrometer location from the influence of ground clutter. ..... 23

Figure 2.7: Evolution of enhanced vertical profiles of $Z_H$ (a), $Z_{DR}$ (b) and $\rho_{hv}$ (c) measured with KOUN over 2DVD site. Height is referenced above ground level (AGL). Dashed lines denote RUC analysis temperature profiles above 2DVD location, where black color represent temperature below freezing while magenta above freezing..... 25

Figure 2.8: Evolution of SVPs at 1° elevation of $Z_H$ (a), $Z_{DR}$ (b) and $\rho_{hv}$ (c) from KOUN. The thin black line at ~610 m AGL represent height directly above 2DVD location; the thick black box represents 5 km radial segment along the 1° elevation (height projections) centered on 2DVD location and indicates a period of refreezing. ..... 27

Figure 2.9: Evolution of SVPs at 0° elevation of $Z_H$ (a), $Z_{DR}$ (b) and $\rho_{hv}$ (c) from KOUN. The thin black line at ~100 m AGL represent height directly above 2DVD location; the thick black boxes represent 5 km radial segment along the 0° elevation (height projections) centered on the 2DVD location and indicate periods of refreezing. ..... 28

Figure 2.10: The impact of drops sequential freezing for two different size spectra on (a), (c) $Z_H$ and (b), (d) $Z_{DR}$ for the preferential freezing of small drops. $D_f$ is the largest frozen diameter below which all the drops are frozen for each PSD realization. Computations are for S-band, and Marshall-Palmer DSDs with different rainfall rates $R$ (mm $h^{-1}$) used (blue, green, red, and cyan represent 1, 0.5, 0.3, and 0.1 mm $h^{-1}$, respectively). The discretization of DSD is performed for the two spectral sizes: narrow size NS (top) and wide size WS (bottom) by sorting drops between 0.05 and 2 (4) mm in 40 (80) bins using 0.05 mm increments. Black lines are mean 2DVD PSD measurements from two main ice pellet periods, (a) and (b) from 0645 to 1100 UTC, and (c), (d) are from 1730 to 2130 UTC. ..... 31

Figure 2.11: Comparison of (a) $Z_H$, (b) $Z_{DR}$, (c) rainfall rate, where the ice phase adjustment are in cyan (small dry hail aspect ratio) and green (raindrops aspect ratio) dots for 2DVD, and in blue dotted (small dry hail aspect ratio) and gray dotted (raindrops aspect ratio) line for KOUN, and (d) median volume diameter, obtained from radar DSD retrieval (KOUN) and disdrometer, time series for 0° KOUN elevation angle. Black arrows in (a) represent short periods of relatively big discrepancies between radar and 2DVD characterized as ice pellets. ..... 33

Figure 2.12: Comparison of (a) $Z_H$, (b) $Z_{DR}$, (c) rainfall rate, where the ice phase adjustment are in cyan (small dry hail aspect ratio) and green (raindrops aspect ratio) dots for 2DVD, and in blue dotted (small dry hail aspect ratio) and gray dotted (raindrops aspect ratio) line for KOUN, and (d) median volume diameter, obtained from radar DSD retrieval (KOUN) and disdrometer, time series for 0.41° KOUN elevation angle. Black arrows in (a) represent short periods of relatively big discrepancies between radar and 2DVD characterized as ice pellets. ..... 36

Figure 3.1: Summary of $Z(S)$ relations for dry snow listed in literature and utilized by the WSR-88D network in the US. ..... 44

Figure 3.2: Scatterplot of $N_{0s}$ vs. $S/Z^{0.62}$ ($\log_{10}$ scale, correlation coefficient = 0.978) from 2DVD estimations and computations (blue dots). The best fit to 2DVD data, $S\,Z^{-0.62} = 1.9\,10^{-3}\,N_{0s}^{0.35}$, is overlaid as red line. ..... 55

Figure 3.3: Scatterplot of $N_{0s}$ vs. IWC/$Z^{0.58}$ ($\log_{10}$ scale, correlation coefficient = 0.977) from 2DVD estimations and computations (blue dots). The best fit to 2DVD data, IWC $Z^{-0.58} = 5.26\ 10^{-4}\ N_{0s}^{0.38}$, is overlaid as red line. ..... 56

Figure 3.4: Scatterplots of: a) $N_{0s}$(2DVD) vs. $N_{0s}(K_{DP}, Z)$ ($\log_{10}$ scale, correlation coefficient = 0.971); b) $\Lambda_s$(2DVD) vs. $\Lambda_s(K_{DP}, Z)$ (correlation coefficient = 0.985). ..... 58

Figure 3.5: Scatterplot of IWC vs. $S$ – blue dots represent 2DVD measurements, red and green dots Heymsfield et al. (2016) relations (herein HE16), whereas magenta and black dots represent linear and quadratic least square fit on 2DVD data. Correlation coefficient between 2DVD measured IWC and $S$ is 0.991. ..... 60

Figure 3.6: Scatterplots of $S$(2DVD) vs. $S(Z)$ (green dots), $S$(2DVD) vs. $S(K_{DP})$ (blue dots), $S$(2DVD) vs. $S_{CO}(K_{DP}, Z)$ (black dots, where subscript $_{CO}$ denotes Colorado dataset derived from 6 storms), and $S$(2DVD) vs. $S(K_{DP}, Z)$ (red dots). The correlation coefficients between $S$(2DVD) and $S(Z)$, $S(K_{DP})$, $S_{CO}(K_{DP}, Z)$, and $S(K_{DP}, Z)$ are 0.862, 0.891, 0.995, and 0.995. ..... 62

Figure 3.7: Scatterplot of IWC(2DVD) vs. IWC($Z$) (green dots), IWC(2DVD) vs. IWC($K_{DP}$) (blue dots), IWC(2DVD) vs. $IWC_{CO}(K_{DP}, Z)$ (black dots, where subscript $_{CO}$ denotes Colorado dataset derived from 6 storms), and IWC(2DVD) vs. IWC($K_{DP}$, $Z$) (red dots). The correlation coefficients between IWC(2DVD) and IWC($Z$), IWC($K_{DP}$), $IWC_{CO}(K_{DP}, Z)$, and IWC($K_{DP}$, $Z$) are 0.826, 0.932, 0.988, and 0.989. ..... 63

Figure 3.8: Evolution of a) PSD in $\log_{10}$ scale indicated by the color bar [$\log_{10}(m^{-3}\ mm^{-1})$], where cold to warm color scale represents low to high particle concentrations, b) $Z$, c) $S$(2DVD), $S(K_{DP}, Z)$, and $S_{CO}(Z)$ (blue, red, and green lines), and d) snow accumulations measured by 2DVD, and estimated via $S(K_{DP}, Z)$, and $S_{CO}(Z)$ (blue, red, and green curves), 11 January 2013. ..... 65

Figure 3.9: Scatterplots of $S$(2DVD) vs. $S_{CO}(Z)$ (green dots), $S$(2DVD) vs. $S_{CO}(K_{DP}, Z)$ (blue dots), and $S$(2DVD) vs. $S(K_{DP}, Z)$ (red dots), 11 January 2013. Correlation coefficients between $S$(2DVD) and $S_{CO}(Z)$, $S_{CO}(K_{DP}, Z)$, $S(K_{DP}, Z)$ are 0.833, 0.983, and 0.983. ..... 67

Figure 3.10: As in Figure 8, but for 28 January 2013. ..... 68

Figure 3.11: Scatterplots of $S$(2DVD) vs. $S_{CO}(Z)$ (green dots), $S$(2DVD) vs. $S_{CO}(K_{DP}, Z)$ (blue dots), and $S$(2DVD) vs. $S(K_{DP}, Z)$ (red dots), 28 January 2013. Correlation coefficients between $S$(2DVD) and $S_{CO}(Z)$, $S_{CO}(K_{DP}, Z)$, $S(K_{DP}, Z)$ are 0.796, 0.987, and 0.987. ..... 69

Figure 3.12: Evolution of a) PSD in $\log_{10}$ scale indicated by the color bar [$\log_{10}(m^{-3} mm^{-1})$], where cold to warm color scale represents low to high particle concentrations, b) $Z$, c) $S$(2DVD), $S(K_{DP}, Z)$, and $S_{et}(Z)$ (blue, red, and green lines), and d) snow accumulations measured by 2DVD, and estimated via $S(K_{DP}, Z)$, and $S_{et}(Z)$ (blue, red, and green curves), 25 February 2012. ..... 71

Figure 3.13: Scatterplots of $S$(2DVD) vs. $S_{et}(Z)$ (green dots), $S$(2DVD) vs. $S_{et}(K_{DP}, Z)$ (blue dots), and $S$(2DVD) vs. $S(K_{DP}, Z)$ (red dots), 25 February 2012. Correlation coefficients between $S$(2DVD) and $S_{et}(Z)$, $S_{et}(K_{DP}, Z)$, $S(K_{DP}, Z)$ are 0.825, 0.993, and 0.988. ..... 72

Figure 3.14: Dependence of $L_b - L_a$ on the aspect ratio of oblate spheroids. ..... 74

Figure 4.1: Dependence of the particle's aspect ratio on radar elevation angle (for $\sigma = 0°$ and <canting angle> = 0°, where symbol < > represent mean). Blue, green, red, cyan, and magenta lines represent the change in the apparent aspect ratio $(b/a)_\theta$ = 0.55, 0.6, 0.65, 0.7, and 0.75 for different radar elevation angles, from 0° to 30°. ..... 81

Figure 4.2: Dependence of the $K_{DP}$ exponents $\alpha_1$ and $\alpha_2$ in a) $S(K_{DP}, Z)$ and b) IWC($K_{DP}$, $Z$) on $\sigma$ and $b/a$, computed from 2DVD measurements. ..... 82

Figure 4.3: Dependence of the $Z$ exponents $\beta_1$ and $\beta_2$ in a) $S(K_{DP}, Z)$ and b) IWC($K_{DP}$, $Z$) on $\sigma$ and $b/a$, computed from 2DVD measurements. ..... 83

Figure 4.4: Dependence of the a) $S(K_{DP}, Z)$ and b) IWC($K_{DP}$, $Z$) relations' multipliers $\gamma_1$ and $\gamma_2$ on $\sigma$ and $b/a$, computed from 2DVD measurements. ..... 83

Figure 4.5: QVPs of a) Z in dBZ, b) $K_{DP}$ in deg km$^{-1}$, c) $Z_{DR}$ in dB, and d) S($K_{DP}$, Z) in mm h$^{-1}$, KLWX 19.5° radar elevation angle, Sterling VA, 23 January 2016. The black dashed lines are isotherms, where the layer from -10°C to -20°C highlighted in magenta represents DGL. ..... 85

Figure 4.6: Vertical profiles of total snow accumulation obtained from KLWX 19.5° QVPs using various $S(Z)$s and $S(K_{DP}, Z)$ relations (red: aspect ratio – ar = $(b/a)_{0°}$ = 0.65, magenta: apparent aspect ratio – ap = $(b/a)_{19.5°}$ = 0.6, obtained from $(b/a)_{0°}$ = 0.55 via Eq. 4.1) for 23 January 2016. The X represents reference ground measurements of snow liquid-water equivalent presented at the lowest snowfall accumulation height for convenience. ..... 87

Figure 4.7: QVPs of a) $Z$ in dBZ, b) $K_{DP}$ in deg km$^{-1}$, c) $Z_{DR}$ in dB, and d) S($K_{DP}$, $Z$) in mm h$^{-1}$, KOUN 19.5° radar elevation angle, Norman OK, 1 February 2011. The black dashed lines are isotherms, where the layer from -10°C to -20°C highlighted in magenta represents DGL. ..... 90

Figure 4.8: QVPs of a) SNR (dB) and b) spectrum width SW (m s$^{-1}$) from 19.5° elevation, KOUN, 1 February 2011. The threshold of 20 dB in SNR is applied to SW. 91

Figure 4.9: Vertical profiles of total snow liquid-water equivalent accumulation obtained from KOUN 19.5° QVPs using various $S(Z)$s and $S(K_{DP}, Z)$ relations (red: aspect ratio – ar = $(b/a)_{0°} = 0.65$, magenta: apparent aspect ratio – ap = $(b/a)_{19.5°} = 0.6$, obtained from $(b/a)_{0°} = 0.55$ via Eq. 4.1) for 1 February 2011. The X represents reference ground measurements of snow liquid-water equivalent from Oklahoma Mesonet, whereas Δ is the estimate form the average snow depth measured by ruler across Norman, OK, using the 10:1 conversion rule, presented at the lowest snowfall accumulation height for convenience. Red and magenta asterisks are $S(K_{DP}, Z)$ estimates using aspect ratios of 0.65 and 0.6 respectively, but from DGL (-10°C to -20°C). ..... 92

Figure 4.10: Instantaneous snowfall rate from heated rain gauge (dashed cyan line), 2DVD (blue line), $S_{CO}(K_{DP}, Z)$ (red line) and $S(Z)$ (green line) relations; 28 January 2013, Grand Mesa, CO. ..... 94

Figure 4.11: SWE accumulations from heated rain gauge (cyan line), 2DVD (blue line), $S_{CO}(K_{DP}, Z)$ (red line), $S(K_{DP}, Z)$ (black line), and $S(Z)$ (green line) relations; 28 January 2013, Grand Mesa, CO. ..... 95

# Abstract

The recent upgrade of the National Weather Service WSR-88D radar network to polarimetric capabilities provides the abundance of information about the precipitation microphysics. Even with the plethora of polarimetric measurements at our disposal, use of this essential information regarding the microphysical processes is underutilized. For example, there is no polarimetric relation for snow estimation. The focus of this study is to improve the existing state of polarimetric data usage for discrimination between the ice pellets and freezing rain if their occurrence is away from the radar (patchy, no radar-centric structure), and more importantly the development of the polarimetric relations for snow quantification.

Observations and analysis of an ice-liquid phase precipitation event, collected with an S-band polarimetric KOUN radar and a two-dimensional video disdrometer in central Oklahoma are presented. Using the disdrometer measurements, precipitation is classified either as ice pellets or rain/freezing rain. The ice pellets were challenging to detect by looking at conventional polarimetric radar data due to the localized and patchy nature of the ice phase and occurrence close to the ground. In this study, a new, unconventional way of looking at polarimetric radar data is introduced: Slanted Vertical Profiles SVPs at low (0° - 1°) radar elevations. From the analysis of the localized and patchy structures using SVPs, the polarimetric refreezing signature, reflected in local enhancement in $Z_{DR}$ and reduction in $Z_H$ and $\rho_{hv}$, became much more evident. Model simulations of sequential drop freezing using Marshal-Palmer DSDs along with the disdrometer observations suggest that preferential freezing of small drops may be responsible for the refreezing polarimetric signature.

Accurate measurements of snow amounts by radar are very difficult to achieve. The inherent uncertainty in radar snow estimates based on the radar reflectivity factor $Z$ is caused by the variability of snow particle size distributions and snow particle density as well as large diversity of snow growth habits. In this study, a novel methodology for snow quantification based on the joint use of radar reflectivity $Z$ and specific differential phase $K_{DP}$ is introduced. An extensive dataset of 2D video disdrometer measurements of aggregated snow in central Oklahoma is used to derive polarimetric relations for liquid-equivalent snowfall rate $S$ and ice water content IWC in the forms of bivariate power-law relations $S = \gamma_1 K_{DP}^{\alpha_1} Z^{\beta_1}$ and $\mathrm{IWC} = \gamma_2 K_{DP}^{\alpha_2} Z^{\beta_2}$. The physical basis of these relations is explained. Their multipliers are sensitive to variations in the width of the canting angle distribution, and to lesser extent particles' aspect ratios and densities, whereas the exponents are practically invariant. This novel approach is tested against the $S(Z)$ relation using snow disdrometer measurements in three geographical regions (Oklahoma, Colorado, and Canada). Similarly, the new approach is tested on polarimetric radar data at three localities, Oklahoma, Virginia, and Colorado. Polarimetric relations for snow quantification demonstrated significant improvement in snow estimates compared to the traditional $Z$-based methods.

# Chapter 1: Introduction

Several, if not all types of winter precipitation can be very disruptive and have tremendous hazardous effect on the society and everyday's life. Oftentimes, the winter precipitation influence is extended in space and time, depending on storm's severity and havoc it created. At least two-thirds of continental United States is affected by winter precipitation. Thus, it is of high importance to accurately represent microphysical processes in winter storms to be able to mitigate adverse impacts on human lives and associated property damage. There are several studies (Martner et al. 1992, Stewart 1992; Rauber et al. 1994, Cortinas 2000, Cortinas et al. 2004) that describe the multiple levels of destruction caused by the winter storms, and emphasize the importance of more accurate measurements and predictions of such events. With the recent conversion of NWS WSR-88D radars to polarimetric capabilities, the potential for measurements of winter precipitation microphysics is tremendously increased. Nowadays, because of the engagement of the widespread polarimetric radar network across the US and other countries, the prospect of more accurate measurements of winter hazardous weather is more appealing than ever.

Some precipitation, such as freezing rain or heavy snow, is more hazardous than other. Because of complex microphysics involved in the process of precipitation formation (Zerr 1997), freezing rain is often accompanied by less perilous ice pellets. Small changes in environmental conditions can substantially alter precipitation type from ice pellets to freezing rain (or snow) (Ryzhkov et al. 2011a). This is mainly because freezing rain is formed by melting of snow particles in and below the melting layer (the layer with temperatures above freezing), which fall through the subfreezing

layer below, and freeze on the contact with the ground. If the subfreezing layer is deep and cold enough, the partial or full refreezing from liquid (freezing) rain to solid ice pellets occurs. It is not uncommon that ice pellets and freezing rain coexist, or fall exclusively, depending on storm microphysics (Stewart 1992). Thus, it is very important to distinguish between these two types of precipitation because of their different effect on society and day to day life. Also, it is important for the aviation safety to distinguish between very dangerous freezing rain and less disruptive ice pellets. In the first part of this study the novel method for discrimination of ice pellets from freezing rain, using Slanted Vertical Profiles (SVPs) of polarimetric variables ($Z_H$, $Z_{DR}$, and $\rho_{hv}$) at lowest few radar elevations, is developed. The SVP methodology is applicable on patchy and localized ice pellets occurrence, at some distance (usually 20 – 60 km) away from radar.

Snow estimations with standard $S(Z)$ radar relations are highly unreliable. Even the ground measurements of snow liquid-water equivalent $S$ are oftentimes unsatisfactory. Snowpack accumulation in winter season has a huge impact on a total water accumulation in water reservoirs in spring, and even summer. It is of great importance for water management facilities to accurately estimate the amount of water from melted snow. Heavy snow has a horrendous impact on traffic, whereas human-made structures are often under a lot of stress due to high snow accumulations (Stewart 1992). The blizzard conditions can completely shut down electricity, water and food supply, traffic, services, etc., in storm-affected areas. Even though radar polarimetry is present for more than 40 years, not much work on polarimetric snow estimation is done. The radar algorithms are still using the standard $S(Z)$ relations, which are very

unreliable for snow estimation. There have been some attempts to estimate ice water content IWC from radar polarimetric variables (Vivekanandan et al. 1994, Aydin and Tang 1995, Ryzhkov et al. 1998), but not *S*. In the second (larger) part of this study a novel approach for estimation of aggregated snow is proposed. Polarimetric relations for *S* and IWC in the form of bivariate power-laws, $S = \gamma_1 K_{\mathrm{DP}}^{\alpha_1} Z^{\beta_1}$ and $\mathrm{IWC} = \gamma_2 K_{\mathrm{DP}}^{\alpha_2} Z^{\beta_2}$, are derived from a large disdrometer snow data set, collected in Oklahoma from 2006 until 2015. These relations are verified in three different regions (Colorado, Ontario, and Oklahoma) with corresponding disdrometer (2DVD) data and three localities (Virginia, Colorado, and Oklahoma) with polarimetric radar data using Quasi Vertical Profiles QVP (Ryzhkov et al. 2016) and plan position indicator (PPI) methodology.

The dissertation begins with a short description of winter precipitation impact, especially ice pellets and snow, on society and everyday's life, and the goals of the study are related to the prospective of previous work in the field. It continues (Chapter 2, which is the exact replica of Bukovčić et al. 2017a published in JAMC) with a portrayal of the method for discrimination of ice pellets from freezing rain in localized, patchy area 20 to 60 km away from radar, using the Slanted Vertical Profiles (SVPs) of polarimetric variables $Z_{\mathrm{H}}$, $Z_{\mathrm{DR}}$, and $\rho_{\mathrm{hv}}$ at low radar elevations. Chapter 3 is almost identical replica (except for two added and three allocated paragraphs to Chapter 4) of a text from a research paper accepted for publication in JAMC (Bukovčić et al. 2017b) in which polarimetric relations for estimation of *S* and IWC are developed from 2DVD data. The relations, which are valid for dry, aggregated snow, are derived from 16 Oklahoma snow storms, presented in forms of bivariate power-laws. Their output is verified with the disdrometer datasets from three geographical regions, Colorado,

Ontario, and Oklahoma. In Chapter 4 the novel polarimetric relations for snow estimation (developed in Chapter 3) are tested on polarimetric radar data from three localities, Virginia, Colorado, and Oklahoma. Chapter 5 provides overall summary of the dissertation and future work. Appendix includes the parameterization of the $S(Z)$ and IWC($Z$) relations with the intercept parameter of the exponential distribution $N_{0s}$. Chapters 2 and 3 are derived from published (or accepted – Chapter 3) papers, with Chapter 4 as radar-based verification of Chapter 3, and thus, structured to be self-contained. These chapters have their own introductory (background), methodology, summary, and conclusions.

# Chapter 2: Winter Precipitation Liquid-Ice Phase Transitions Revealed with Polarimetric Radar and Disdrometer Observations in Central Oklahoma

## 1. Introduction

While investigations of rain events are numerous (Goddard et al. 1982; Ulbrich 1983; Tokay and Short 1996; Atlas et al. 1999; Schuur et al. 2001; Zhang et al. 2001, 2003, 2006, 2008; Bringi et al. 2003; Brandes et al. 2004a, b; Thurai et al. 2007, 2014; Cao et al. 2008; Niu et al. 2010; Tao et al. 2010; Islam et al. 2012; Williams et al. 2014; Bukovčić et al. 2015), winter precipitation has been studied considerably less, especially transitions between the liquid and snow/ice phases (Raga et al. 1991; Trapp et al. 2001; Cortinas et al. 2004; Ikeda et al. 2005a, b; Yuter et al. 2006, 2008; Brandes et al. 2007; Ryzhkov et al. 2008; Zhang et al. 2011).

Even though ice pellets (IP) are considered less hazardous than snow or freezing rain, they are very important. Relatively small changes in environmental conditions can dramatically alter precipitation type from ice pellets to freezing rain or snow (Ryzhkov et al. 2011a). In recent years there has been an increase in interest regarding the characteristics and microphysical properties of ice pellets. Gibson and Stewart (2007) used a high-resolution digital camera to photograph and classify IP into several categories during a winter storm in Mirabel: bulged particles, particles with spicules, spherical particles, nearly spherical particles, and irregular particles. Gibson et al. (2009) investigated the microphysical and statistical properties of ice pellets in the Montreal area using the images from a high-resolution digital camera. Kumjian and Schenkman (2014) presented an analysis of a curious case of ice pellets over central

Tennessee. Despite the fact that the surface temperatures were >10°C and the lowest ~2 km of the atmosphere was entirely above freezing, ice pellets were reported on the ground. They found that the evaporation of raindrops substantially cooled the surrounding air towards its wet bulb temperature ($T_w$), well below 0°C. This was sufficiently cold for the freezing of subsequent raindrops, which fell to the ground without significant melting or sublimation. Nagumo and Fujiyoshi (2015) investigated microphysical properties of slow-falling and fast-falling ice pellets using 2DVD. They associated slow-falling IP with uniform and rapid freezing in the cold and dry layer with $T_w \sim$ -4°C. The fast-falling IP showed similarity to the ice particles with a smooth wet surface and exhibited falling velocities close to those of raindrops. Hence, fast-falling ice pellets froze slowly through contact with splinters (or ice crystals) generated by preceding slow-falling ice pellets in a relatively warm layer.

Ryzhkov et al. (2011a) and Kumjian et al. (2013) are two studies which are closely related to this research. Ryzhkov et al. (2011a) investigated polarimetric radar signatures in winter storms and their relation to aircraft icing and freezing rain; it is rather difficult to predict or even detect the transition between very disruptive freezing rain and much less hazardous ice pellets. One of the main conclusions of the study is that in the case of refreezing (i.e., IP formation) differential reflectivity ($Z_{DR}$) is locally increasing rather than decreasing, which is the opposite of what was initially expected; horizontal reflectivity ($Z_H$) and copolar correlation coefficient ($\rho_{hv}$) locally decrease in transition from rain to ice pellets ($Z_H$ due to change in complex dielectric factor and $\rho_{hv}$ due to differences in particle shapes, compositions, and canting angles at refreezing levels). Kumjian et al. (2013) conducted a study of polarimetric radar measurement

fingerprints in winter storms that produce ice pellets. These unique refreezing fingerprints, observed within the low-level subfreezing layer, consist of enhancement in $Z_{DR}$ and specific differential phase ($K_{DP}$) and decrease in $Z_H$ and $\rho_{hv.}$ They proposed that the unique polarimetric signature of refreezing is caused either by preferential freezing of small drops or local ice generation and suggested that the validity of these hypotheses be further explored.

The shapes in the PPI plots of the reported refreezing signatures by Ryzhkov et al. (2011a) and Kumjian et al. (2013) are rings of change in polarimetric variables below the melting layer and centered on the radar. Such rings close to the radar are readily identified at high elevation scans due to enhanced vertical resolution and continuity in azimuth. Thus, the signatures are well suited for discrimination between freezing rain and ice pellets in operational environments. Herein we report the polarimetric observation of ice pellets in a localized area about 30-40 km away from the radar where poorer resolution and small spatial extent challenge identification and interpretation. However, benefiting from the previous observations, a collocated 2DVD, and other measurements, we are able not only to confirm the signatures but also to quantify the amount of frozen precipitation.

In this study, we jointly use polarimetric radar data and 2DVD measurements to uncover important precipitation microphysics properties in the transition from rain to ice pellets and vice versa. A novel way of presenting polarimetric data in quasi-vertical profiles (QVPs) from azimuthal averages (Ryzhkov et al. 2016) is expanded to generate Slanted Vertical Profiles (SVPs), which help understand the transition precipitation

microphysics. Also, the discrepancies between radar-retrieved microphysical parameters and those obtained from 2DVD measurements are explained.

In section 2, the data acquisition, processing, and synoptic setting are explained, while in section 3 the methodology and theoretical basis are presented. The main results of the study, as well as comparisons with the findings of Ryzhkov et al. (2011a) and Kumjian et al. (2013), are in section 4. The discussion and implications of our findings are in section 5, while the summary is in section 6.

## 2. Dataset and synoptic setting

Observation data of a winter storm event on 20 January 2007 were collected with the S-band polarimetric KOUN radar and the University of Oklahoma (OU) 2DVD in central Oklahoma. The case is classified as a wintery mix of ice pellets, freezing rain, and rain periods. The disdrometer was deployed at Kessler's Atmospheric and Ecological Field Station (KAEFS), an OU test site approximately 29 km and 191.4° azimuth from KOUN, at ~345 meters above sea level. Disdrometer measured Drop Size Distributions (DSDs – for raindrops) or Particle Size Distributions (PSDs – for hydrometeors other than rain) are sampled over 1-minute intervals.

On this day, an upper-level, low-pressure system approached the area from the southwest, passing to the northeast. The event started at about 0540 UTC, with light stratiform rain over the disdrometer site, changing into periods of ice pellets (IP) from ~0645 to 1100 UTC and from ~1730 to 2130 UTC, called herein the primary and secondary ice pellet periods (see section 4*b* for detailed analysis). In general, the transition was caused by a warm layer of air at ~2200 m above the ground and a

freezing layer below the warm layer extending to the ground, making environmental conditions favorable for ice pellet formation; the structure of the melting/refreezing layers is more complex and described in section 4*a*. Precipitation was mainly freezing rain or rain with a few short transitions to ice/mixed phase between the primary and secondary ice pellet periods. Near the end of the event, from 2200 until 2330 UTC, precipitation changed from IP/mixed phase to snow.

## 3. Methodology

The fundamental information associated with rain microphysics is contained in raindrop size distributions. DSDs are readily measured with 2DVDs, but only at one location. Various microphysical parameters, such as median volume diameter ($D_0$, mm) and rainfall rate ($R$, mm $h^{-1}$), can be calculated from DSDs obtained from 2DVD measurements:

$$\int_0^{D_0} D^3 N(D)\, dD = \int_{D_0}^{\infty} D^3 N(D)\, dD, \tag{2.1}$$

$$R = 10\pi \sum_{i=1}^{L} \frac{C(D_i) D_i^3}{A(D_i)}, \tag{2.2}$$

where the term $C(D_i)$ represents the number of particles, $A(D_i)$ is the mean measured sensor (2DVD) effective area in $mm^2$ for the size bin i, and $D_i$ is the equivolume diameter representing the bin center (also denoted as $D$ subsequently) in mm, while $N(D)$ is measured drop size distribution in $m^{-3}$ $mm^{-1}$. If the ice phase is assumed instead of liquid precipitation, the rainfall rate becomes the ice pellet equivalent liquid fall rate $R_{ip}$ in mm $h^{-1}$:

$$R_{\mathrm{ip}} = 10\pi \frac{\rho_{\mathrm{ice}}}{\rho_{\mathrm{w}}} \sum_{\mathrm{i}=1}^{L} \frac{C(D_{\mathrm{i}}) D_{\mathrm{i}}^3}{A(D_{\mathrm{i}})}, \tag{2.3}$$

where $\rho_{\mathrm{ice}} = 0.917$ g cm$^{-3}$ is the density of ice, and $\rho_{\mathrm{w}}$ is the density of water.

Integral parameters calculated from 2DVD measurements for liquid precipitation, reflectivity factor ($Z_{\mathrm{h,v}}$ in mm$^6$ m$^{-3}$, $Z_{\mathrm{H,V}}$ is in dBZ; Doviak and Zrnić, 1993), differential reflectivity ($Z_{\mathrm{DR}}$, dB), and copolar correlation coefficient $\rho_{\mathrm{hv}}$ are defined as

$$Z_{\mathrm{h,v}} = \frac{4\lambda^4}{\pi^4 \left|K_{\mathrm{W}}\right|^2} \int_{D_{\min}}^{D_{\max}} \left|s_{\mathrm{h,v}}(\pi, D)\right|^2 N(D)\, dD, \tag{2.4}$$

$$Z_{\mathrm{H,V}} = 10 \log_{10}\left(Z_{\mathrm{h,v}}\right), \tag{2.5}$$

$$Z_{\mathrm{DR}} = 10 \log_{10}\left(\frac{Z_{\mathrm{h}}}{Z_{\mathrm{v}}}\right), \tag{2.6}$$

$$\rho_{\mathrm{hv}} = \frac{\left|\int_{D_{\min}}^{D_{\max}} s_{\mathrm{v}}(\pi, D)\, s_{\mathrm{h}}^*(\pi, D)\, N(D)\, dD\right|}{\sqrt{\int_{D_{\min}}^{D_{\max}} \left|s_{\mathrm{v}}(\pi, D)\right|^2 N(D)\, dD \int_{D_{\min}}^{D_{\max}} \left|s_{\mathrm{h}}(\pi, D)\right|^2 N(D)\, dD}}. \tag{2.7}$$

Backscattering amplitudes obtained from T-matrix calculations are represented by $s_{\mathrm{h,v}}(\pi, D)$; the conjugate is indicated by $^*$, and indices h and v denote horizontal and vertical polarization. Scattering amplitudes of ice pellets are calculated using Rayleigh-Gans approximation where the dry graupel/hail axis aspect ratio (Ryzhkov et al. 2011b) is

$$r_{\mathrm{dh}} = 1 - 0.02D. \tag{2.8}$$

In the case of raindrops, the axis ratio (Brandes et al. 2002; Zhang 2016)

$$r_{\mathrm{w}} = 0.9951 + 0.0251D - 0.03644D^2 + 0.005303D^3 - 0.0002492D^4, \tag{2.9}$$

is assumed for retrievals and comparisons.

Polarimetric radar data can be utilized to determine the particle size distribution of the hydrometeors (Zhang et al. 2001). The gamma distribution

$$N(D) = N_0 D^{\mu} \exp(-\Lambda D), \tag{2.10}$$

has been widely accepted to model rain DSDs (Ulbrich, 1983). $N_0$ ($mm^{-1-\mu}$ $m^{-3}$) is the number concentration parameter, $\mu$ is the distribution shape parameter and $\Lambda$ ($mm^{-1}$) is the slope parameter. The following constraining relation (Cao et al. 2008), empirically derived from 2DVD measurements of rain in Oklahoma, is used for rain microphysical retrievals in this study:

$$\mu = -0.0201\Lambda^2 + 0.902\Lambda - 1.718. \tag{2.11}$$

The $\mu$- $\Lambda$ relation used for the ice phase precipitation (ice pellets)

$$\mu_{ip} = -0.0048\Lambda^2 + 0.8856\Lambda - 1.9124, \tag{2.12}$$

is derived from periods identified as IP and measured with 2DVD. This $\mu$-$\Lambda$ relation (Fig. 2.1) is obtained from the second, fourth, and sixth moments of the measured PSDs.

Parameters $N_0$ and $\Lambda$ of the constrained (via eq.'s 11 and 12) gamma distribution are directly estimated from radar measurements of $Z_H$ and $Z_{DR}$ respectively as explained in Zhang (2016). From this distribution, various precipitation parameters such as median volume diameter $D_{0r}$, rainfall rate $R_r$ and ice pellets liquid water equivalent rate $R_{ipr}$ are retrieved:

$$\int_{D_{min}}^{D_{0r}} D^3 N(D)\, dD = \int_{D_{0r}}^{D_{max}} D^3 N(D)\, dD, \tag{2.13}$$

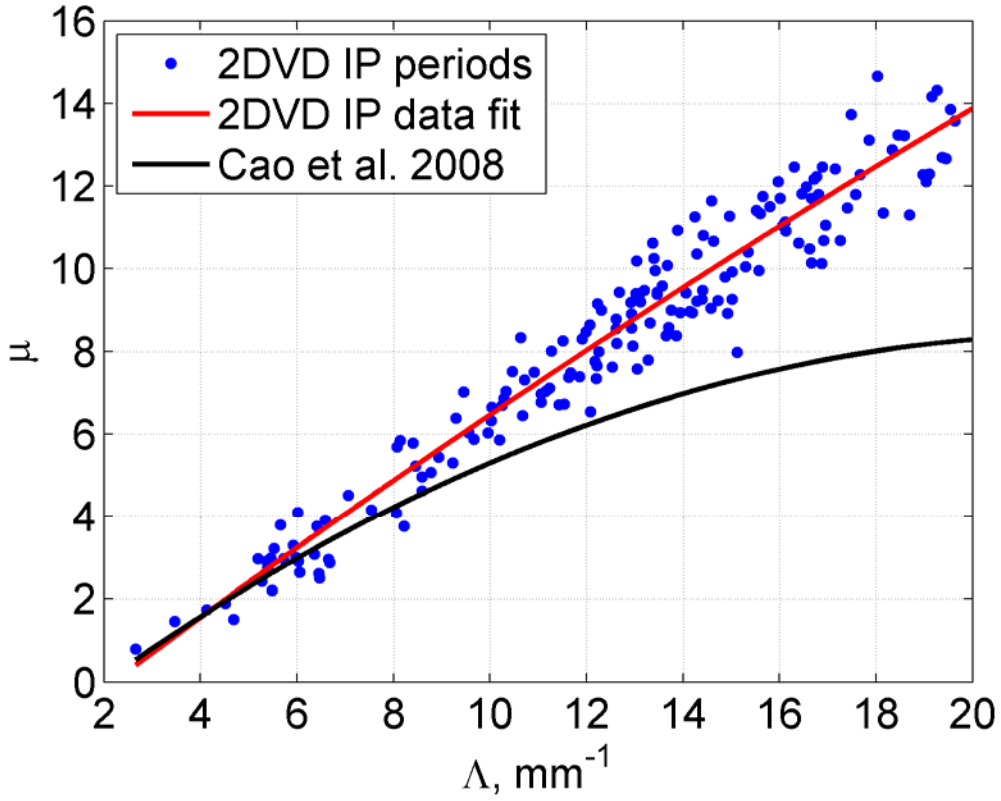



Figure 2.1: $\mu$-$\Lambda$ scatterplot - blue dots are estimated values of $\mu$ and $\Lambda$ from 2DVD measurements using the 2nd, 4th, and 6th moments of the measured distributions during the IP periods (0645 to 1100 UTC, and 1730 to 2130 UTC), whereas red line denotes 2nd degree polynomial data fit during these periods. The black line represents the rain $\mu$-$\Lambda$ relation from Cao et al. (2008).

$$R_{\mathrm{r}} = 6\times10^{-4}\pi\sum_{\mathrm{i}=1}^{L} D_{\mathrm{i}}^{3} v\left(D_{\mathrm{i}}\right) N\left(D_{\mathrm{i}}\right)\Delta D, \tag{2.14}$$

$$R_{\mathrm{ipr}} = 6\times10^{-4}\pi\frac{\rho_{\mathrm{ice}}}{\rho_{\mathrm{w}}}\sum_{\mathrm{i}=1}^{L} D_{\mathrm{i}}^{3} v\left(D_{\mathrm{i}}\right) N\left(D_{\mathrm{i}}\right)\Delta D. \tag{2.15}$$

$D_{\mathrm{min}}$ and $D_{\mathrm{max}}$ are particles' minimum (set to 0.1 mm) and maximum diameters, where $D_{\mathrm{max}}$ can be estimated from the radar reflectivity (or differential reflectivity, see Brandes et al. 2003); $v(D_{\mathrm{i}})$ denote raindrops' terminal velocity in m $s^{-1}$ (Brandes et al. 2002) and the same is used for the IP terminal velocity as suggested by 2DVD

measurements (see section 4*b* for clarification). $\Delta D$ is bin spacing, set to 0.2 mm in our computations.

To interpret radar measurements over the disdrometer site, we use representations in the vertical planes. Herein two such representations are explained. The first we call Slanted Vertical Profile (SVP). It was inspired by the Quasi Vertical Profile (QVP) introduced by Ryzhkov et al. (2016) to analyze vertical structure at a higher resolution. Our SVP profile is presented in the vertical cross-section positioned along the radial that is located over the disdrometer. Figure 2.2 illustrates how one vertical profile along height is obtained. The radial over the disdrometer (2DVD) has azimuth $az_d$ and elevation $e_l$, which in our case is $\leq 1^o$. A beginning range $r_b$ and ending range $r_e$ are chosen so that the disdrometer is about at the midpoint. Similarly, a beginning azimuth $az_b$ and ending azimuth $az_e$ are chosen to encompass the disdrometer's azimuth. Data from radials at adjacent azimuths between $az_b$ and $az_e$, same $e_l$, and constant range are averaged to produce a single value. The array of such points along range is the radial profile of the variable. Then the data from the $r_b$ to $r_e$ are projected on the vertical axis to produce an SVP corresponding to the time of the scan. Typically the range interval is up to 60 km and the azimuthal span is $20^o$. *The data over such large range intervals are likely inhomogeneous, hence interpretation needs to be very cautious.* Clearly, relating the top of the profile to the bottom could produce absurd results. But in our interpretation, we do not attempt to relate data from vastly different ranges. Rather we concentrate on the height $h_d$ which is directly over the disdrometer site. Then we examine a small increment above and below this height to interpret the change in the polarimetric variables. The small increment corresponds to the range

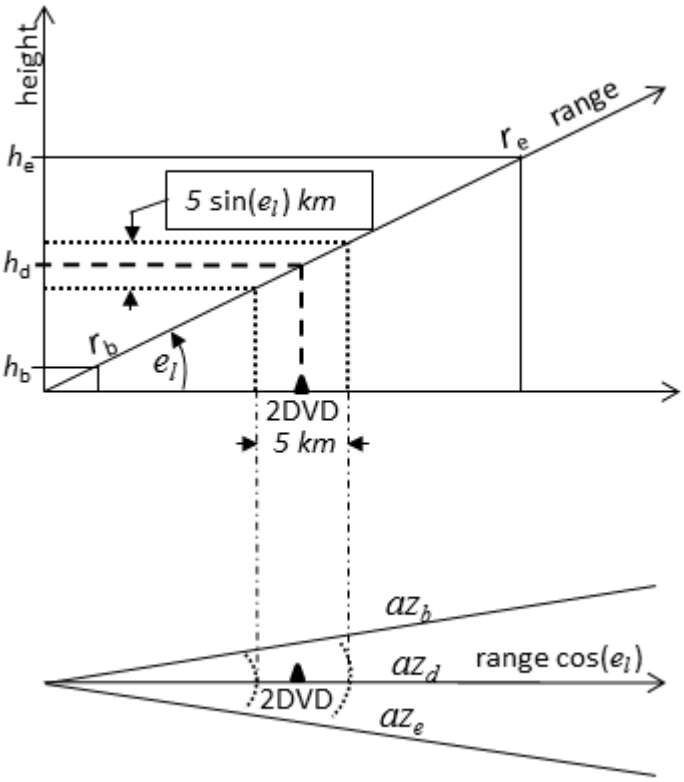



Figure 2.2: Diagram explaining computation of the Slant Vertical Profile and its interpretation. For simplicity, a flat earth is assumed in the sketch whereas in actual computations earth's curvature is accounted for via the 4/3 equivalent radius model. The vertical plane bisects the radar and disdrometer locations. The projection of the conical section over which the data are averaged is at the bottom of the figure. The disdrometer is located at 29 km from the radar, the extent of averaging in azimuth $az_e$-$az_b$ = 20°. In the data interpretation, the band of values 5sin($e_l$) km wide and centered at the height above the disdrometer is examined.

interval of 2.5 km for a total of 5 km centered on the disdrometer, making the vertical extent equal to 5 sin($e_l$) km (Fig. 2.2). Over such short range, the homogeneity is much more likely to hold, although it is not guaranteed. An additional concern is smoothing by the beam which at the disdrometer site extends over about 500 m. The beam positions in the SVP are such that the edge (3 dB point) of the beam does not reach the

bright band. Hence the data are not contaminated by the strong gradient of $Z_H$ at the transition from the bright band to the precipitation below. At the disdrometer location, the azimuthal averaging sector equals 10 km. Note that in our analysis the earth's curvature and 4/3 radius model are taken into account but are not presented in the simplified diagram (Fig. 2.2).

The second presentation in the vertical plane we call Enhanced Vertical Profile (EVP). This profile is constructed from all available elevation scans over the disdrometer. At each elevation, a median is applied to three radials and five range locations starting 2.5 km before the disdrometer. The procedure is repeated in the range up to 2.5 km beyond the disdrometer location. These median values are projected from all elevations to the vertical to create one vertical cut (EVP) over the disdrometer (see Fig. 2.7).

An additional presentation convenient for a time series of variables uses only the median of the three (in azimuth) by five (in range) points above the disdrometer at a fixed elevation. Herein this is applied to data at the two lowest elevations (see Figs. 2.11 and 2.12).

The identification of the precipitation phase change in the 2DVD data was accomplished by a visual examination of the images which exhibit a clear distinction between irregular shapes of ice hydrometeor and oblate raindrops (some images are in Fig. 2.4).

## 4. Results

The principal findings of the study are in this section, which consists of five subsections corresponding to the five topics as follows: environmental data, 2DVD data, radar data, refreezing model, and radar-2DVD comparisons.

*a. Environmental data*

In the preliminary data perusal, the vertical profiles from the radiosondes (available at http://weather.uwyo.edu/upperair/sounding.html) and Rapid Update Cycle (RUC, available at https://nomads.ncdc.noaa.gov/data/rucanl/200701/20070120/) analysis were examined, as presented in Fig. 2.3a-2.3c for 0000, 1200, and 1800 UTC respectively for the Norman radar (KOUN) location. Generally, these are well-matched (especially temperature), with minor discrepancies in dew point temperature mostly in drier air where the RUC slightly overestimates dew point temperature (Fig. 2.3a). Some subtle differences (up to few $^{o}$C) also exist between radiosonde and RUC temperature profiles when multiple melting and freezing layers are present (Fig. 2.3a). Because the temporal resolution of the radiosondes' measurements is very sparse and available only at 6-hour intervals, RUC analysis soundings are examined for better insight into environmental conditions. The time evolution of RUC analysis temperature and relative humidity vertical profiles over the 2DVD location (KAEFS) are plotted in Fig. 2.3d-2.3e. RUC temperature profiles are compared with radio acoustic sounding system (RASS) profiles (Fig. 2.3f) obtained from the collocated NOAA's Purcell wind profiler. The RASS measurements could only be obtained in conditions of little to no precipitation; thus no reliable data is recorded after ~1130 UTC. Nonetheless, RUC analysis temperature profiles match well with RASS measurements between 0100 and

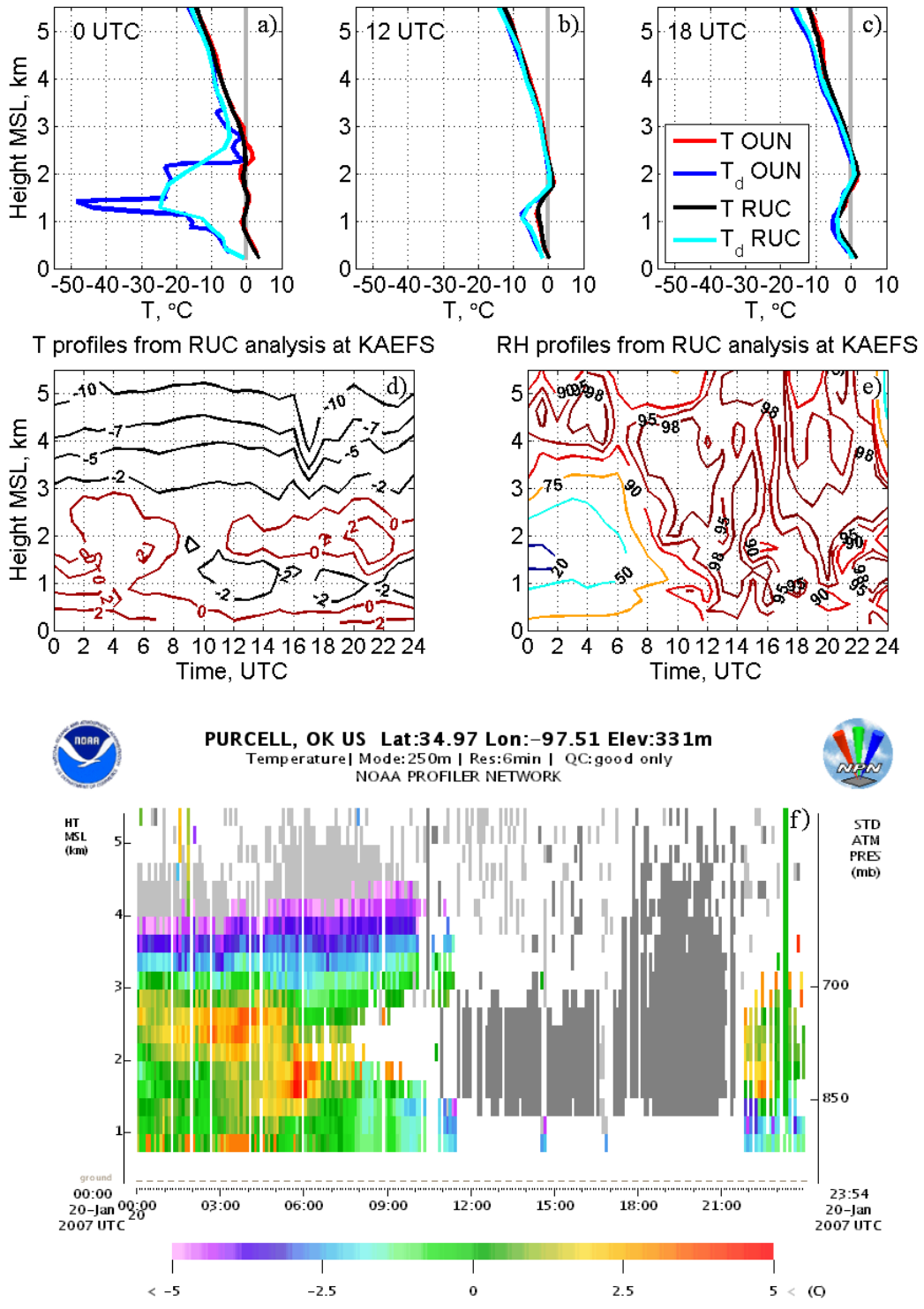



Figure 2.3: Comparison of radiosondes and RUC analysis soundings for Norman (OUN) at 0000 (a), 1200 (b), and 1800 (c) UTC. Evolution of temperature (d) and relative humidity (e) profiles over KAEFS. Temperature profiles from RASS soundings Purcell profiler (f) at KAEFS.

0400 UTC, where the temperatures above 0°C extend from ~2500 m MSL to the ground, with elevated freezing layer centered at ~1500 m between ~0200 and 0300 UTC. As seen in earlier comparisons between RUC and radiosonde profiles (e.g., 0000 UTC for Norman OUN location, Fig. 2.3a), RUC does not reproduce the elevated melting layer ~2200 to 3000 m MSL at 0000 UTC, which clearly exist in the RASS profile. Also, there is no indication of a melting layer above the ground in the RUC profile between 0800 and 1130 UTC, but a melting layer is seen in the RASS data at ~2000 m MSL until ~1000 UTC when the RASS measurement started to become unreliable. There is presence of a freezing layer in the RASS data from ~0700 until 1130 UTC, extending from ~700 to 1700 m MSL, which is also present in the RUC profile with minimum temperatures from both sources close to -3°C. The air is relatively dry (0000 until 0930 UTC) in the layer extending from ~3000 m to the ground, as seen in the RUC relative humidity profile (Fig. 2.3e). There is also a nearly saturated layer (>95% RH) aloft at ~3000 to 5000 m MSL for the same period. Air becomes nearly saturated from 1200 UTC until the end of the event at low and medium tropospheric levels (0 to 5000 m MSL).

In summary, it is indicated from all available data sources (including KOUN radar) that the temperature profile exhibited very complex, multiple melting-refreezing layered structures. At the beginning of the event, the double melting and refreezing layers are suggested by the inferred temperature profile. The primary melting layer (~700 to 2000 m AGL) is accompanied by the shallow refreezing layer and a secondary shallow melting layer towards the ground. Surface temperature suggests a secondary shallow refreezing layer next to the ground. This complex structure gradually evolved

to a stronger melting layer aloft, with increased height and depth (from 1230 to 2100 UTC), and refreezing occurred at lower altitudes than in the previous stages.

*b. Data from the 2DVD*

The images and velocities of particles measured by the 2DVD are analyzed next. A high percentage of recorded ice pellets (>99%) exhibited fast-falling velocities, very close to those of raindrops, hence it was difficult to distinguish between the precipitation types using measured velocity distribution. In contrast, only a few IP displayed slow-falling velocities ranging from 1-3 m $s^{-1}$. In a study by Nagumo and Fujiyoshi (2015), the number of fast-falling ice pellets was higher than the number of slow-falling ice pellets but comparable (for IP greater than 1.5 mm in diameter, the ratio was roughly 3 to 1 in favor of fast-falling). In this study, slow-falling IP were identified with 2DVD by looking into both falling velocities and images from orthogonal cameras, whereas fast-falling IP were identified visually. Images of both fast and slow IP recorded with the 2DVD are in Fig. 2.4. In general, larger IP ($D$ > 1.5 mm) are easily identified due to rugged shapes that deviate from the oblate shapes of the same-sized raindrops (Fig. 2.4). Smaller IP ($D$ < 1 mm), especially near-spherical, are much harder to discriminate from the similar-sized raindrops due to the 2DVD's resolution (~0.2 mm in horizontal) and due to particle's contour depiction by the 2DVD visualization software (as seen in Fig. 2.4). Therefore we assume that if larger particles are identified as rain, smaller ones in the same period are assigned to the rain category although some could be partially frozen. If the larger particles are ice pellets, then the smaller ones must be pellets too as these would have frozen before the larger ones.

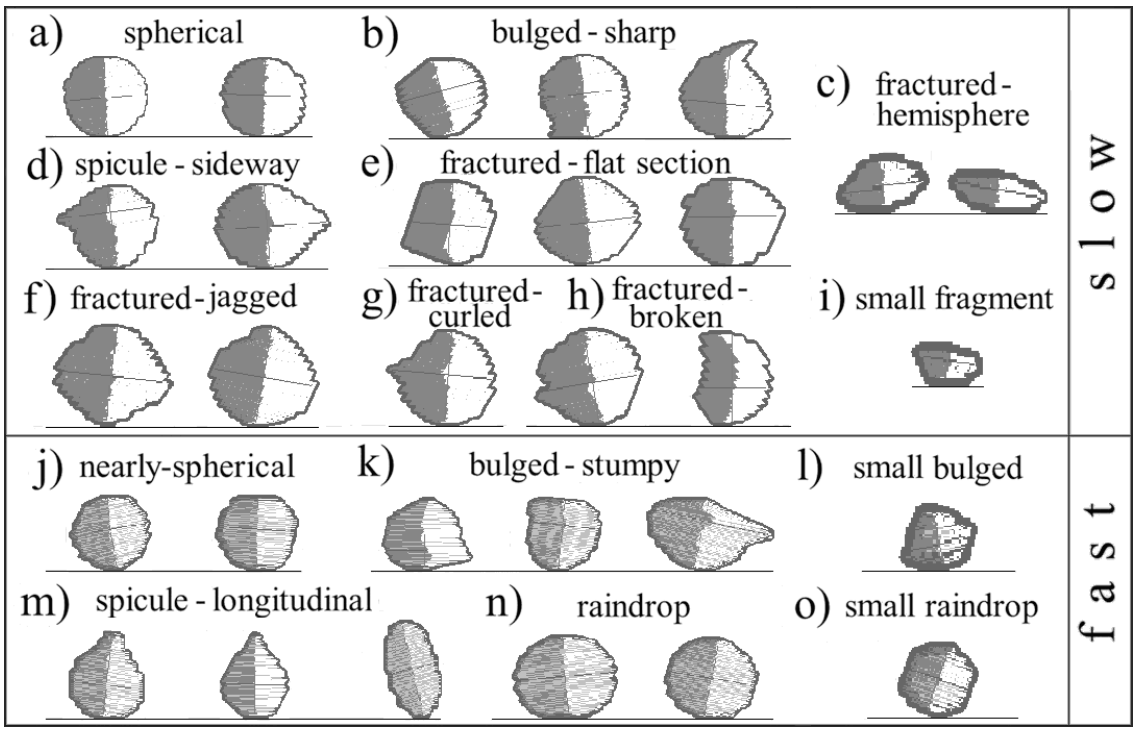



Figure 2.4: Images of IP and raindrops from 2DVD (not in scale). Typical silhouettes of: (a)-(i) slow-falling IP; (j)-(m) fast-falling IP; and (n)-(o) raindrops. The particles in (c), (i), (l), and (o) are less or equal to 1 mm whereas the other particles dimension is between 1.5 and about 3 mm. The fast particles fall speeds are about the same as those of raindrops. The slow particles fall speeds were between 55 % and 80 % smaller than those of equivalent size raindrops.

The disdrometer measurements suggest that the primary ice phase period occurred between 0645 and 1100 UTC, and a secondary period was from ~1730 to 2130 UTC. Between 1100 and ~1730 UTC, freezing rain and rain are the dominant types of precipitation, with just a few shorter ice phase transitions until 2130 UTC, when precipitation started changing into snow (not shown). Temperature measurements from the nearby Washington Mesonet station (not shown) indicate that freezing at 1.5 m above ground level occurred from ~0720 to 1430 UTC, partially coinciding with the primary ice pellet periods. The lowest temperature was about -0.5°C from 1030 until 1200 UTC. The temperature at 9 m above ground level implies that freezing occurred

from 0615 until 2130 UTC, with the lowest temperature of about -0.8°C from 1100 until 1215 UTC.

The time evolution of the DSD, mass, $Z_H$ and $Z_{DR}$ distributions measured and/or calculated from the 2DVD are shown in Fig. 2.5a-2.5d, where $Z_H$ and $Z_{DR}$ are obtained from the measured DSDs assuming liquid phase. The mass was computed for each size bin assuming liquid density and the volume of the particle at the observed equivalent diameter $D_i$. The simulated radar variables were similarly computed at each size

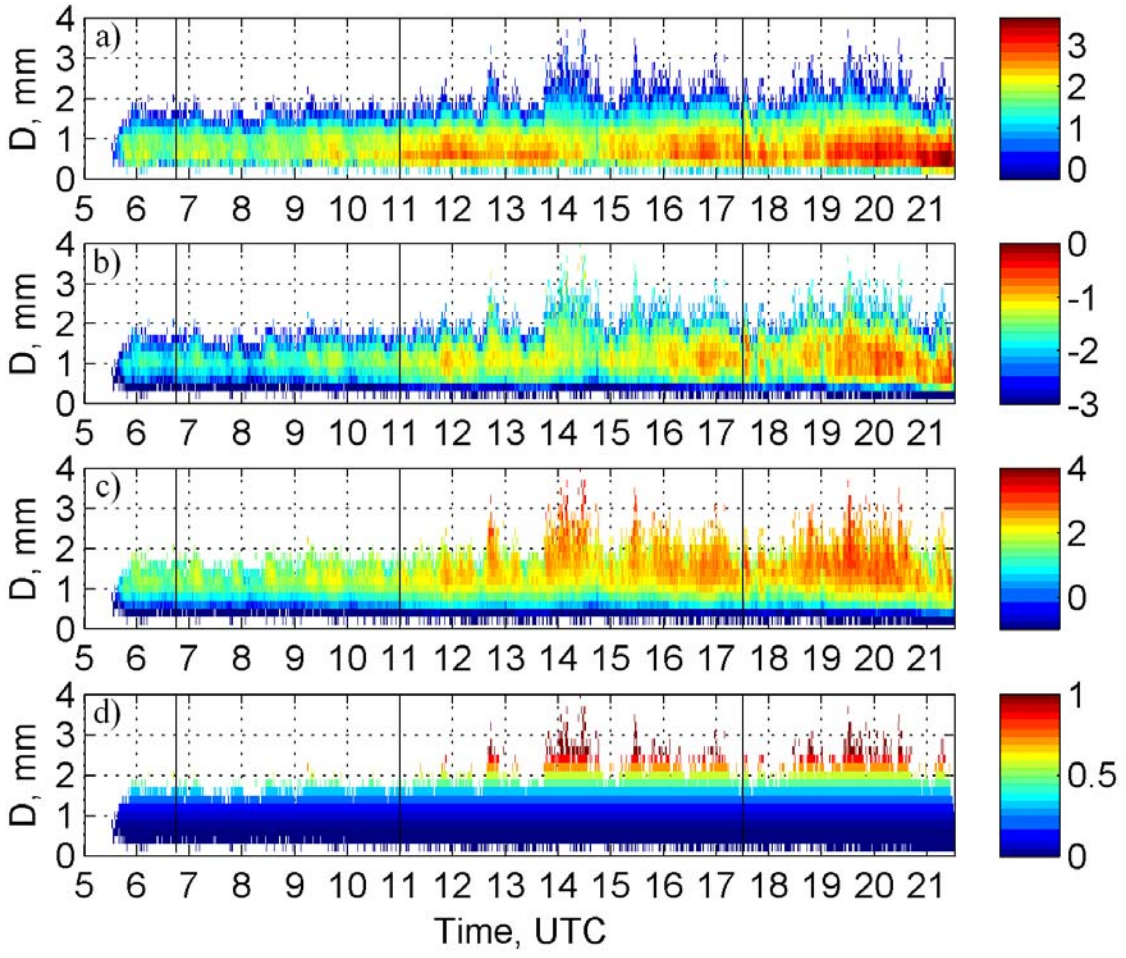



Figure 2.5: Evolution of: (a) DSD [$\log_{10}(m^{-3}\ mm^{-1})$], (b) mass [$\log_{10}(g\ m^{3}\ mm^{-1})$], (c) $Z_H$ [$\log_{10}(mm^{6}\ m^{-3}\ mm^{-1})$], and (d) $Z_{DR}$ [dB] distribution measured with 2DVD; thin black lines denote main ice pellets periods from ~0645 until 1100 UTC and 1730 to 2130 UTC.

category using the T-matrix and relations between the size and the variable in the case of the liquid phase. The results are plotted as a distribution with respect to $D_i$.

In the primary ice pellets period (~0645 until 1100 UTC, denoted by thin vertical black lines), DSD values are smaller than in the rain periods and range up to ~240 $m^{-3}$ $mm^{-1}$ (at ~0.6 mm size). The DSDs are initially narrow (before 1030 UTC) and gradually broaden with time in the mature stage, which predominantly consists of rain periods. In the secondary IP period (1730 to 2130 UTC, denoted by a thin vertical line), there are several periods of IP alternating with rain/freezing rain. In comparison to earlier storm stages, DSD values are larger, and the highest concentrations coincide with the occurrence of rain. In general, larger concentrations of particles are seen from 1100 to 2130 UTC for diameters $D$ = 0.4 mm to 1.6 mm, with the highest value at about 2120 UTC with $N(D)$~4500 $m^{-3}mm^{-1}$ for $D$~0.7 mm. Particles with sizes between 0.9 mm and 1.3 mm contribute to the maxima in the mass distribution while larger drops contribute the most to the maxima in reflectivity and differential reflectivity distributions.

*c. Radar data*

The morphology of the storm is observed in the fields of $Z_H$, $Z_{DR}$, and $\rho_{hv}$ (Fig. 2.6a-2.6c, 0730 UTC) displayed on conical surfaces (PPI). The $Z_H$ varied between 0 and 20 dBZ in the beginning of the event, whereas in later stages of the storm it increased up to ~40 dBZ. $Z_{DR}$ values were noisy most of the time but generally did not exceed 2 dB, not even in the middle stages when rain was a dominant type of precipitation. At ~0730 UTC (Fig. 2.6a-2.6c), there is a localized drop in $Z_H$ and $\rho_{hv}$, coinciding with the measurable enhancement of $Z_{DR}$ in the vicinity and southwest of the 2DVD location,

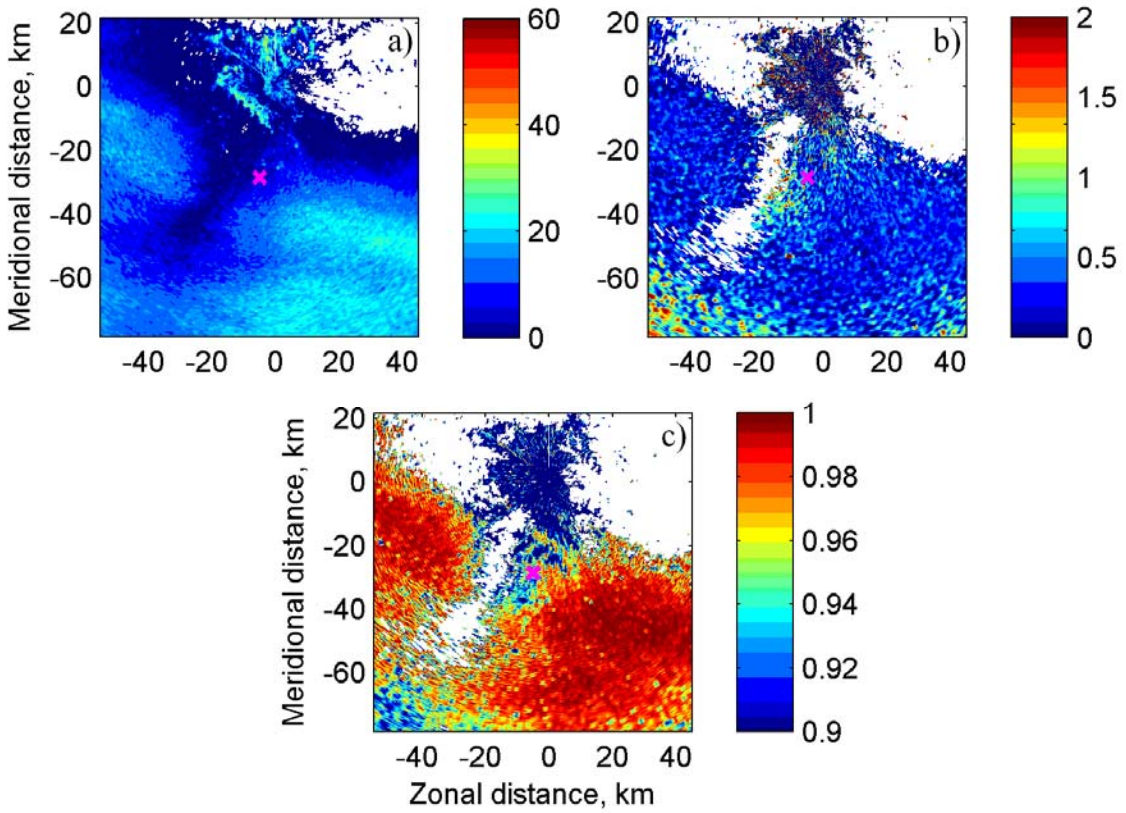



Figure 2.6: PPI of $Z_H$ (a), $Z_{DR}$ (b) and $\rho_{hv}$ (c) at 0730 UTC and elevation of 0.41°. The magenta colored x represent 2DVD location (KAEFS). The high values of $Z_H$ extending diagonally from NW to SE at about 10 km off the radar is an orographic ridge which in this case shields the disdrometer location from the influence of ground clutter.

marked by magenta x's in Fig. 2.6a-2.6c. The 2DVD indicates ice pellets at this time. Thus the described change of the polarimetric variables we attribute to refreezing associated with the ice pellets. The "refreezing patch" disappeared later during the rain period, suggesting that the phenomenon is real. Ryzhkov et al. (2011a) and Kumjian et al. (2013) reported a repetitive ring-like structure of enhanced $Z_{DR}$ and reduced $\rho_{hv}$ values (reduction in $Z_H$ occurs as well but gradually along the radial instead of in a localized ring) in PPIs at intermediate or higher elevations (>3°) if refreezing is ongoing. Their cases were more spatially uniform and refreezing was widespread across radar coverage area, thus much easier to interpret. This contrasts the patchy and very

localized occurrence about 30-40 km south-southwest from the radar in our case. Also, the height of the refreezing layer in our case is lower: it ranges from ~70 m to ~700 m AGL, compared to ~400 m to ~800 m in Ryzhkov et al. (2011a), or ~300 m to ~1000 m in Kumjian et al. (2013). Another very important difference is that the minimum temperature of the refreezing layer, or "refreezing zone" as dubbed in Ryzhkov et al. (2011a), in our case rarely dropped below -4°C (from Norman radiosonde soundings at 1200 and 1800 UTC, RASS and RUC temperature profiles), whereas it ranged from -5 °C to -12°C in these previous studies.

The time evolution of the enhanced vertical profiles (EVP's are explained in section 3) of the radar variables $Z_H$, $Z_{DR,}$ and $\rho_{hv}$, created from volume PPI scans over the disdrometer site are presented in Fig. 2.7a-2.7c; overlaid are RUC temperature vertical profiles (black dashed lines represent below freezing, while magenta dashed lines above freezing temperatures). In all three polarimetric variables, the melting layer is well defined with the increased $Z_H$ and $Z_{DR}$ but reduced $\rho_{hv}$ values. The height of the melting layer from RUC analysis soundings agrees well with that seen in the polarimetric measurements (~2 km AGL), except from ~0800 until 1130 UTC when RUC soundings show only freezing temperatures (although relatively close to 0°C), as described earlier (Fig. 2.3d). The evolution of $Z_H$, $Z_{DR}$, and $\rho_{hv}$ (Fig. 2.7a-2.7c) reveals the presence of a weaker melting layer centered at ~1900 m AGL (approx. 2250 m MSL) from ~0800 until 1130 UTC. Over the primary period of ice pellets (0645 to ~ 1100 UTC) $Z_H$ values are very low (0 to 10 dBZ) within the sublayer from ~700 m extending close to the ground. The trend of lower values of $Z_{DR}$ (from 0 to 0.5 dB) and $\rho_{hv}$ (0.9 to 0.95) within the sublayer is also seen. Low $Z_H$ and $Z_{DR}$ could be due to either

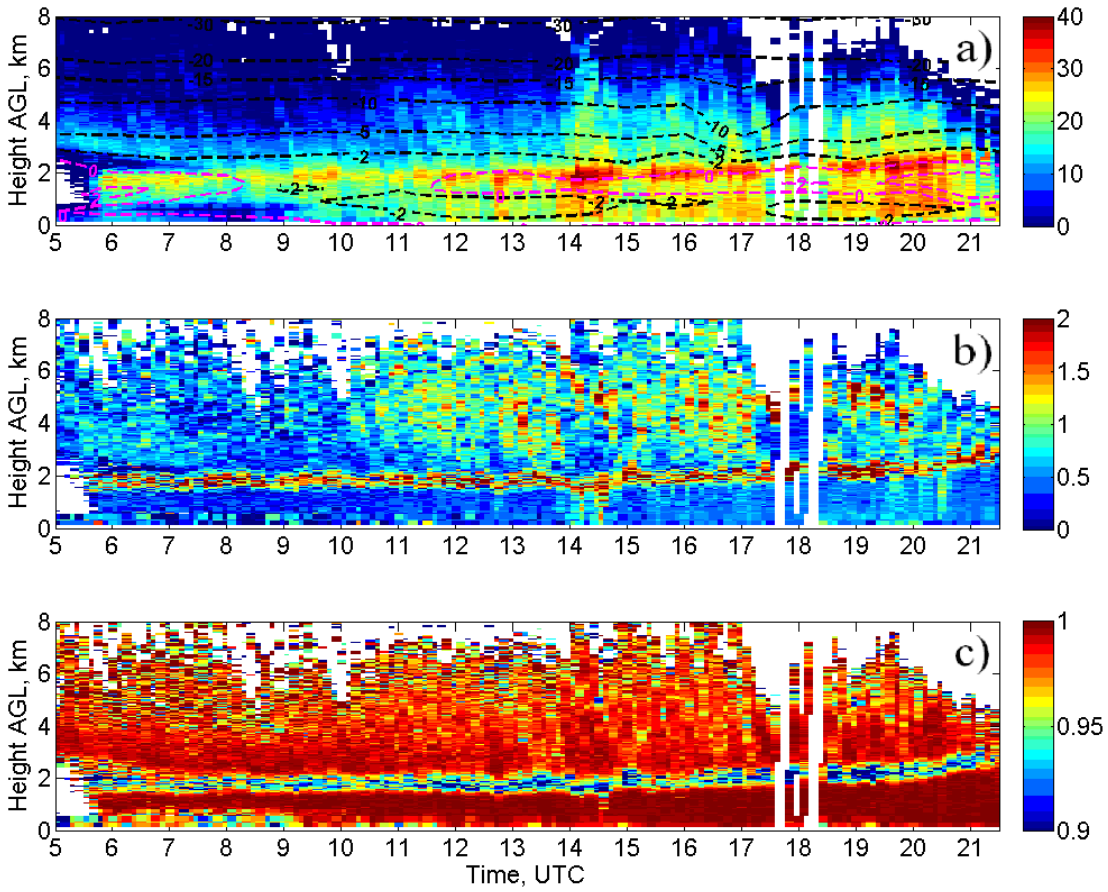



Figure 2.7: Evolution of enhanced vertical profiles of $Z_H$ (a), $Z_{DR}$ (b) and $\rho_{hv}$ (c) measured with KOUN over 2DVD site. Height is referenced above ground level (AGL). Dashed lines denote RUC analysis temperature profiles above 2DVD location, where black color represent temperature below freezing while magenta above freezing.

small raindrops ($D$ < 1.5 mm) or ice pellets. Although the reductions in $Z_H$ and $\rho_{hv}$ within the sublayer are obvious throughout the period of interest, the localized coinciding increase in $Z_{DR}$ is not. There are some hints of about 0.2 to 0.3 dB increase in $Z_{DR}$ next to the ground. On the onset of precipitation, at about ~0545 UTC, there is a short period of warming as both RASS and RUC indicate (at ~1500 m MSL), coinciding with the temporary strengthening of the bright band, followed by the slightly enhanced values of the $Z_H$ extending all the way to the ground. During the primary ice

pellet period, the bright band is weaker compared to later periods of rain, melting layer is shallower, with refreezing layer temperature estimated from RASS and RUC profile to be no lower than -3.5°C. In general, moisture availability gradually improves from the onset of precipitation at ~0545 UTC throughout the event (in the lowest 3000 m), modifying the air from unsaturated to slightly subsaturated with respect to water and (most likely) saturated with respect to ice (Fig. 2.3e). All these environmental conditions made the period 0645 to 1100 UTC favorable for ice pellet formation. During the secondary IP period, there are also hints of refreezing signatures in EVPs between 1815 and 2015 UTC (lowest 300 m), but slightly weaker than during the previous IP period because refreezing occurred at even lower altitudes. This is partially caused by the increased height and depth of the melting layer, allowing particles to almost entirely melt, thus needing more time to refreeze. From 1730 until ~2200 UTC the lower (1-1.5 km) tropospheric levels become less saturated, again leading to more favorable conditions for evaporative cooling to occur, resulting in frequent IP appearances during the period.

Our 2DVD location is approximately 29 km south from the radar, and coincidently favorable conditions for the ice phase precipitation are found close to the disdrometer site. Moreover, refreezing was localized at lower altitudes (~70 m to ~700 m AGL). This motivated construction of SVPs (defined in section 3) at the lowest elevations. The SVP at $1^{o}$ elevation (Fig. 2.8 within the box) between 0645 and 0915 UTC clearly displays the onset of the refreezing signature. The box isolates parts of the refreezing layer ~550 m to 660 m AGL. The $Z_H$ and $\rho_{hv}$ decrease ($Z_H$ about 5-7 dB and

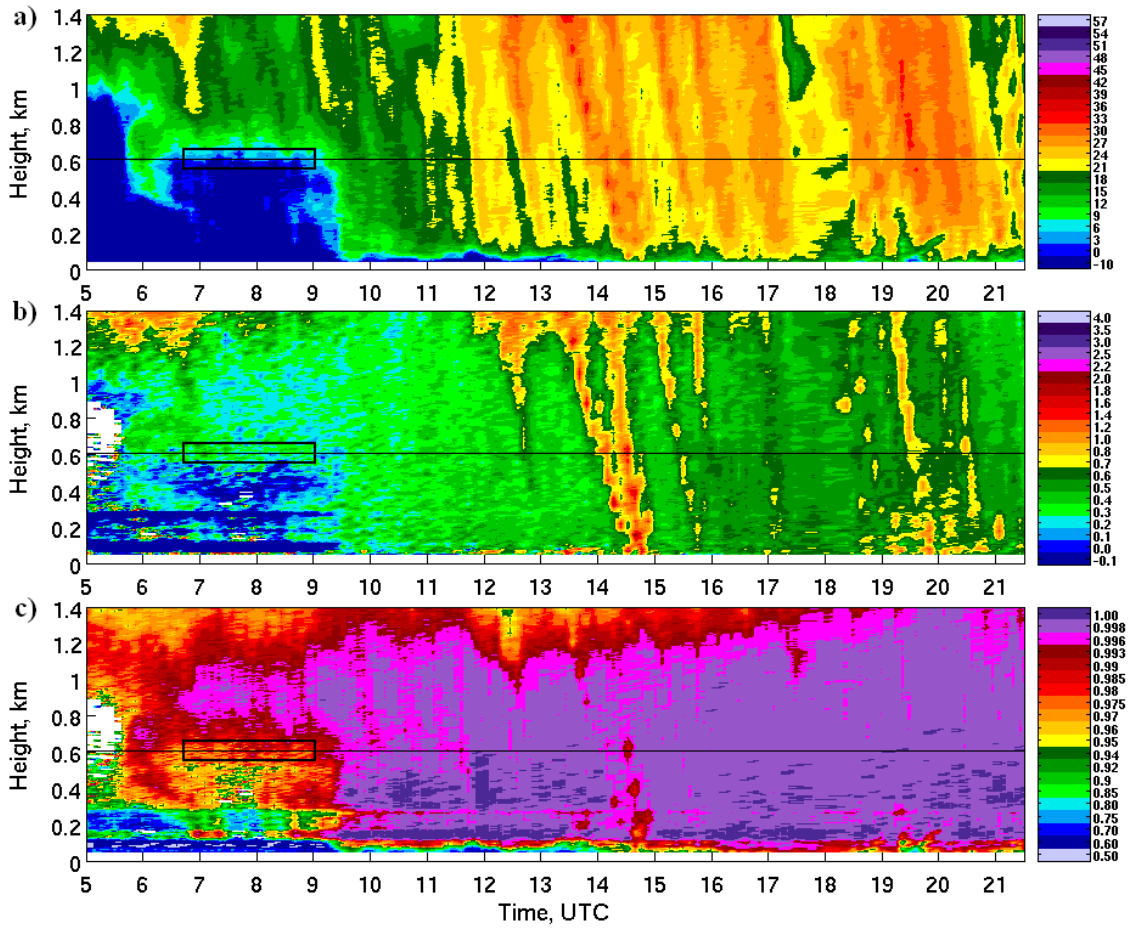



Figure 2.8: Evolution of SVPs at 1° elevation of $Z_H$ (a), $Z_{DR}$ (b) and $\rho_{hv}$ (c) from KOUN. The thin black line at ~610 m AGL represent height directly above 2DVD location; the thick black box represents 5 km radial segment along the 1° elevation (height projections) centered on 2DVD location and indicates a period of refreezing.

$\rho_{hv}$ ~0.02) towards the ground while the $Z_{DR}$ has a week local maximum (~0.4-0.6 dB). Similarly, the SVP reconstructed from the 0° elevation (Fig. 2.9) indicates refreezing layer (times 0645 to 1100 UTC and height 90 to 110 m AGL). Further examination of the data including temperature (Fig. 2.7) suggests that partial melting could have occurred above 110 m. We speculate that the $Z_H$ in Fig. 2.9 is higher than in Fig. 2.8 because of this partial melting. Two warm layers with a cold layer in between them are clearly seen in Fig. 2.7. Because the temperatures at 9 m AGL were negative from 0615

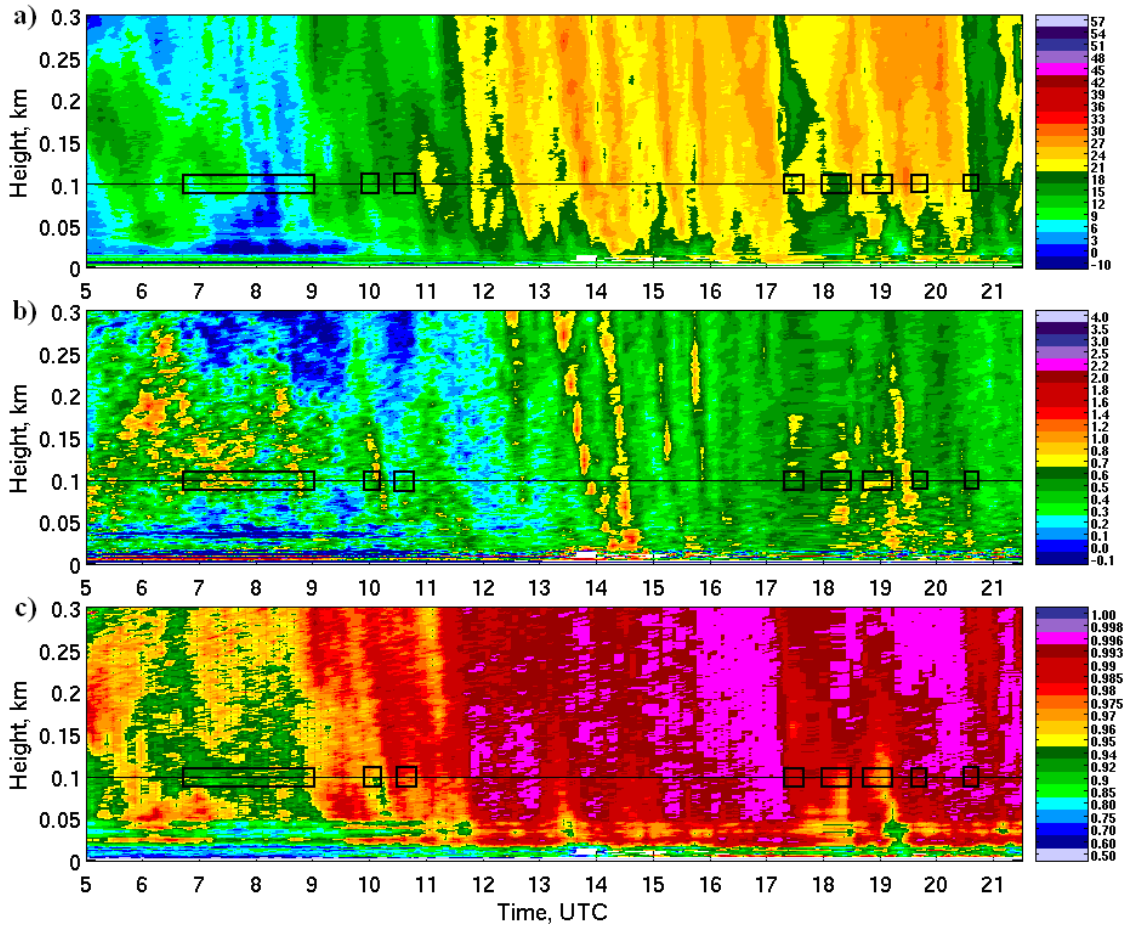



Figure 2.9: Evolution of SVPs at 0° elevation of $Z_H$ (a), $Z_{DR}$ (b) and $\rho_{hv}$ (c) from KOUN. The thin black line at ~100 m AGL represent height directly above 2DVD location; the thick black boxes represent 5 km radial segment along the 0° elevation (height projections) centered on the 2DVD location and indicate periods of refreezing.

until 2100 UTC, and also at 1.5 m AGL from 0720 to 1430 UTC, there was an additional cold layer below the second warm layer implying two regions of refreezing. The decrease in $Z_H$ (~4-7 dB), the persistence of $Z_{DR}$ (~0.5-0.9 dB), and local minimum of $\rho_{hv}$ (~0.92-0.95) are consistent of refreezing. The fact that this SVP projects the radial at $0^o$ elevation (uses 4/3 earth curvature model) make the interpretation challenging.

The secondary IP period from 1730 to 2130 UTC interrupted with a few short rain episodes is identified in the disdrometer data. The refreezing periods, lasting ~ 20

minutes, and centered at about 1730, 1815, 1855, 1940, 2015, 2035 and 2110 UTC, are marked by thick black boxes (Fig. 2.9a-2.9c) encompassing slight enhancement in $Z_{DR}$ (~0.1-0.3 dB), and reduction in $Z_H$ (3-6 dB) and $\rho_{hv}$ (by about 0.03). Radar PPI plots (not shown) indicate the freezing patch was centered west of the 2DVD and its eastern edge was barely over it. Thus, azimuthal averaging reduced its signature in the SVP presentation. The SVP from the 0.41° (not shown), at just a bit higher altitude above the 2DVD site, exhibits one similar feature at 1815 UTC as the one from 0° elevation but not the others. This is because the "refreezing patch" drifted west, the melting layer intensified, and the refreezing layer lowered.

In all data, the SNR within the refreezing area is larger than 15 dB and most values are between 20 and 30 dB. The effects of noise on the polarimetric variables were corrected to eliminate bias. Thus, the variability is caused by meteorological conditions and the statistical uncertainty which increases at lower $\rho_{hv}$. Refreezing is close to the ground and within a layer smaller than beam resolution, obscuring detection. A further complication is the double melting and refreezing suggested by the inferred temperature profile at the beginning of the event. Nonetheless, examination of polarimetric signatures clearly demonstrates that precipitation other than pure rain is occurring. Without the disdrometer, it would be hard to discriminate with polarimetric variables between ice pellets and slush.

*d. Refreezing model*

Kumjian et al. (2013) proposed two plausible mechanisms for polarimetric refreezing signature: preferential freezing of small drops and local ice generation. In our case, local ice generation seems highly unlikely due to relatively high freezing

temperatures (>-4°C) and weak $Z_{DR}$ increase (pointing towards more spherical particles) in the "refreezing". Preferential freezing of small drops gradually decreases the effects of the complex dielectric constant because of sequential freezing of first small drops followed by larger drops until all are frozen. The expected total decrease in $Z_H$ is about 6-7 dBZ. Similar to Kumjian et al. (2013), we use the Marshall-Plamer DSD model to calculate $Z_H$ and $Z_{DR}$ for different rainfall rates (0.1, 0.3, 0.5, and 1 mm $h^{-1}$) and two size spectra, $0.05 < D < 2$ mm, and $0.05 < D < 4$ mm; these maximum diameter values were observed with the 2DVD. We use 0.05 mm size increments to explore the validity of this hypothesis. Disdrometer measurements indicate that rainfall rates (or more appropriate $R_{ip}$ rates) for the primary IP period are rather small (see Fig. 2.11b), less than 0.5 mm $h^{-1}$, hence much smaller than in Kumjian et al. (2013) simulations. In addition, 2DVD measured drop size spectra are narrow during the primary IP period, with $D < 2$ mm. Later IP periods have slightly larger particle sizes, up to ~ 4 mm. The impact of preferential freezing of small drops for narrower spectra (herein NS, 40 DSD bins, $0.05 < D < 2$ mm) on $Z_H$ and $Z_{DR}$ are presented in Fig. 2.10a, b, while computations for broader spectra (herein WS, 80 bins, $0.05 < D < 4$ mm) are in Fig. 2.10c, d. Preferential freezing is simulated by sequentially "freezing" each DSD diameter (bin), starting from the smallest size, where $Z_H$ and $Z_{DR}$ are calculated as a function of frozen diameters (herein $D_f$). Both NS and WS computations show a decrease of $Z_H$ by ~7 dBZ with sequential freezing; the faster decrease of $Z_H$ occurs for smaller sizes and NS simulation in general. The maximal $Z_{DR}$ happens later for larger particles because of the greater relative contribution of larger liquid drops to intrinsic $Z_{DR}$. Regarding the size spectra, the magnitude of the $Z_{DR}$ increase is much smaller for

the NS compared to the WS simulation. For $R$ = 0.5 mm h$^{-1}$, NS $Z_{DR}$ is 0.36 dB and $D_f$ = 1.45 mm compared to 0.56 dB and $D_f$ = 1.75 mm from WS. This example indicates how the width of DSD may affect the magnitude of $Z_{DR}$ increase as well as $Z_H$ reduction in the refreezing region. SVPs for the primary IP period indicate that the range of maximum $Z_{DR}$ is between 0.3 and ~0.9 dB, which is comparable to the simulated values (Fig. 2.10). Note that the magnitude of $Z_{DR}$ actually decreases (by ~0.1 to ~0.4 dB in

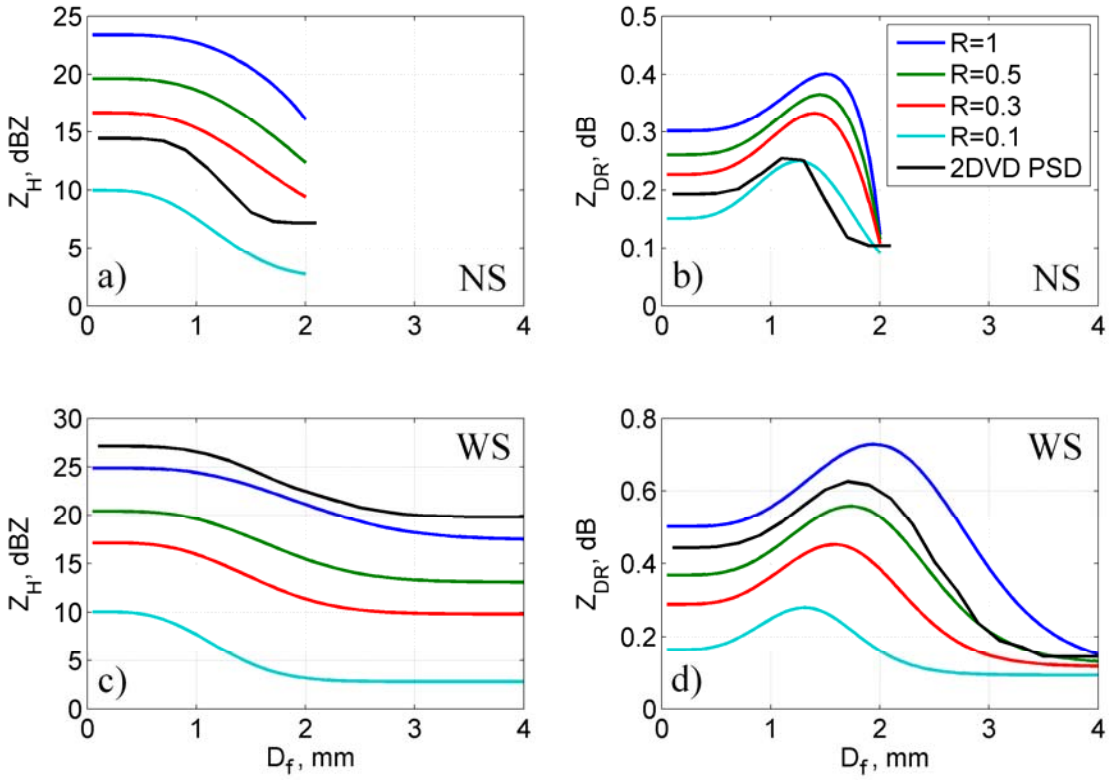



Figure 2.10: The impact of drops sequential freezing for two different size spectra on (a), (c) $Z_H$ and (b), (d) $Z_{DR}$ for the preferential freezing of small drops. $D_f$ is the largest frozen diameter below which all the drops are frozen for each PSD realization. Computations are for S-band, and Marshall-Palmer DSDs with different rainfall rates $R$ (mm h$^{-1}$) used (blue, green, red, and cyan represent 1, 0.5, 0.3, and 0.1 mm h$^{-1}$, respectively). The discretization of DSD is performed for the two spectral sizes: narrow size NS (top) and wide size WS (bottom) by sorting drops between 0.05 and 2 (4) mm in 40 (80) bins using 0.05 mm increments. Black lines are mean 2DVD PSD measurements from two main ice pellet periods, (a) and (b) from 0645 to 1100 UTC, and (c), (d) are from 1730 to 2130 UTC.

our simulations) after all drops are frozen, and is considerably less than before freezing started. This simple example suggests that refreezing signature may be hard to observe, and the increase in $Z_{DR}$ for ongoing freezing is likely followed by the subsequent tangible decrease as the number of larger frozen drops increases. To further validate MP-model simulations, 2DVD-measured average PSDs from the primary and secondary ice pellet periods (0645 to 1100 UTC, Fig. 10a-b, and 1730 to 2130 UTC, Fig. 10c-d) are sequentially frozen and presented as black lines ($Z_H$, $Z_{DR}$) in Fig. 2.10. Both 2DVD-measured $Z_H$ and $Z_{DR}$ have a similar shape compared to MP-model when sequential freezing occurs. During the primary IP period (0645 to 1100 UTC), when measured PSDs were narrow ($D$ < 2 mm), $Z_H$ and $Z_{DR}$ curves fall between MP simulated $R$ = 0.1 mm $h^{-1}$ and $R$ = 0.3 mm $h^{-1}$, while mean measured $R_{ip}$ is 0.21 mm $h^{-1}$. During the secondary IP period (1730 to 2130 UTC), the shape of the measured $Z_H$ and $Z_{DR}$ curves are similar to MP simulations, but $Z_{DR}$ falls between $R$ = 0.5 mm $h^{-1}$ and $R$ = 1 mm $h^{-1}$, while $Z_H$ is higher than the one calculated for $R$ = 1 mm $h^{-1}$. Mean measured $R_{ip}$ = 1.68 mm $h^{-1}$, which is very close to the value expected for MP-$Z_H$ for the same $R$. In general, the discrepancies in $Z_{DR}$ are likely due to differences between measured (averaged) and MP-simulated PSD, and the choice of the aspect ratio and canting angle can highly affect $Z_{DR}$ magnitude. Disdrometer measurements agree well with the simulations and increase confidence in the preferential drop freezing hypothesis.

*e. Radar-disdrometer comparisons*

Radar-disdrometer comparisons are presented in Figs. 2.11 and 2.12 for 0° and 0.41° beam elevations, respectively. In this case, the variables are $Z_H$ and $Z_{DR}$ and retrieved microphysical parameters $R_r$ and $D_{0r}$. One should be aware of 2DVD

measurement error sources: they are most frequently induced by drop splashing (Kruger and Krajewski 2002), wind effects in precipitation measurements (Nešpor et al. 2000), and particle mismatching (Huang et al. 2010, 2014) in case of the snow. In the initial and late storm stage, the difference between radar-measured (red dotted line in Fig. 2.11a, 0° elevation angle) and 2DVD-calculated $Z_H$ (assuming liquid water, black dots in Fig. 2.11a) is ~6-7 dB, primarily due to the difference between the refractive indices of liquid and ice hydrometeors. After replacing the dielectric constant of water with that

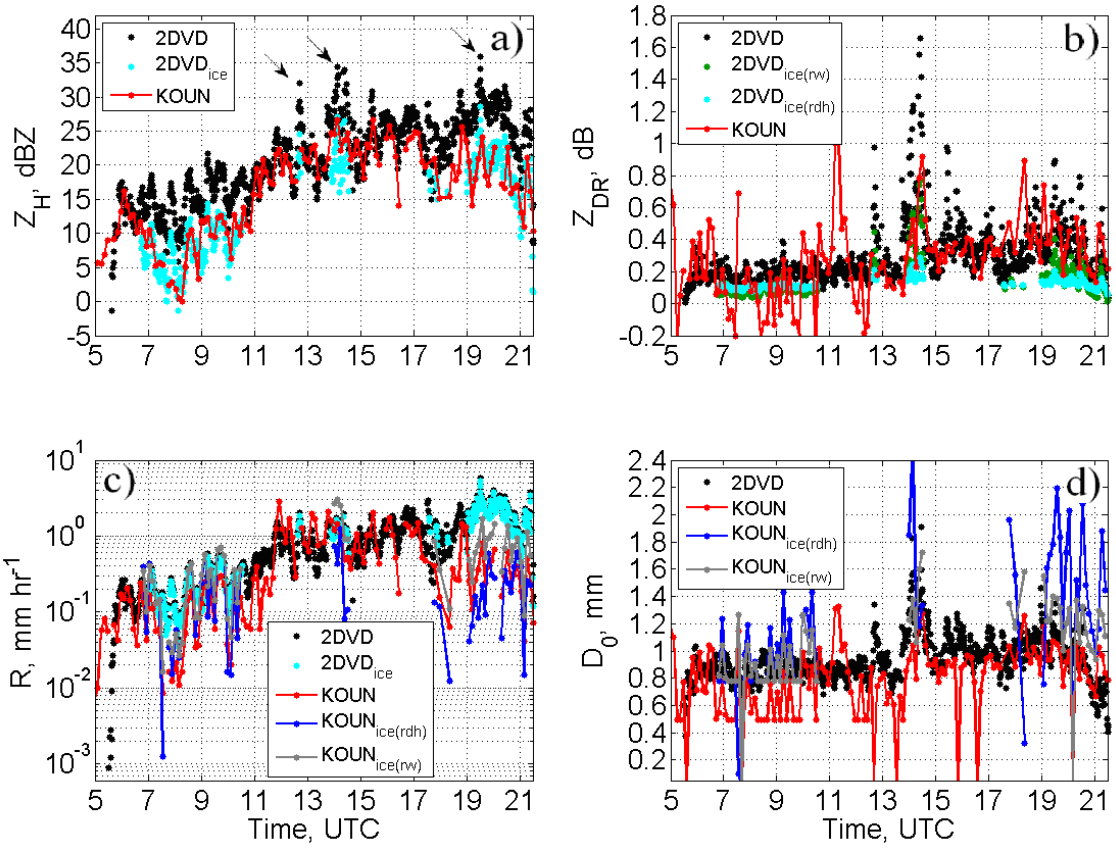



Figure 2.11: Comparison of (a) $Z_H$, (b) $Z_{DR}$, (c) rainfall rate, where the ice phase adjustment are in cyan (small dry hail aspect ratio) and green (raindrops aspect ratio) dots for 2DVD, and in blue dotted (small dry hail aspect ratio) and gray dotted (raindrops aspect ratio) line for KOUN, and (d) median volume diameter, obtained from radar DSD retrieval (KOUN) and disdrometer, time series for 0° KOUN elevation angle. Black arrows in (a) represent short periods of relatively big discrepancies between radar and 2DVD characterized as ice pellets.

of ice, and recalculating scattering amplitudes using Rayleigh-Gans approximation for the period from 0645 to 1100 UTC, and 1730 to 2130 UTC, the results for $Z_H$ are in much better agreement (Fig. 2.11a, cyan dots), while $Z_{DR}$ results are slightly better (Fig. 2.11b, cyan, and green dots). For both $Z_H$ and $Z_{DR}$ ice phase calculations, two axis ratios are used: $r_{dh}$ (Eq. 2.8) and $r_w$ (Eq. 2.9). The axis ratio $r_{dh}$ is the ratio of the vertical over horizontal axis for small dry hail (Ryzhkov et al. 2011b) while $r_w$ represent the axis ratio of the raindrops (Brandes et al. 2002). There is not a large difference between $Z_H$ values obtained from different axis ratios (for simplicity only cyan dots obtained from $r_{dh}$ are shown in Fig. 2.11a), but $Z_{DR}$ values are susceptible to change in particle shape as seen in Fig. 2.11b, where cyan dots are obtained from $r_{dh}$ and green dots from $r_w$ computations. In the primary IP period, the values of $Z_{DR}$ obtained through $r_{dh}$ and $r_w$ are comparable, but in the secondary IP periods, $r_w$ $Z_{DR}$ values (green dots, Fig. 2.11b) are in slightly better agreement with the measured radar $Z_{DR}$ (red dotted line, Fig. 2.11b). As a reminder, black dots represent 2DVD $Z_{DR}$ computed with the dielectric constant of water and raindrop $r_w$ axis ratio. Taking this into account, along with the RUC analysis soundings and SVPs, the observed trends in polarimetric variables are caused by the liquid to ice phase transition that characterizes ice pellet formation.

Radar retrieved rainfall rate $R_r$ (red dotted line in Fig. 2.11c) is in slightly better agreement with the disdrometer after the 2DVD ice phase adjustment (Fig. 2.11c, cyan dots; it is $R_{ip}$ after the ice phase adjustment instead of $R$), but the relative difference is still large for the period from 0645 to 1100 UTC and from ~1730 to 2130 UTC. This is mostly due to the assumption that the precipitation type is rain in radar $R_r$ (red dotted line) retrieval. After the ice phase adjustment for radar retrieved IP rate, $R_{ipr}$ (blue dotted

line – $R_{ipr}$ retrieved using $r_{dh}$, and gray dotted line – $R_{ipr}$ retrieved using $r_w$ in Fig. 2.11c) is in better agreement with 2DVD ice phase adjustment for the primary IP period (except for the few outliers). $R_{ipr}$ retrieved using $r_w$ is comparable with the $R_{ipr}$ obtained using $r_{dh}$ but in slightly better agreement with $R_{ip}$ from 2DVD. For later IP periods $r_{dh}$ $R_{ipr}$ retrieval (blue dotted lines, Fig. 2.11c) degrades even more than retrieved $R_r$ (red dotted line in Fig. 2.11c), while $r_w$ $R_{ipr}$ (gray dotted line, Fig. 2.11c) is in fairly good agreement for all IP periods. It seems that currently-used, direct-radar retrieval algorithms underestimate the precipitation rate during the occurrence of ice pellets, but this could be adjusted with more suitable axis ratio and particle density relations. In addition, the low concentration of precipitation particles imposes a restriction during the ice phase periods, limiting the accuracy of DSD measurements and radar DSD retrievals. In general, the radar retrieved and 2DVD measured rain rates are in fair agreement; during the ice phases there are moderate improvements for the IP periods using the raindrops axis ratios, but not for the later ones if the axis ratios of dry hail are used for the ice phase adjustment. Radar retrieved median volume diameter (red dotted line in Fig. 2.11d, liquid phase assumption), especially for the primary ice phase period (0645 until 1100 UTC), is noisy and with a much larger range of values compared to the 2DVD measurements. In the later stages the two are in fair agreement, with retrieved values slightly underestimated ($D_{0r}$ between 0.8 and 1.2 mm). Adjusting for the ice phase, radar-retrieved $D_{0r}$ agrees much better with the 2DVD-measured one for the primary IP period. The results from $r_w$ $D_{0r}$ (gray dotted line, Fig. 2.11d) are slightly better than the ones from $r_{dh}$ $D_{0r}$ (blue dotted line, Fig. 2.11d). In later IP periods, $r_{dh}$ $D_{0r}$

retrievals substantially degrade while $r_w$ $D_{0r}$ retrievals are in fair to good agreement with 2DVD.

It is very informative to take a look at radar-disdrometer comparisons at the next available radar beam elevation, 0.41°. As seen in Fig. 2.12a, the biggest differences between the radar-measured (red dotted line in Fig. 2.12a) and the 2DVD-calculated $Z_H$ (assuming liquid water, black dots in Fig. 2.12a) is ~6-7 dB and occurred in the initial storm stage (0645 to 0920 UTC). This is primarily due to the differences between the

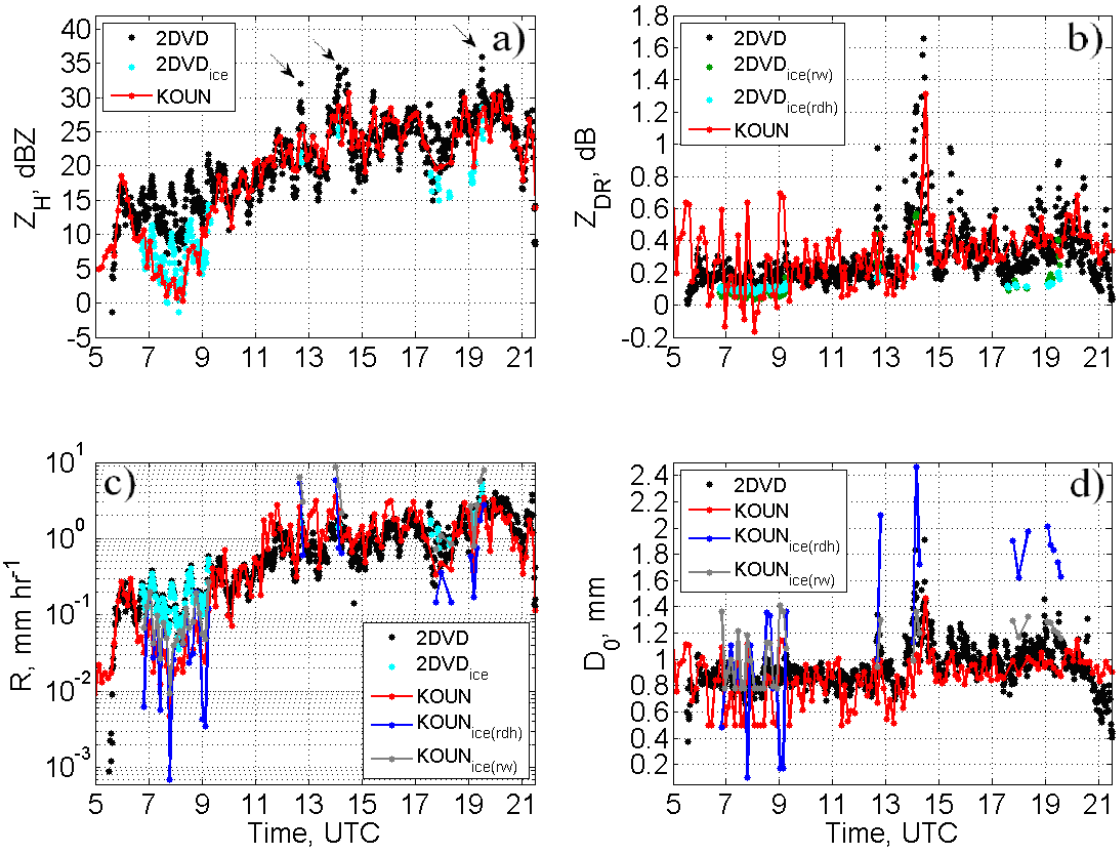



Figure 2.12: Comparison of (a) $Z_H$, (b) $Z_{DR}$, (c) rainfall rate, where the ice phase adjustment are in cyan (small dry hail aspect ratio) and green (raindrops aspect ratio) dots for 2DVD, and in blue dotted (small dry hail aspect ratio) and gray dotted (raindrops aspect ratio) line for KOUN, and (d) median volume diameter, obtained from radar DSD retrieval (KOUN) and disdrometer, time series for 0.41° KOUN elevation angle. Black arrows in (a) represent short periods of relatively big discrepancies between radar and 2DVD characterized as ice pellets.

refractive indices of liquid and ice hydrometeors. After replacing the dielectric constant of water with that of ice, and recalculating scattering amplitudes using Rayleigh-Gans approximation for the period from 0645 to 0920 UTC, the results for $Z_H$ are in much better agreement (Fig. 2.12a, cyan dots). This confirms that at both the 0° and 0.41° radar elevations refreezing occurred, with slightly shorter duration at the 0.41° elevation. From 0645 until 0920 UTC, the radar-measured $Z_{DR}$ is noisy and the results obtained from $r_{dh}$ 2DVD calculations (Fig. 2.12b, cyan dots) are in slightly better agreement than those obtained from $r_w$. In later IP periods (from 1730 to 1910 UTC) 2DVD calculated $Z_{DR}$ using both $r_{dh}$ and $r_w$ are in worse agreement with the radar than the ones calculated for pure liquid phase (black dots, Fig. 2.12b). This is likely due to beam smoothing of the liquid contribution because during this period the refreezing level height is lower than during the initial IP period while the melting layer is deeper and stronger. Clearly, the refreezing processes can be localized and altitude-dependent, and if shallow and far from radar, are hard to detect.

Radar retrieved rainfall rate $R_r$ (red dotted line in Fig. 2.12c) is in slightly better agreement with 2DVD after the ice phase adjustment (Fig. 2.12c, cyan dots; it is rather $R_{ip}$ after the ice phase adjustment instead of $R$), but the relative difference is still big for the period 0645 to 0920 UTC and at ~1730, 1815, and 1905 UTC. After the ice phase adjustment for radar retrieved IP rate using the dry hail axis ratio $r_{dh}$, $R_{ipr}$ (blue dotted line in Fig. 2.12c) is in better agreement with the 2DVD ice phase adjustment during the primary IP period (except for the few outliers), but degrades even more than retrieved $R_r$ in later IP periods. The best agreement between radar retrieved $R_{ipr}$ and the one calculated from 2DVD is achieved if $r_w$ is used for retrievals of $R_{ipr}$. The low

concentration of precipitation particles during the ice phase periods is restricting the accuracy of DSD measurements and radar DSD retrievals. In general, the differences between radar-retrieved and 2DVD-measured rain rates are in fair agreement, while during the ice phase there are possible improvements which depend on the choice of the ice pellets axis ratios. Radar retrieved median volume diameter (red dotted line in Fig. 2.12d, liquid phase assumption), especially during the first ice phase period (0645 until 0920 UTC), is noisy and fluctuates much more compared to the 2DVD measurements. In the later stages, the two are in fair agreement, with the values of $D_{0r}$ between 0.8 and 1.1 mm. The peak of radar retrieved $D_{0r}$ (1.5mm) occurred ~1440 UTC corresponds to relatively high values of $Z_{DR}$ (1.5 dB) caused by few large particles. Overall, the results during the rain periods agree well. After accounting for the ice phase (blue dotted line-using $r_{dh}$ and gray dotted line-using $r_w$ in Fig. 2.12d) $D_{0r}$ retrieval is in better agreement with 2DVD measurements in the primary IP period (except for the few outliers), but degrades substantially in the later ice pellet periods if the dry hail $r_{dh}$ axis ratio is used.

Besides the discrepancies occurring in the two main ice phase transitions, there have been a few other short periods with relatively large differences between radar and 2DVD measurements. These periods are marked with black arrows in Figs. 2.11a and 2.12a at 1245, 1410 and 1930 UTC. The distinction with regard to the main IP periods is in the relatively larger $Z_{DR}$ (0.4 to 0.8 dB) difference between the instruments (with respect to the liquid phase assumption in the 2DVD calculations, black dots in Figs. 2.11 and 2.12), along with the 4-7 dB difference in $Z_H$. A closer analysis of 2DVD DSD data (Fig. 2.5a) indicates that the concentration of the particles during these periods is slightly lower compared to values in adjacent times when fewer large particles are

present. The jump in particle sizes is also seen in 2DVD $D_0$ measurements. In the SVPs from these periods, there are short episodes of weak to moderate local enhancements in $Z_H$, $Z_{DR}$, and $\rho_{hv}$ at the times of interest. This is indicative of rain. Since the particles classified with 2DVD are ice pellets, the differences most likely originate from the much larger area over which the radar data are averaged (20° in azimuth for SVPs), or because of the short temporal scales of the refreezing episodes.

## 5. Discussion

An observational study of 20 January 2007 winter precipitation event using S-band polarimetric KOUN radar data and OU 2DVD measurements in Oklahoma is presented. The case is classified as a wintery mix of ice pellets and rain/freezing rain periods. RUC analysis and RASS profiles provide insight into environmental conditions, while storm structure and evolution are studied using the polarimetric radar and disdrometer observations. The PPI of $Z_H$, $Z_{DR,}$ and $\rho_{hv}$ revealed the morphology of the storm. Refreezing occurred locally at a distance of 30-40 km from the radar and exhibited a patchy structure of weakly enhanced $Z_{DR}$ (up to 0.2-0.3 dB) and reduced $Z_H$ and $\rho_{hv}$ values.

Radar-measured vertical profiles and time evolution of $Z_H$, $Z_{DR}$, and $\rho_{hv}$ over the disdrometer site are extracted from volume scans and analyzed. Radar vertical profiles presented in somewhat enhanced vertical resolution (dubbed as Enhanced Vertical Profiles - EVPs) show a reduction in $Z_H$ and $\rho_{hv}$, and very weak enhancement in $Z_{DR}$ as rain on its descent is transitioning to ice pellets. Coarser vertical resolution of regular profiles hints at some of the refreezing episodes but misses other signatures and hence is

deficient compared to the EVPs. The EVPs can moderately improve vertical resolution and continuity and therefore better isolate the refreezing signatures. A novel technique of polarimetric radar data processing/viewing, the Slanted Vertical Profiles (SVPs) at lowest elevations, is used for semi-quantitative analysis. This technique improves the diagnostics of localized refreezing at locations away from the radar because it enhances vertical resolution. In the case of homogeneous precipitation over large areas, the whole profile (top to bottom) can be interpreted for microphysical inferences within the vertical column. But, in horizontally non-homogeneous precipitation as was the case in our study the SVP is not representative of the true vertical column. Nonetheless, incremental values centered at a fixed height can represent well the actual variables at the corresponding range. The time evolution of the DSD, mass, reflectivity, and differential reflectivity distributions obtained with the 2DVD are examined. These generally show narrower distributions and lower particle concentrations during the ice phase periods compared to rain periods. Polarimetric radar variables were calculated from 2DVD data and compared with KOUN radar measurements, while radar retrieved raindrop size distributions (DSDs) are compared with the disdrometer measurements. Polarimetric variables $Z_H$ and $Z_{DR}$, as well as microphysical parameters of radar retrieved DSDs, rainfall rate ($R_r$) and median volume diameter ($D_{0r}$), generally agree well with 2DVD calculations/measurements, although discrepancies occur during the time of the ice phase if this phase transition is not recognized.

Estimates of radar $Z_H$ in which the correct precipitation phase is assumed improves significantly agreement with computed $Z_H$ from the 2DVD. However, improvement in $Z_{DR}$ is marginal. This is because ice pellets and small raindrops have

similar values of $Z_{DR}$. Using a novel approach - the SVPs at low elevations, and an in situ instrument (2DVD) makes it possible to extend remote measurements from the ground into the area above. In this case in situ observations and remote radar measurements are consistent with the observations of ice pellets.

## 6. Summary

The following summarizes principal findings of this paper:

1) Recognition of ice pellets with the polarimetric radar in localized areas up to about 50 km away from the radar is challenging. It is doable if the melting layer and refreezing layer are spaced by more than the beamwidth and refreezing is not below the radar horizon. Benefiting from previous observations, collocated 2DVD, and other measurements we were able not only to confirm the refreezing signatures but also to quantify the amount of frozen precipitation.

2) Slow falling (1 to 3 m $s^{-1}$) ice pellets were readily recognized in the 2DVD data. The rugged shapes of the pellets larger than 1.5 mm made these easily detectable at any fall speed. Because small drops freeze faster than large ones the presence of large pellets indicates that the smaller ones must be frozen too. This facilitated the overall discrimination.

3) The patchy refreezing structure in PPIs is in contrast to Ryzhkov et al.'s (2011a) and Kumjian et al.'s (2013) observations where the increase in $Z_{DR}$ and the reduction in $\rho_{hv}$ have ring-like structures while a reduction in $Z_H$ (by about 7 dB same as in our case) was more gradual. The differences can be due to the locality of our measurements where the refreezing processes occurred much closer to the ground. Polarimetric

signature of local enhancement in $Z_{DR}$ and reduction in both $Z_H$ and $\rho_{hv}$ is the same, except the magnitude of $Z_{DR}$ enhancement due to refreezing of smaller sizes (0.1 to 0.3 dB) is lower in our study. This is due to smaller particle size spectra during the ice phase.

4) Environmental conditions, such as the presence of melting and freezing layers, and also freezing temperatures not colder than -3.5°C within refreezing zones, indicated that preferential freezing of smaller drops is most likely the mechanism which produces the refreezing polarimetric signatures.

5) The magnitudes of $Z_H$, $Z_{DR}$, and $\rho_{hv}$ per se are not sufficient for identifying refreezing, but their spatial and temporal changes reveal the locations of refreezing.

6) Simulations of preferential drop freezing suggest complexity in the refreezing signatures, such as dependence on the width of the particle size spectra, and particle sizes (smaller drops freeze faster), in conjunction with the environmental conditions (e.g., temperature and relative humidity). The simulated refreezing signature of $Z_{DR}$ is especially instructive: $Z_{DR}$ increases during preferential freezing, but after larger drops start to freeze it drops substantially (depending on the particle size), as confirmed by 2DVD measurements. This indirectly indicates that the refreezing signatures are altitude (due to temperature) dependent and that the enhancement of the $Z_{DR}$ may be followed by a substantial reduction over a small vertical distance.

# Chapter 3: Polarimetric Relations for Quantification of Snow Based on Disdrometer Data

## 1. Introduction

Radar measurements of snow are challenging due to tremendous variability of snow particle size distributions (PSDs), density, water content, shape, orientation, crystal habits, etc. Thus, radar quantitative precipitation estimation (QPE) of snow is very difficult (Mitchell et al. 1990).

There have been many radar-based studies on the estimation of snowfall rates in the past half-century. The vast majority of these studies utilize power-law relations between the equivalent radar reflectivity ($Z_e$, herein $Z$) and liquid water equivalent snowfall rate ($S$, also LWE), $Z = aS^b$ (e.g., Gunn and Marshall 1958; Ohtake and Henmi 1970; Sekhon and Srivastava 1970; Puhakka 1975; Fujiyoshi et al. 1990; Koistinen et al. 2003; Matrosov et al. 2007, 2009; Huang et al. 2010; Szyrmer and Zawadzki 2010; Zhang et al. 2011; Wolfe and Snider 2012; Heymsfield et al. 2016; etc.). Most of these relations assume that $Z$ is proportional to $S^2$. The multitude of power-law $Z - S$ relations (some of which are presented in Table 3.1 and Figure 3.1) exhibit roughly an order of magnitude difference in the estimates of snowfall rate for the same reflectivity factor $Z$. None of the previous studies have capitalized on the emergence of polarimetric radar capabilities for estimation of $S$.

Ice water content (IWC) is another important microphysical parameter characterizing glaciated parts of clouds. There have been a number of studies in which the IWC of clouds is estimated using radar reflectivity factor $Z$ in the form of IWC = $cZ^d$ (e.g., Sekhon and Srivastava 1970; Heymsfield 1977; Sassen 1987; Atlas et al.

| Source | $Z(S)$ relation for dry snow |
|---|---|
| Gunn and Marshall 1958 | $Z = 448\ S^2$ |
| Sekhon and Srivastava 1970 | $Z = 399\ S^{2.21}$ |
| Ohtake and Henmi 1970 | $Z = 739\ S^{1.7}$ |
| Puhakka 1975 | $Z = 235\ S^2$ |
| Koistinen et al. 2003 | $Z = 400\ S^2$ |
| Huang et al. 2010 | $Z = (106 – 305)\ S^{(1.11 – 1.92)}$ |
| Szyrmer and Zawadzki 2010 | $Z = 494\ S^{1.44}$ |
| Wolfe and Snider 2012 | $Z = 110\ S^2$ |
| WSR-88D, Northeast | $Z = 120\ S^2$ |
| WSR-88D, North Plains / Upper Midwest | $Z = 180\ S^2$ |
| WSR-88D, High Plains | $Z = 130\ S^2$ |
| WSR-88D, Inter-mountain West | $Z = 40\ S^2$ |
| WSR-88D, Sierra Nevada | $Z = 222\ S^2$ |

Table 3.1: Summary of $Z(S)$ relations for dry snow listed in literature and utilized by the WSR-88D network in the US.

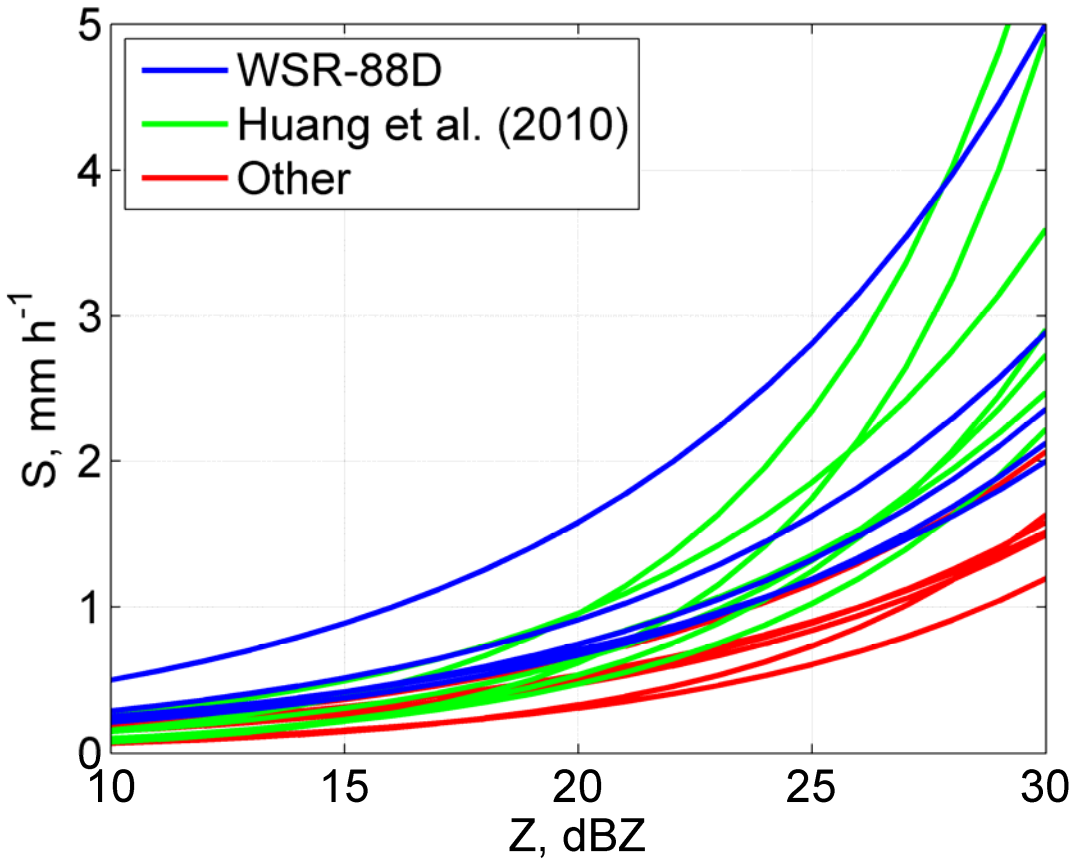



Figure 3.1: Summary of $Z(S)$ relations for dry snow listed in literature and utilized by the WSR-88D network in the US.

1995; Liu and Illingworth 2000; Hogan et al. 2006; Delanoë et al. 2014; Heymsfield et al. 2016).

The common thread in all of these studies is the large variability of $Z$-IWC relations in space (i.e., from cloud to cloud) and time (Ryzhkov et al. 1998). Adequately representing IWC in Numerical Weather Prediction (NWP) models is needed to improve Quantitative Precipitation Forecast (QPF) as well as global circulation and climate models because ice clouds strongly affect Earth's radiation balance (Stephens et al. 1990). This magnifies the importance of measuring the IWC in situ or remotely so that comparisons with model estimates can be made.

A few studies that explored polarimetric methods for IWC estimation are exposed next. Vivekanandan et al. (1994) advocate use of specific differential phase $K_{DP}$ for IWC estimation. Aydin and Tang (1995) combine $K_{DP}$ and differential reflectivity $Z_{DR}$ for IWC estimation in clouds composed of pristine ice crystals assuming that the density of crystals is equivalent to the density of solid ice. Ryzhkov et al. (1998) propose IWC estimation for pristine ice crystals (or lightly to moderately aggregated crystals) from a combination of $K_{DP}$ and reflectivity difference $Z_{DP}$ or $K_{DP}$ alone.

We use extensive snow disdrometer data – measured snow PSDs, collected in central Oklahoma from late 2006 until early 2015, to derive polarimetric relations for liquid water equivalent snow rate $S$ and ice water content IWC. Similarly, relations for intercept $N_{0s}$ and slope $\Lambda_s$ of an exponential size distribution are also derived from snow PSD measurements. For these relations, we choose a power-law form $V = \gamma K_{DP}^{\alpha} Z^{\beta}$, where $V$ represents any of the variables/parameters: $S$, IWC, $N_{0s}$ or $\Lambda_s$. Our proposed

methodology is applicable to the cloud depth from the ice crystal forming region through aggregation, which in winter storm often extends down to the ground. We submit that over such layer the flux of ice water is constant. In such cases, the $K_{DP}$ would decrease from the top down, whereas $Z$ would increase. Therefore a single relation using either of these two variables would miss the total amount. The combined relation compensates for these two opposing trends and more accurately quantifies the constant snow flux throughout the cloud depth.

The paper is organized as follows. Section 2 contains a description of the acquisition and processing of snow disdrometer data. A methodology for the computation of snow microphysical parameters $S$ and IWC, and polarimetric variables $Z$ and $K_{DP}$ is presented in section 3, whereas a theoretical background for $Z$-$S$ and $Z$-IWC parameterization is discussed in section 4. The results of disdrometer estimated $S$(2DVD) and IWC(2DVD) and expected $S$ and IWC from disdrometer data ($S(Z)$, $S(K_{DP})$, $S(K_{DP}, Z)$, IWC($Z$), IWC($K_{DP}$), IWC($K_{DP}$, $Z$)) are included in section 5, followed by a discussion and summary in sections 6 and 7.

## 2. Datasets and 2DVD processing

*a. Datasets*

The 2DVD observations of snow in central Oklahoma were made during the period from November 2006 until March 2015. The disdrometer was deployed at Kessler Atmospheric and Ecological Field Station (KAEFS), the University of Oklahoma (OU) test site approximately 15 km west of Purcell OK, at ~350 meters above sea level. Sixteen snow events were observed and a total of ~7000 one-minute

snow particle size distributions were sampled. Using the measurements of temperature and humidity most of the precipitation was classified as dry aggregated snow; the thermodynamic vertical profiles retrieved from the Rapid Update Cycle (RUC) or Rapid Refresh (RAP) models aided this classification. Episodes of mixed-phase precipitation were excluded from the dataset.

For nine out of sixteen snow events, snow water equivalent (SWE) amounts were recorded with nearby Oklahoma Mesonet (Washington) station, which are total melted SWE amounts from regular rain gauge (about 400 meters away from 2DVD). Since the acquisition of heated rain gauge (2013), we have compared the amounts with the Washington station (after melting) and found relatively good agreement. This gave us confidence in total snow water amounts collected previously.

Until 2014, there was no wind measurement directly at the Oklahoma 2DVD site, but 400 m away on the hill. After the wind sensor installation at the 2DVD site, the measurements between these two locations indicate an average difference of about 1 to 4 m/s (median is ~3 m/s), with higher winds on top of the hill. Application of this correlation to all Oklahoma snow events revealed only few short periods with winds above 4 m/s in 4 of 16 events. We excluded these from the analysis but used them for the estimation of the total SWE amounts. The rest of the events (including Colorado and Canada 2DVD measurements) had ambient wind speeds less than 4 m/s.

*b. 2DVD processing*

The 2D video disdrometer (2DVD) (Kruger and Krajewski 2002; Schönhuber et al. 2008) is an optical instrument which directly measures the particles' size, shape, and terminal velocity, allowing for the construction of particle size distributions (PSDs).

The horizontal resolution of 2DVD measurements is approximately 0.2 mm while the vertical resolution depends on the hydrometeors' terminal velocities and ranges from 0.05 to 0.2 mm. The particles are partitioned into 101 size bins, each 0.2 mm wide and centered at diameters ranging from 0.1 to 20.1 mm.

The instrument has two line scan cameras placed orthogonally, with planes of view separated by about 6.2-7.0 mm and illuminated by two light sources. It was originally designed for raindrop size distribution and shape measurements. As a raindrop falls through the virtual measurement area, line cameras record two orthogonal views, so that it is fairly straightforward to match images and construct a 2D view of the drop. Because of the 6.2-7.0 mm vertical displacement between the cameras, it is possible to measure a raindrop's fall speed. Whereas it is rather easy to match two raindrop images due to their high symmetry with respect to the minor axis, it has been demonstrated that 2DVD snow data processing using manufacturer's proprietary software is problematic (Hanesch 1999; Huang et al. 2010, 2014).

A large amount of mismatching occurs in the case of snow because snow particles' diverse shapes produce dissimilar orthogonal images. Only the vertical dimensions of the particles (measured in a number of line scans) from two orthogonal cameras are suitable for matching. According to the manufacturer's matching software, the particle is considered matched if the vertical dimensions from the two orthogonal images are within certain tolerance. That way, the first two particles which pass the criteria are matched. A better matching procedure described by Huang et al. (2010) examines all possible pairs within a prescribed time window. Our attempt to use this matching criterion produced slightly higher particles' fall speeds than expected. After

the refinements, reflected in adding another membership function which utilized the ratio of measured versus empirical velocity, fall speeds agreed slightly better with the expected ones. Thus this approach was abandoned. Instead, we made adjustments to the original matching algorithm as follows.

We have applied an additional filter to the originally matched particles. Namely, the height ratio of the orthogonal images (denoted as $f_1$) and the ratio of the measured terminal velocity $V_m$ to the empirically predetermined value $V_e$ (denoted as $f_2$). These ratios are forced to be less than or equal to one,

$$f_1 = H_A/H_B \text{ if } H_A \leq H_B \text{ or } f_1 = H_B/H_A \text{ otherwise,} \quad (3.1)$$

$$f_2 = V_m/V_e \text{ if } V_m \leq V_e \text{ or } f_2 = V_e/V_m \text{ otherwise.} \quad (3.2)$$

In (3.1) – (3.2), $H_A$ and $H_B$ are the particle's heights measured by orthogonal cameras and $V_e$ is the empirical terminal velocity specified by Brandes et al. (2007, see section 3). Finally, the product $f_1 f_2$ is used as an adaptable threshold that depends on the measured amount of snow water equivalent (SWE) by a reference gauge. The values typically range between 0.5 and 0.65. In this way, the original 2DVD matching with all available statistics becomes usable and physically realistic.

The total SWE amounts are determined from Oklahoma Mesonet (Washington) rain gauge measurements. The data are filtered in the way described above, where the mean threshold is derived from the available SWE estimates. Additionally, due to the problem with our unit's cameras' focus for particles smaller than ~0.7 mm, extrapolation from the 1-minute measured distribution size range of 1-4 mm (if a total number of particles within this size range is equal to or larger than 6) is used to quantify

PSDs at particle sizes less than 1 mm. For the distributions with a number of particles less than 6 within the prescribed size range, measured distributions are accepted as is.

## 3. Methodology

The snow water equivalent rate S expressed in mm $h^{-1}$ is computed as

$$S = \frac{\pi}{6\Delta t}\sum_{i=1}^{L}\frac{\rho_s(D_i)}{\rho_w}\frac{C(D_i)D_i^3}{A(D_i)}. \quad (3.3)$$

The term $\Delta t$ is summation time period in hours, $C(D_i)$ represents the number of particles collected in one minute in the $i^{th}$ size bin, $A(D_i)$ is the mean 2DVD effective area in $mm^2$ for the $i^{th}$ size bin, $D_i$ is the equivolume diameter representing the bin center in mm, $\rho_w$ and $\rho_s$ are the densities of water and snow in g $cm^{-3}$. For 1-minute summation period Eq. (3.3) simplifies to $S = 10\pi\sum_{i=1}^{L}\frac{\rho_s(D_i)}{\rho_w}\frac{C(D_i)D_i^3}{A(D_i)}$.

The IWC in g $m^{-3}$ is calculated via

$$\mathrm{IWC} = \frac{\pi}{6}10^{-3}\sum_{i=1}^{L}\rho_s(D_i)D_i^3N(D_i)\Delta D, \quad (3.4)$$

where $N(D_i)$ is the measured particle size distribution in $m^{-3}$ $mm^{-1}$.

There are multiple density-size relations in the literature (e.g., Brown and Francis 1995; Matrosov 1997; Brandes et al. 2007; Szyrmer and Zawadzki 2010; Tiira et al. 2016). These are usually between the mean snow density $<\rho_s>$ determined as a ratio of the total mass to total volume of snow in the whole size distribution and the median volume diameter $D_0$. For example, the relation from Brandes et al. (2007) is

$$<\rho_s> = 0.178\,D_0^{-0.922}. \quad (3.5)$$

It can be shown that for exponential size distribution the dependence $\rho_s(D)$, where $D$ (mm) is particle equivalent volume diameter, has the same exponent as the $<\rho_s(D_0)>$ relation but with a slightly different multiplier (about 18% smaller). Most of the density relations cited in the literature have the exponent close to -1, but the multiplier can vary significantly. Matrosov (1997) claims that the multiplier is higher for ice particles observed at higher altitudes (using in situ aircraft measurements) compared to particles observed near the surface (from ground measurements). The multiplier of the power-law density-size relation is higher for rimed snow. Zawadzki et al. (2005) use the degree of riming factor, $f_{\text{rim}}$, to account for riming of different intensity so that

$$\rho_s(D) = c_\rho f_{\text{rim}} D^{-\delta} \tag{3.6}$$

and $f_{\text{rim}} = 1$ for unrimed snow. Zhang et al. (2011) and Zhang (2016) recommend using the measured ratio $V_m(D)/V_e(D)$ to account for the change of the multiplier and variable degree of riming across the snow spectrum. Here, we follow the Zhang et al. (2011) and Zhang (2016) suggestion to estimate the degree of riming $f_{\text{rim}}$ as

$$f_{\text{rim}}(D) = \left[\frac{V_m(D)}{V_e(D)}\right]^2 \tag{3.7}$$

where

$$V_e(D) = 0.768\, D^{0.142} \tag{3.8}$$

is the relation obtained by Brandes et al. (2007) in Colorado (Marshall, National Center for Atmospheric Research Snowfall Test Site, at the height of 1742 m MSL). Velocity ratio in Eq. (3.7) could be regarded as a proxy for riming because the increase in the ratio of $V_m/V_e$ increases the degree of rimming. Due to the dependence of terminal velocity on air density, $V_m(D)$ in (3.7) should be adjusted to the air density at which Eq.

(3.7) is valid. This is done by multiplying $V_m$ with the square root of the ratio $\rho_a(O)/\rho_a(C)$ where $\rho_a(O)$ is the air density at the observational site and $\rho_a(C)$ is the standard air density at h = 1742 m MSL.

The intercept $N_{0s}$ (in $m^{-3}$ $mm^{-1}$) and slope $\Lambda_s$ (in $mm^{-1}$) of the exponential size distribution are determined from the 2DVD measured snow size distributions using the 2nd and 4th PSD moments. The nth moment of the PSD, where the second equality is valid only for exponential PSD model, is defined as

$$M_n = \int_0^\infty D^n N(D)\, dD = N_{0s} \Lambda_s^{-(n+1)} \Gamma(n+1). \tag{3.9}$$

Hence the parameters $\Lambda_s$ and $N_{0s}$ of the exponential size distribution can be computed as

$$\Lambda_s = (12 M_2 / M_4)^{1/2}, \tag{3.10}$$

and

$$N_{0s} = \frac{M_2 \Lambda_s^3}{2}. \tag{3.11}$$

The polarimetric variables are computed from 2DVD measurements as follows (Ryzhkov et al. 2011b):

$$Z = \frac{4\lambda^4}{\pi^4 |K_w|^2} \int_0^\infty \left\{ \left| s_a^{(\pi)} \right|^2 - 2\,\mathrm{Re}\left[ s_a^{(\pi)*} \left( s_a^{(\pi)} - s_b^{(\pi)} \right) \right] A_2 + \left| s_a^{(\pi)} - s_b^{(\pi)} \right|^2 A_4 \right\} N(D) dD, \tag{3.12}$$

$$K_{DP} = \frac{0.18\lambda}{\pi} \int_0^\infty \mathrm{Re}\left( s_a^{(0)} - s_b^{(0)} \right) A_7 N(D) dD, \tag{3.13}$$

where $Z$ is the reflectivity factor at horizontal polarization, and $K_{DP}$ is the specific differential phase in degree $km^{-1}$. In (3.12) and (3.13), $\lambda$ is the radar wavelength (in

mm), whereas the coefficients $A_2$, $A_4$, and $A_7$ are the angular moments of the canting angle distributions of hydrometeors:

$$A_2 = 0.25\left(1 - r^2\right), \tag{3.14}$$

$$A_4 = \left(0.375 - 0.5r + 0.125r^4\right)\left(0.375 + 0.5r + 0.125r^4\right), \text{ and} \tag{3.15}$$

$$A_7 = 0.5r\left(1 + r\right), \tag{3.16}$$

where $r = \exp(-2\sigma^2)$, and $\sigma$ is the width of the canting angle distribution (in the expression for $r$, $\sigma$ is in radians; for convenience, we express $\sigma$ in degrees throughout the text). Scattering amplitudes $s_{a,b}$ (in mm) are determined in the Rayleigh approximation for which the backward and forward scattering amplitudes (denoted with superscript ($\pi$) and (0) respectively) are the same, (i.e., $s_{a,b}^{(\pi)} = s_{a,b}^{(0)}$) and can be expressed as (Van de Hulst 1981)

$$s_{a,b}^{(\pi)} = s_{a,b}^{(0)} = \frac{\pi^2 D^3}{6\lambda^2} \frac{\varepsilon - 1}{L_{a,b}(\varepsilon - 1) + 1}, \tag{3.17}$$

with $\varepsilon$ representing the dielectric constant of dry snow (determined from the Maxwell-Garnett mixing formula); $L_{a,b}$ are the shape parameters given by

$$L_b = \frac{1 + g^2}{g^2}\left(1 - \frac{\arctan g}{g}\right), g = \sqrt{\frac{a^2}{b^2} - 1}, \text{ and, } L_a = \frac{1 - L_b}{2}. \tag{3.18}$$

Here $b/a$ is the aspect ratio of an oblate particle, hence $b < a$.

The specific differential phase $K_{DP}$ strongly depends on the particle shape and orientation (see the Appendix), while $Z$ is not much affected by these factors. Nonetheless, as shown by Hogan et al. (2012), the polarimetric radar variables in aggregated snow consisting of irregular ice particles can be computed with reasonable accuracy by modeling the scatterers as oblate spheroids with a vertical rotation axis

(i.e., $\sigma = 0°$) and aspect ratio of 0.6. Numerous studies of ice with aircraft in situ probes demonstrate that irregular aggregated particle comprise the bulk (up to 90%) of snow (Korolev et al. 2000) and, if larger than about 0.07 mm, typically have an axis ratio between 0.5 and 0.7 (Korolev and Isaac 2003). Garrett et al. (2015) found that the median axis ratio of unrimed aggregates is equal to 0.60 versus 0.70 for moderately rimed snowflakes in the observations with MASC (particles larger than 1 mm were examined). Thus, in our computations of $K_{DP}$ and $Z$ from the 2DVD measurements, we utilize an axis ratio $b/a = 0.65$ and $\sigma = 0°$.

## 4. Parameterization of the *Z*-*S* and *Z*-IWC relations for dry snow

*a. Parameterization of the Z-S and Z-IWC relations*

Following the approach of Rasmussen et al. (2003), theoretical $Z - S$ and $Z -$ IWC relations can be derived. As shown in the Appendix, these relations are parameterized by the intercept $N_{0s}$ and the degree of riming $f_{rim}$:

$$S = 2.26 \times 10^{-3} a_u f_{rim}^{0.07} N_{0s}^{0.37} Z^{0.63}, \tag{3.19}$$

and

$$\mathrm{IWC} = 4.95 \times 10^{-4} f_{rim}^{-0.19} N_{0s}^{0.4} Z^{0.6}. \tag{3.20}$$

It follows from (3.19) and (3.20) that the multipliers in the power-law $S - Z$ and IWC – $Z$ relations are almost entirely dependent on the intercept $N_{0s}$ of the exponential size distribution and are practically insensitive to the degree of riming $f_{rim}$.

We use our disdrometer dataset obtained from 16 snowstorms in Oklahoma to estimate $S$, IWC, $N_{0s}$, and $Z$ and to derive empirical $S(N_{0s}, Z)$ and IWC($N_{0s}$, $Z$) relations. As a first step, we plot $N_{0s}$ versus the ratio $S/Z^q$ with various values of the exponent q to

find an optimal value of q that yields the highest correlation coefficient between $N_{0s}$ and $S/Z^{q}$. As expected, the correlation is indeed very high and the maximal correlation coefficient (0.978) is achieved for q = 0.62. The corresponding scatterplot of $S/Z^{0.62}$ vs. $N_{0s}$ (Fig. 3.2) clearly demonstrates that the value of $S$ can vary more than an order of magnitude for a given $Z$ depending on $N_{0s}$, where the later can change four orders of magnitude. The best linear fit to the scatterplot in Fig. 3.2 is

$$S = 1.9 \times 10^{-3} N_{0s}^{0.35} Z^{0.62}, \tag{3.21}$$

with the exponents of $N_{0s}$ and $Z$ in excellent agreement with theoretical prediction specified in Eq. (3.19) (0.37 and 0.63 respectively).

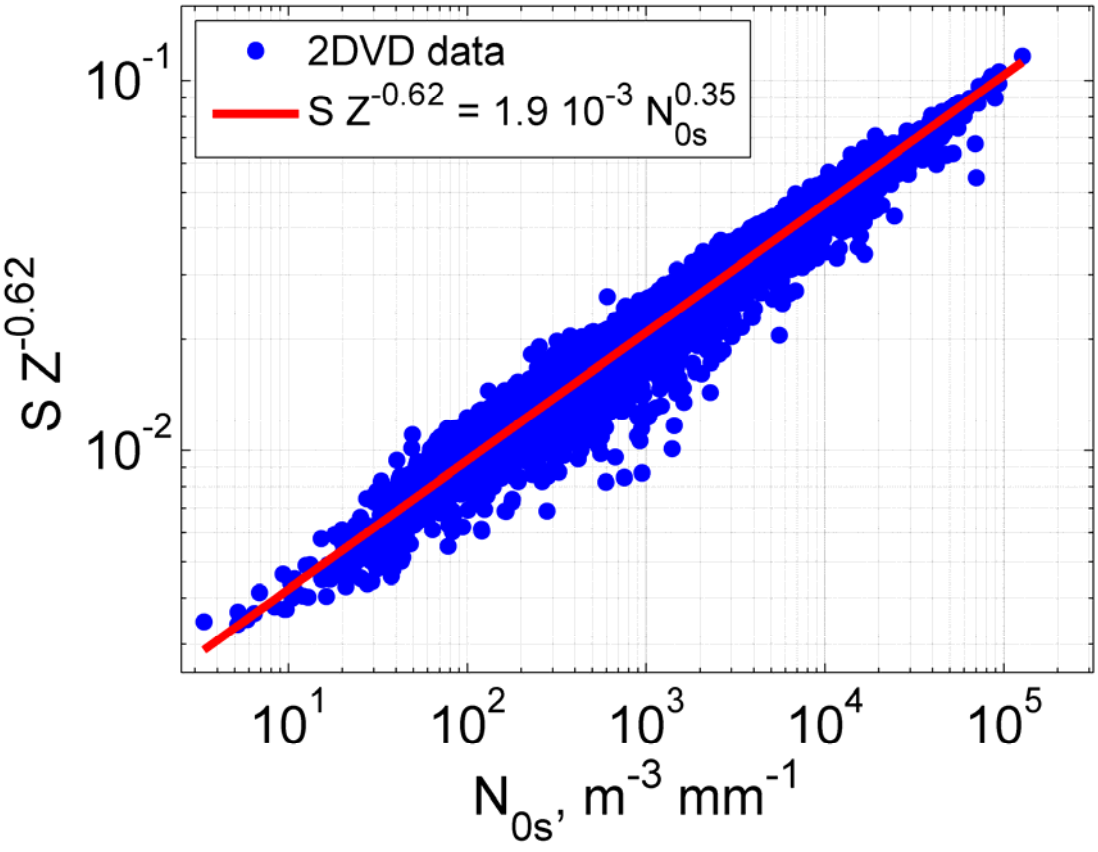



Figure 3.2: Scatterplot of $N_{0s}$ vs. $S/Z^{0.62}$ ($\log_{10}$ scale, correlation coefficient = 0.978) from 2DVD estimations and computations (blue dots). The best fit to 2DVD data, $S\ Z^{-0.62} = 1.9\ 10^{-3}\ N_{0s}^{0.35}$, is overlaid as red line.

A similar analysis for IWC yields

$$\mathrm{IWC} = 5.26\times10^{-4} N_{0s}^{0.38} Z^{0.58} \tag{3.22}$$

and the corresponding scatterplot is presented in Fig. 3.3. Again, the exponents in the empirical best fit are very consistent with the ones in the theoretical formula (3.20) and agree well with the results of in situ measurements with aircraft probes in various types of clouds. The latter are summarized in the studies of Hogan et al. (2012) and Delanoë et al. (2014), where the relations $\mathrm{IWC} \sim N_{0s}^{0.4} Z^{0.6}$ and $\mathrm{IWC} \sim N_{0s}^{0.42} Z^{0.58}$ were suggested.

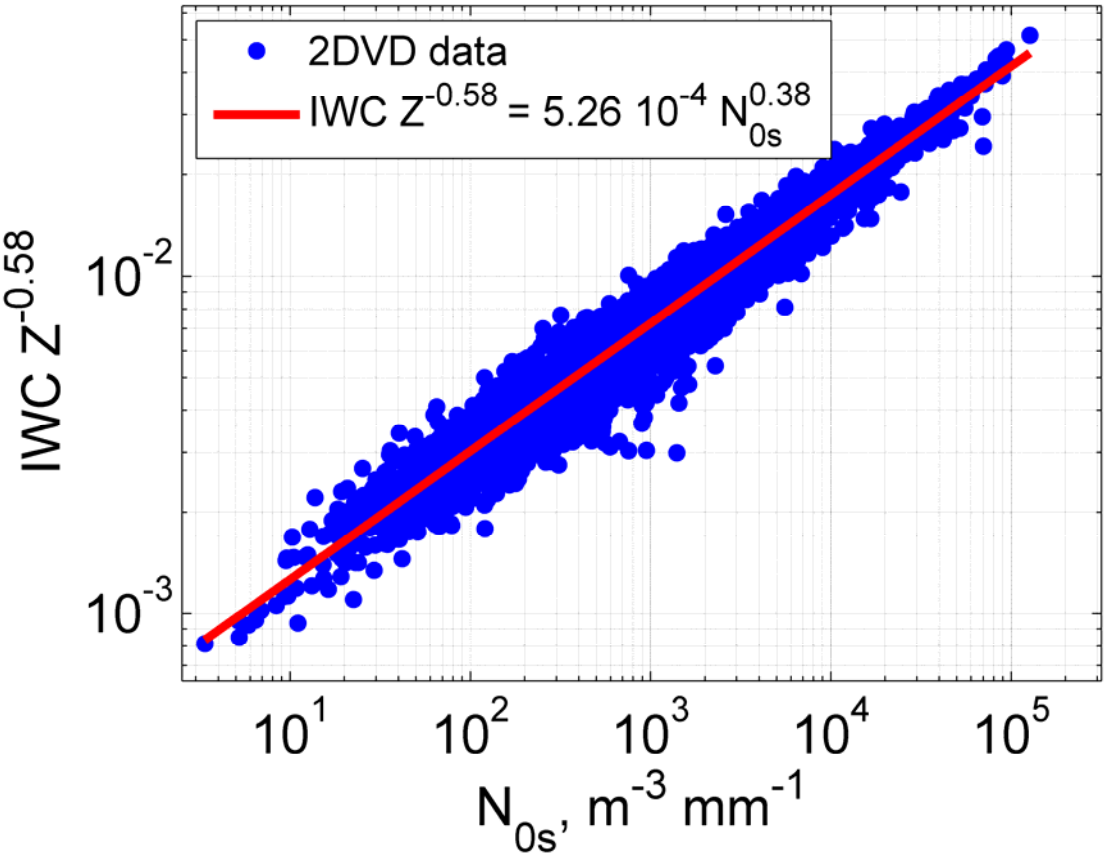



Figure 3.3: Scatterplot of $N_{0s}$ vs. IWC/$Z^{0.58}$ ($\log_{10}$ scale, correlation coefficient = 0.977) from 2DVD estimations and computations (blue dots). The best fit to 2DVD data, IWC $Z^{-0.58} = 5.26\ 10^{-4}\ N_{0s}^{0.38}$, is overlaid as red line.

The strong dependence of the multipliers in the $S - Z$ and IWC $- Z$ relations on the concentration of snow particles (which can be approximated by the intercept $N_{0s}$) precludes their effective use for quantification of snow. The ubiquitous presence of dual-polarization weather radars motivates the exploration of alternatives. One of these is to classify snow types using polarimetric variables and then apply $S(Z)$ or IWC($Z$) relations corresponding to the particular snow type. Differential reflectivity $Z_{DR}$ can be a good candidate for snow classification but not for quantification. $Z_{DR}$ is insensitive to concentrations of snowflakes which cause the largest uncertainty in the $S(Z)$ or IWC($Z$) relations, as Figs. 3.2 and 3.3 demonstrate.

Another possibility is to use $K_{DP}$ which is directly proportional to $N_{0s}$. Vivekanandan et al. (1994) and Ryzhkov et al. (1998) reported promising results in the estimation of IWC from $K_{DP}$ for pristine or lightly aggregated ice crystals. That approach may not work well for aggregated or irregular snowflakes because $K_{DP}$ is proportional to the first moment of PSD whereas $S$ and IWC are close to the second moment of PSD for low-density snow (see the Appendix). Nevertheless, we tried this path and came up with the following $S(K_{DP})$ and IWC($K_{DP}$) relations at S-band using our disdrometer dataset:

$$S(K_{DP}) = 55.63\, K_{DP}^{1.08}, \tag{3.23}$$

and,

$$\mathrm{IWC}(K_{DP}) = 14.44\, K_{DP}^{1.05}. \tag{3.24}$$

Because exponential size distributions are characterized with two parameters, $N_{0s}$ and $\Lambda_s$, it is possible to estimate these from two radar variables. We chose the

combination of $Z$ and $K_{DP}$, and from the same disdrometer dataset, we obtained the following relations

$$N_{0s}(K_{DP}, Z) = 15.3 \times 10^7 K_{DP}^{1.72} Z^{-0.79} \tag{3.25}$$

and

$$\Lambda_s(K_{DP}, Z) = 39\, K_{DP}^{0.36} Z^{-0.35}. \tag{3.26}$$

Both parameters exhibit a tight fit (Fig. 3.4). The high correlation with their 2DVD estimates from method of moments (0.971 for $N_{0s}$ and 0.985 for $\Lambda_s$), suggests that (3.25) and (3.26) may enable polarimetric radar retrieval of snow microphysical parameters. From (3.25) and (3.26) it is easy to compute the exponential snow PSD, from which in turn the $S$ and IWC can be computed. The disadvantage of such approach is that the

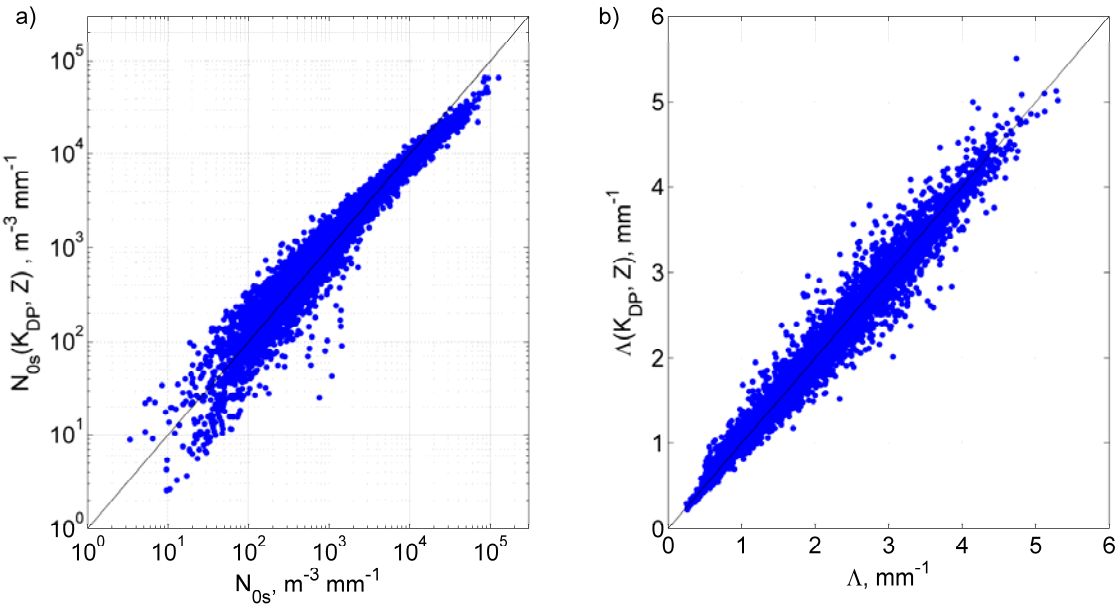



Figure 3.4: Scatterplots of: a) $N_{0s}$(2DVD) vs. $N_{0s}(K_{DP}, Z)$ ($\log_{10}$ scale, correlation coefficient = 0.971); b) $\Lambda_s$(2DVD) vs. $\Lambda_s(K_{DP}, Z)$ (correlation coefficient = 0.985).

PSD is assumed to be exponential, and thus not directly measured.

Another possibility is to use direct combination of $Z$ and $K_{DP}$ to express $S$ and IWC. The reasoning is that $Z$ is close to the fourth moment while $K_{DP}$ is proportional to the first moment of PSD for a low-density (aggregated) snow. Therefore the product of $K_{DP}$ and $Z$ with certain exponents might be more directly related to the second moment of PSD, and thus we search for solutions of the form $S \sim K_{DP}^{\alpha_1} Z^{\beta_1}$, and $\mathrm{IWC} \sim K_{DP}^{\alpha_2} Z^{\beta_2}$.

A direct approach independent of the two parameters of PSD obtains the $S$ and IWC via multivariate linear fitting or the logarithms of $S$, IWC, $Z$, and $K_{DP}$. This way, the following $S(K_{DP}, Z)$ and $\mathrm{IWC}(K_{DP}, Z)$ are obtained from our disdrometer dataset:

$$S(K_{DP}, Z) = 1.48\, K_{DP}^{0.61} Z^{0.33} \tag{3.27}$$

and

$$\mathrm{IWC}(K_{DP}, Z) = 0.71\, K_{DP}^{0.65} Z^{0.28}. \tag{3.28}$$

*b. Relation between IWC and S*

Heymsfield et al. (2016) showed that the logarithms of IWC and $S$ are linearly related implying that the relation on linear scale follows a power law. Indeed, estimated values from disdrometer data (Fig. 3.5) indicate a slightly quadratic fit form $S$ = 0.406 $\mathrm{IWC}^2$ + 3.34 IWC - 0.001 (black dots in Fig. 3.5; this relation is valid for IWC > 0.00042 g $\mathrm{m}^{-3}$). But, the linear expression $S$ = 3.66 IWC (magenta dots) fits the data fairly well. Correlation coefficient between IWC and $S$ is 0.991. The results from Heymsfield et al. (2016), depicted by red and green lines, are in good agreement with our fits at IWC less than about 0.6 g $\mathrm{m}^{-3}$ and slightly overestimate $S$ at higher IWCs.

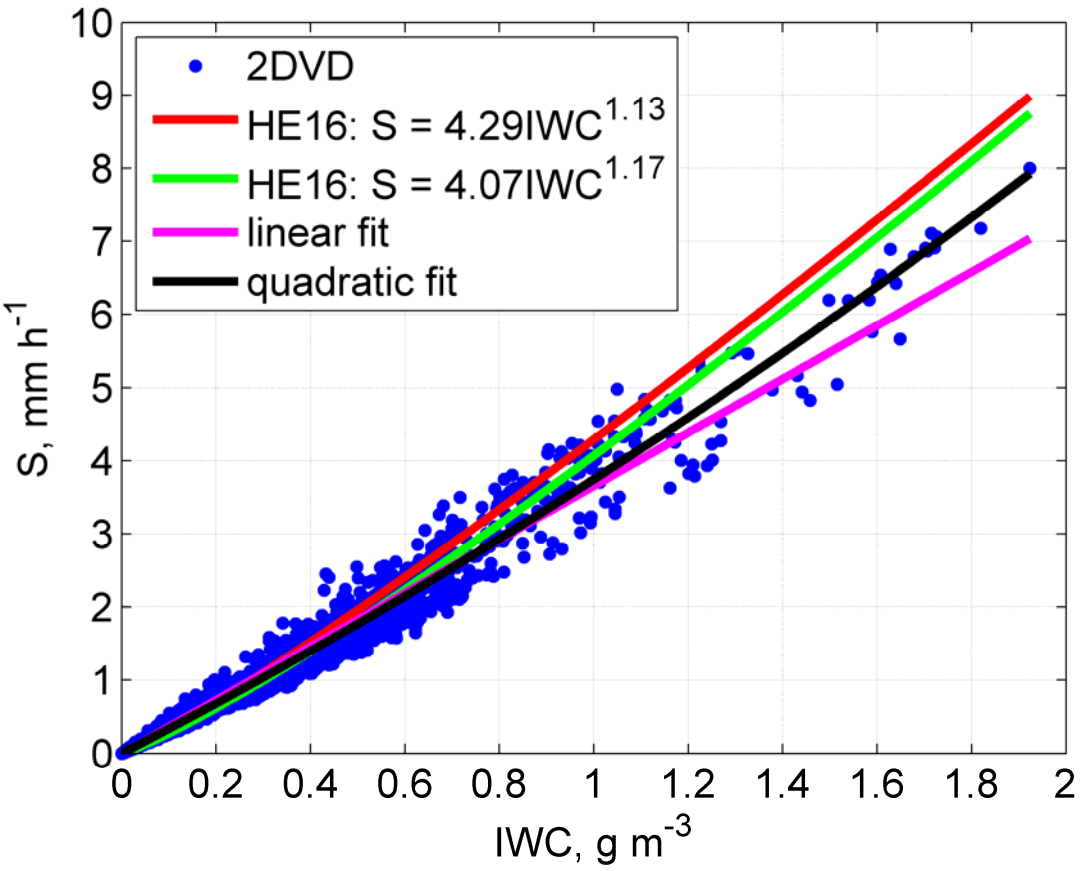



Figure 3.5: Scatterplot of IWC vs. $S$ – blue dots represent 2DVD measurements, red and green dots Heymsfield et al. (2016) relations (herein HE16), whereas magenta and black dots represent linear and quadratic least square fit on 2DVD data. Correlation coefficient between 2DVD measured IWC and $S$ is 0.991.

## 5. Disdrometer measurements-estimations and expected values of *S* and IWC

*a. Oklahoma 2DVD measurements*

The Oklahoma disdrometer dataset was used to compare the performances of the three types of algorithms: based on the combination of $Z$ and $K_{DP}$ (3.27, 3.28), using a sole $K_{DP}$ (3.23, 3.24), and traditional $Z$-based relations. The latter relations are also derived from our Oklahoma dataset to make fair and meaningful comparisons:

$$S(Z) = 0.019\, Z^{0.64}, \text{ and,} \tag{3.29}$$

$$\text{IWC}(Z) = 0.0067\, Z^{0.61}. \tag{3.30}$$

For further validation and verification, we used the data from the same 2DVD instrument located in Colorado (20 km east of Grand Junction, ~3000 m MSL) during the 2013 winter. We developed the $S$ and IWC relations for Colorado, $S_{CO}(K_{DP}, Z)$ and $IWC_{CO}(K_{DP}, Z)$, and found that these slightly differ from the Oklahoma relations. The data are derived from a sample of 6 storms (aggregated snow) which had reliable heated rain gauge measurements (SWE > 1 mm). These are also applied to the Oklahoma dataset along with three previously described methods. Although we had the data from the same type of instrument (possibly later model) located in Canada, we did not use it for cross verification of Oklahoma dataset because of the small data sample (consisting of only few storms). Instead, we used the Oklahoma relations on the Canadian data for further verification.

The scatterplots of snow rates directly estimated by the disdrometer versus expected values from the three methods computed using disdrometer data are displayed in Fig. 3.6 for the Oklahoma dataset. The width of the $S(Z)$ vs. $S$(2DVD) scatterplot (green dots in Fig. 3.6) is prohibitively large because $Z$ is $4^{th}$ moment of the particle size distribution for aggregated snow. Moreover, the $S(Z)$ tends to overestimate light and moderate snowfall whereas it underestimates high snow rates (S>5 mm $h^{-1}$). This is caused by the dependence of the multiplier in the $S(Z)$ relation on the parameters of the PSD. The $S(K_{DP})$ estimate (blue dots in Fig. 3.6) shows smaller, but still significant scatter around the one-to-one line compared to the $S(Z)$. On the other hand, the scatterplot of the $S(K_{DP}, Z)$ vs. $S$(2DVD) is very tight, concentrated along the one-to-one line, and not biased.

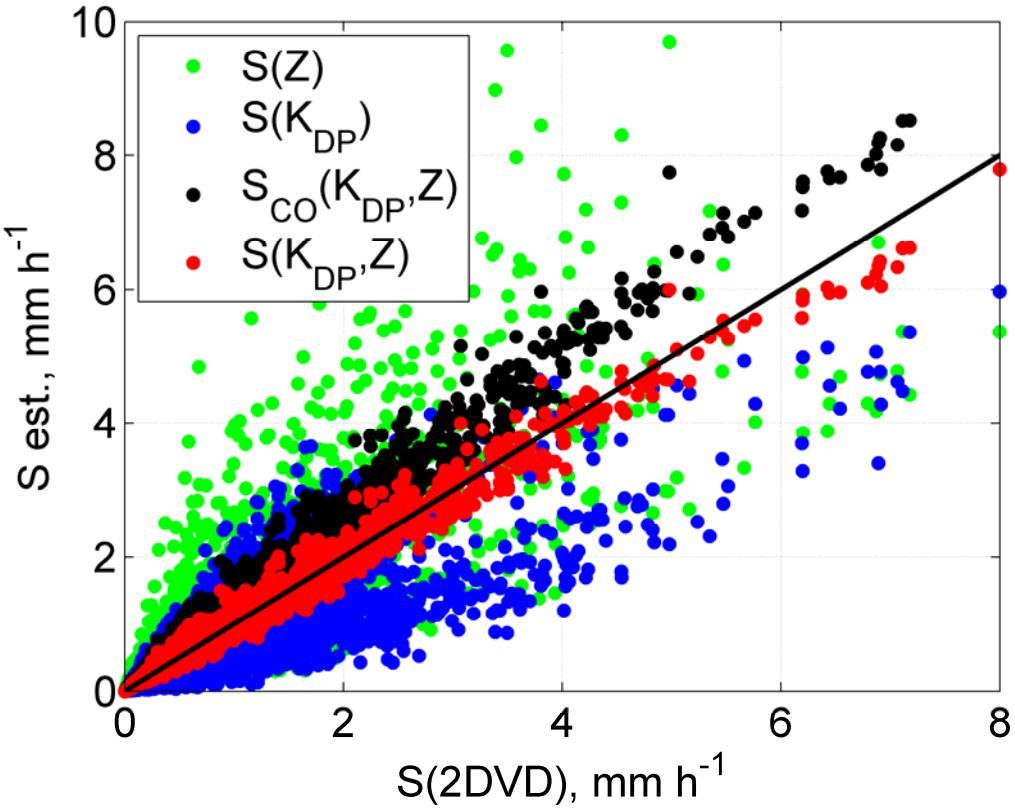



Figure 3.6: Scatterplots of $S$(2DVD) vs. $S(Z)$ (green dots), $S$(2DVD) vs. $S(K_{DP})$ (blue dots), $S$(2DVD) vs. $S_{CO}(K_{DP}, Z)$ (black dots, where subscript $_{CO}$ denotes Colorado dataset derived from 6 storms), and $S$(2DVD) vs. $S(K_{DP}, Z)$ (red dots). The correlation coefficients between $S$(2DVD) and $S(Z)$, $S(K_{DP})$, $S_{CO}(K_{DP}, Z)$, and $S(K_{DP}, Z)$ are 0.862, 0.891, 0.995, and 0.995.

For comparison and validation of our results, we derived (the same procedure as for Oklahoma) $S_{CO}(K_{DP}, Z) = 1.88\ K_{DP}^{0.61} Z^{0.34}$ relation from the Colorado data and applied it to the Oklahoma dataset. The scatter between the points (black dots) is comparable to the Oklahoma $S(K_{DP}, Z)$ scatter and has a very tight fit; the Colorado relation is positively biased, with overestimation of $S$ by about 27% (in agreement with the ratio of the relations' multipliers). The exponents of both relations are practically the same, whereas the relations' multipliers differ. This result is encouraging because the

relation derived on data from one region seems to be applicable to data from a different region.

Similar scatterplots for ice water content are displayed in Fig. 3.7. The IWC($Z$) (green dots) versus IWC(2DVD) displays relatively large scatter and underestimates IWC for larger ice water contents (IWC>1.3 g $m^{-3}$), while the IWC($K_{DP}$, $Z$) (red dots) is similar to IWC($K_{DP}$) (blue dots); the former shows very small scatter about the one-to-one line. The IWC($K_{DP}$, $Z$) agrees much better with the direct 2DVD estimates than the IWC($Z$) and has tighter fit compared to the IWC($K_{DP}$). In the same manner, as for $S$, we

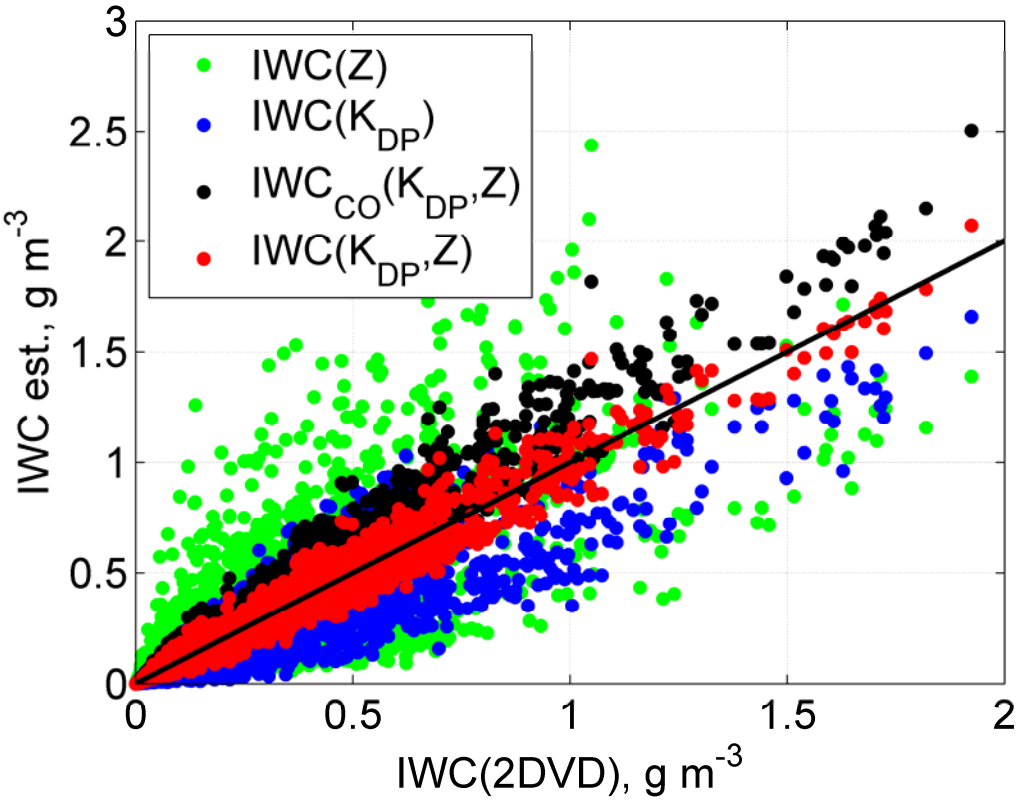



Figure 3.7: Scatterplot of IWC(2DVD) vs. IWC($Z$) (green dots), IWC(2DVD) vs. IWC($K_{DP}$) (blue dots), IWC(2DVD) vs. $IWC_{CO}$($K_{DP}$, $Z$) (black dots, where subscript $_{CO}$ denotes Colorado dataset derived from 6 storms), and IWC(2DVD) vs. IWC($K_{DP}$, $Z$) (red dots). The correlation coefficients between IWC(2DVD) and IWC($Z$), IWC($K_{DP}$), $IWC_{CO}$($K_{DP}$, $Z$), and IWC($K_{DP}$, $Z$) are 0.826, 0.932, 0.988, and 0.989.

have derived the relation for $IWC_{CO}(K_{DP}, Z) = 0.73\ K_{DP}^{0.64} Z^{0.29}$ from the 6 Colorado storms. The CO IWC relation, similarly to OK relation, exhibits the tight fit if applied to the Oklahoma data (black dots). The exponents in both OK and CO relations are practically the same, while the multiplier in the CO relation is ~4% higher. This implies that multipliers of these relations may need to be adjusted according to the geographical location or perhaps altitude (environmental conditions such as temperature, etc.).

*b. Colorado 2DVD measurements*

To further validate the polarimetric snow estimation relations, measurements obtained in Colorado during the winter of 2012-2013 are presented. For brevity, only two cases are evaluated: one with light to moderate snow accumulations, the other with high accumulations. Nonetheless, the principal findings are representative of the whole thirty events. The Colorado relations (listed in the previous section) are used for verification and comparisons with the "general" $S(K_{DP}, Z)$ relation derived from the Oklahoma data (eq. 3.27). There are several radar $S(Z)$ relations available for this area (such as Vasiloff 1997, Wolfe and Snider 2012, 2013, etc.), but we have used 2DVD derived $S_{CO}(Z) = 0.024\ Z^{0.78}$ for consistency and fair comparison. For reference, we have tested the relation of Wolfe and Snider 2012. Their relation gave comparable results with 2DVD derived $S_{CO}(Z)$, and was within ±10% to 15% of the total accumulation measured by the heated rain gauge for 2 chosen Colorado cases. For brevity, the analysis of the $S(K_{DP})$ is omitted.

1) 11 JANUARY 2013 CASE

Two major episodes of snow with different PSD types occurred during the event (Fig. 3.8). In the period from 0400 to 1200 UTC, relatively large particle sizes ($D < 8$

mm) and smaller concentration are detected (Fig. 3.8a; concentrations can be estimated from the color scale – warmer colors indicate higher concentrations). Later, from 1800 to 2200 UTC particles are smaller ($D$ < 4 mm) but have higher maximal concentration. Reflectivity factor $Z$ computed from 2DVD measurements is higher in the first period with the maximum ~34 dBZ compared to the maximum ~29 dBZ in the second (Fig. 3.8b). Large particles in conjunction with relatively lower concentrations produce the higher reflectivities during the first episode. In the later period with smaller particles, $Z$ is lower even though at times the concentrations are an order of magnitude higher than

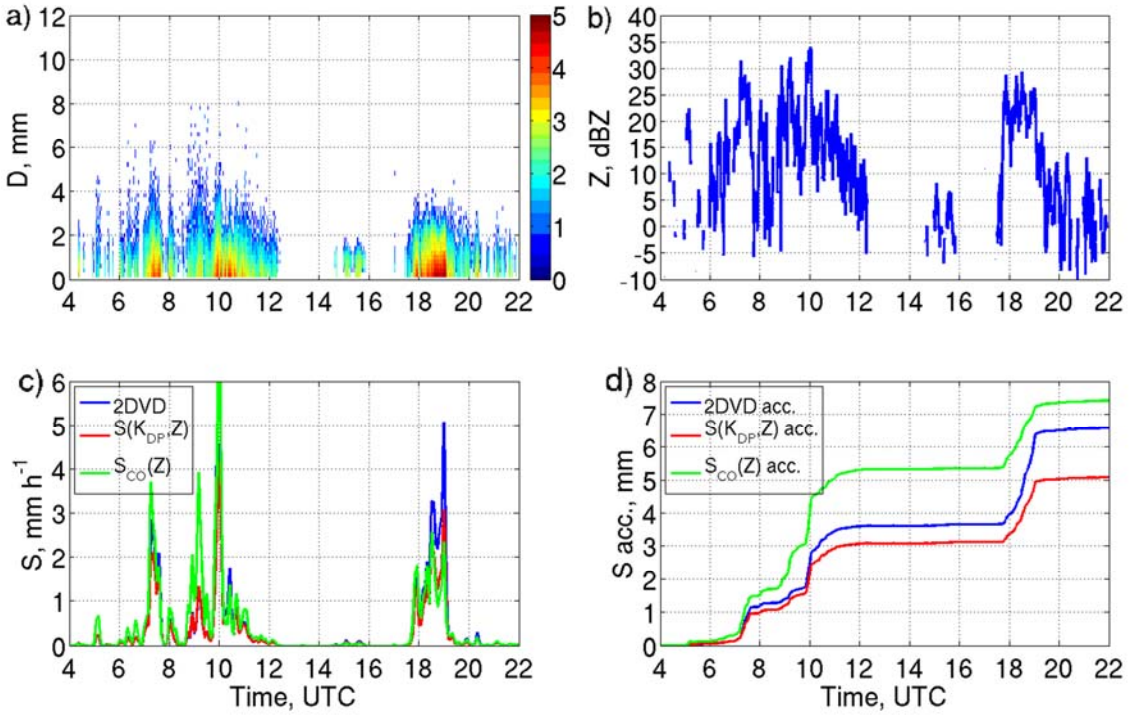



Figure 3.8: Evolution of a) PSD in $\log_{10}$ scale indicated by the color bar [$\log_{10}(m^{-3}\ mm^{-1})$], where cold to warm color scale represents low to high particle concentrations, b) $Z$, c) $S$(2DVD), $S(K_{DP}, Z)$, and $S_{CO}(Z)$ (blue, red, and green lines), and d) snow accumulations measured by 2DVD, and estimated via $S(K_{DP}, Z)$, and $S_{CO}(Z)$ (blue, red, and green curves), 11 January 2013.

in the previous period. This has a large impact on $S_{CO}(Z)$ and $S(K_{DP}, Z)$ estimates as seen in Fig. 3.8c where $S$ directly estimated by the disdrometer is also depicted.

Because $Z$ is proportional to the 4$^{th}$ PSD moment in aggregated snow, the $S_{CO}(Z)$ estimate does not capture adequately the variability of the PSD. This is why $S_{CO}(Z)$ is significantly larger than $S$(2DVD) or $S(K_{DP}, Z)$ during the period of larger snowflakes (0900 to 0930 UTC) (Fig. 3.8c). The opposite happens during the period from 1800 to 1900 UTC when smaller particles and higher concentrations are observed and $S(Z)$ has negative bias. Also note the discrepancy between the $S(K_{DP}, Z)$ and the $S$(2DVD) in the same period. This is caused by non-aggregate nature of precipitation, indicated by larger values of $Z_{DR}$ (not shown), for which the polarimetric relations are not tuned. Overall, the $S(K_{DP}, Z)$ estimate accounts better for the variations in PSDs and microphysics; hence, it is closer to the disdrometer estimated $S$ (except for non-aggregate precipitation period). A heated rain gauge collocated with the disdrometer registered a total snow water equivalent of 6.6 mm; the 2DVD particle filtering threshold was chosen such that the 2DVD accumulation matched this value. The snow accumulation from $S(K_{DP}, Z)$ is about ~23% lower compared to the "true" accumulation estimated by the disdrometer, whereas the $S_{CO}(Z)$ accumulation is ~15% higher (Fig. 3.8d). This result is mostly caused by the precipitation in the period from 1800 to 1900 UTC, where both $S_{CO}(Z)$ and $S(K_{DP}, Z)$ underestimate the snow amounts which falsely improves $S_{CO}(Z)$ performance. Before this period of non-aggregates, $S(K_{DP}, Z)$ was much closer to the 2DVD estimate than $S_{CO}(Z)$.

The scatterplots of $S(Z)$ vs. $S$(2DVD) (green dots), $S(K_{DP}, Z)$ vs. $S$(2DVD) (red dots) and $S_{CO}(K_{DP}, Z)$ vs. $S$(2DVD) (blue dots) are in Fig. 3.9. The $S_{CO}(Z)$ exhibits large

spread mainly because $Z$ is proportional to the 4$^{th}$ moment of the PSD in aggregated snow. In contrast, the $S(K_{DP}, Z)$ produces relatively small scatter that is closer to the one-to-one line and the $S_{CO}(K_{DP}, Z)$ expected value obtained from 6 Colorado storms. The correlation coefficient between the 2DVD estimated $S$ and the $S_{CO}(Z)$ expected value is 0.833, whereas the corresponding correlation coefficients for the $S(K_{DP}, Z)$ and $S_{CO}(K_{DP}, Z)$ expected values are both 0.983.

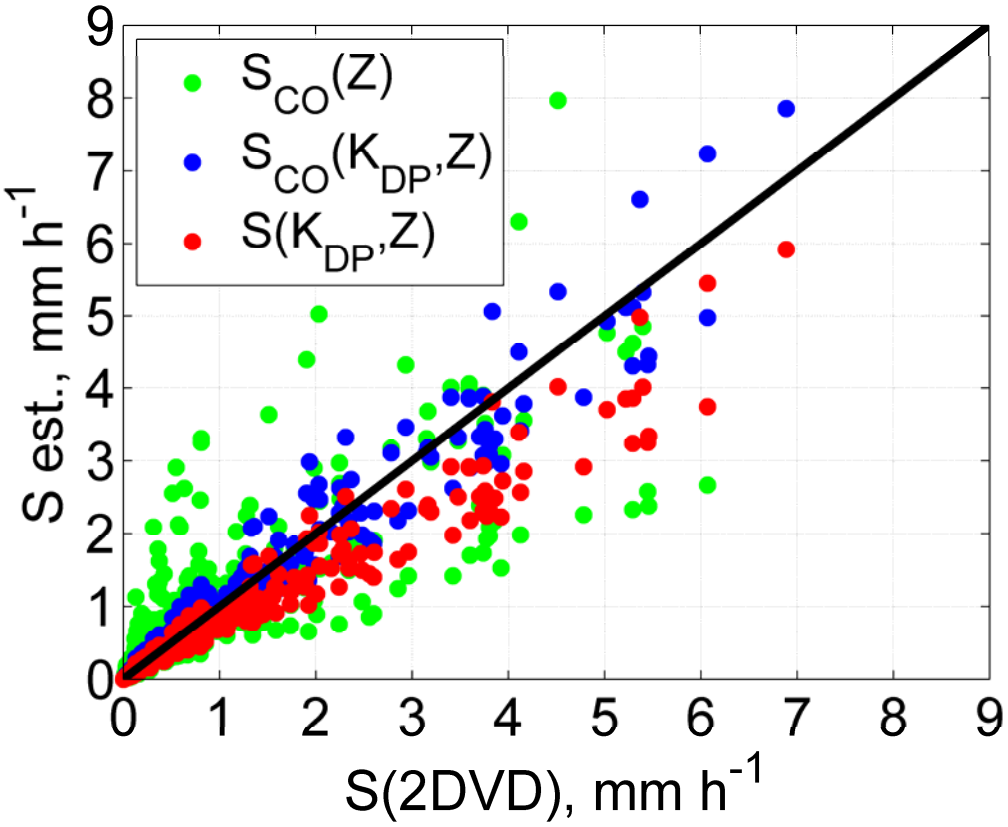



Figure 3.9: Scatterplots of $S$(2DVD) vs. $S_{CO}(Z)$ (green dots), $S$(2DVD) vs. $S_{CO}(K_{DP}, Z)$ (blue dots), and $S$(2DVD) vs. $S(K_{DP}, Z)$ (red dots), 11 January 2013. Correlation coefficients between $S$(2DVD) and $S_{CO}(Z)$, $S_{CO}(K_{DP}, Z)$, $S(K_{DP}, Z)$ are 0.833, 0.983, and 0.983.

2) 28 JANUARY 2013 CASE

In this event, the snowfall accumulation measured with the co-located heated rain gauge was 22.9 mm. The PSDs had highly variable sizes (maximal diameters ~12 mm) and concentrations (Fig. 3.10a). The highest reflectivity factor of ~36 dBZ was measured at ~1445 UTC (Fig. 3.10b) and attributed to a relatively high number of large particles compared to the number of small particles.

Snowfall rates $S(K_{DP}, Z)$, (red line in Fig. 3.10c) are slightly underestimated but remain closer to the 2DVD estimations (blue line, Fig. 10c) than are $S_{CO}(Z)$ rates (green line, Fig. 3.10c). As in the previous case, $S_{CO}(Z)$ is heavily weighted by the particles' sizes, producing higher values than $S$(2DVD) and $S(K_{DP}, Z)$ at 0600 UTC and from 1300 until 1900 UTC.

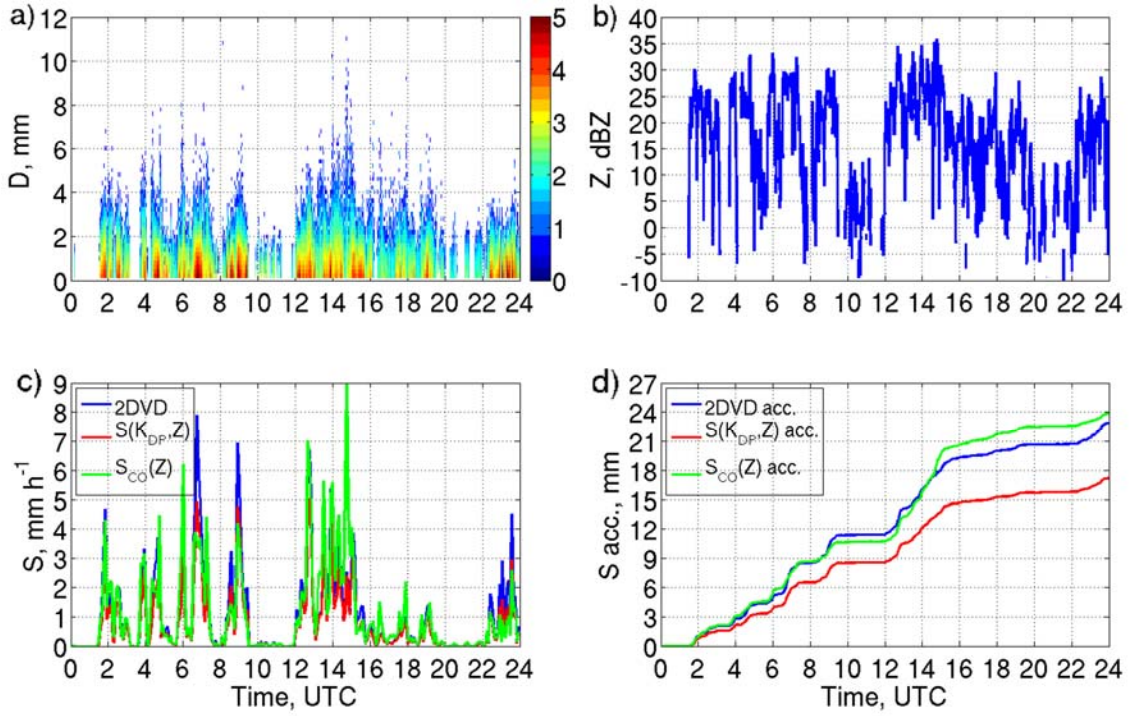



Figure 3.10: As in Figure 8, but for 28 January 2013.

Whenever the concentrations are high (~0700 and 0900 UTC), even with moderate $Z$, $S_{CO}(Z)$ significantly underestimates snow rate, as in the previous examples. The difference between the accumulations from $S(K_{DP}, Z)$ and $S$(2DVD) is ~25%, but the shapes of the curves are very similar (red and blue lines, Fig. 3.10d), whereas the estimate from $S_{CO}(Z)$ (green line, Fig. 3.10d) is not as consistent with the measurements although it underestimates the total amount by only ~7%. Despite such a small difference in a snow totals, the instantaneous LWE from disdrometer measurements and $S_{CO}$(Z) show large discrepancies. Thus, in this case, the good agreement in accumulations is fortuitous.

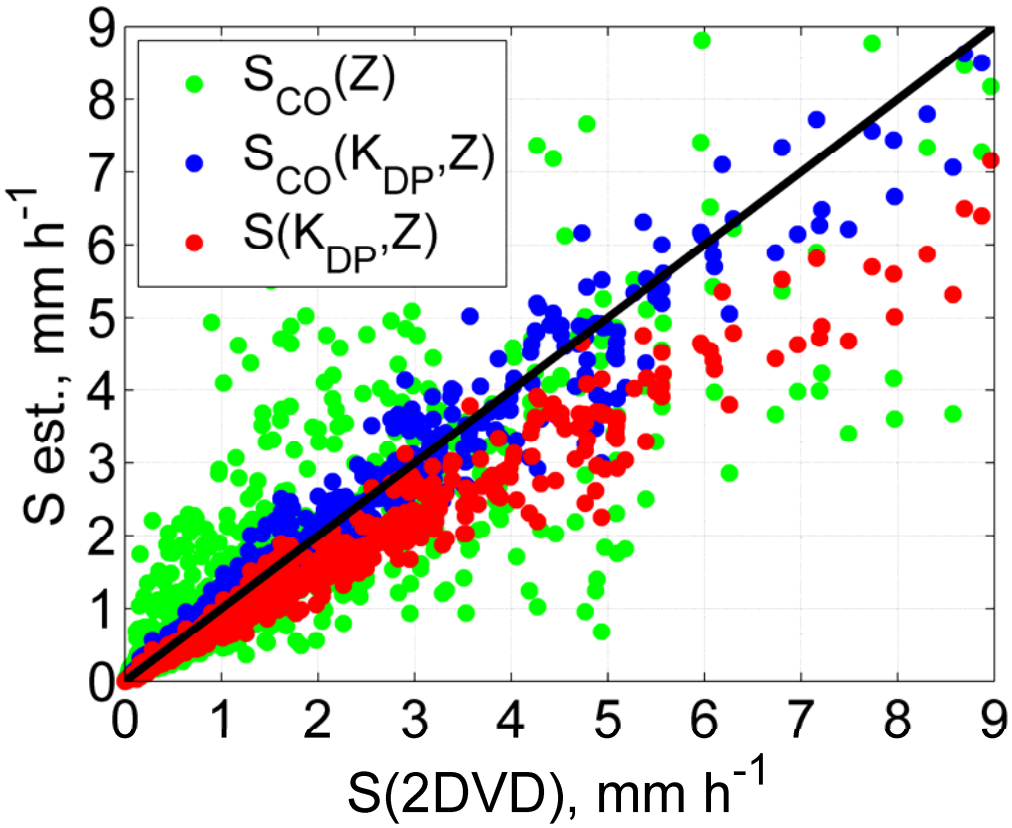



Figure 3.11: Scatterplots of $S$(2DVD) vs. $S_{CO}(Z)$ (green dots), $S$(2DVD) vs. $S_{CO}(K_{DP}, Z)$ (blue dots), and $S$(2DVD) vs. $S(K_{DP}, Z)$ (red dots), 28 January 2013. Correlation coefficients between $S$(2DVD) and $S_{CO}(Z)$, $S_{CO}(K_{DP}, Z)$, $S(K_{DP}, Z)$ are 0.796, 0.987, and 0.987.

The scatterplots of $S$(2DVD) vs. $S_{CO}(Z)$, $S$(2DVD) vs. $S(K_{DP}, Z)$, and $S$(2DVD) vs. $S_{CO}(K_{DP}, Z)$ are in Figure 3.11. Again, $S_{CO}(Z)$ exhibits a very large dispersion around the one-one line (green dots), which is in accord with the previous event analysis. $S(K_{DP}, Z)$ is biased slightly-to-moderately and displays small dispersion (red dots). The scatterplot is relatively close to the $45^{o}$ line and the $S_{CO}(K_{DP}, Z)$ results derived from Colorado dataset (blue dots). Although the $S(K_{DP}, Z)$ underestimates the total SWE amount, the correlation with $S$(2DVD) is high (0.987) compared to the one for $S_{CO}(Z)$ which is significantly lower (0.796). This means that the bias in the $S(K_{DP}, Z)$ estimate could be removed by simply adjusting the multiplier of the relation according to the regional climatology (or altitude). This is consistent with the previous case analysis, thus $S(K_{DP}, Z)$ could potentially produce more realistic results than the $S_{CO}(Z)$ relation which was specially derived for this region.

*c. Canada 2DVD measurements*

The data presented in this section were obtained during the Global Precipitation Measurement Cold Season Precipitation Experiment (GCPEX) (Skofronick-Jackson et al. 2015) in Ontario, Canada and thus enable verification of the polarimetric relation in a different climate region. In particular, the 25 February 2012 case is classified as lake effect snow event. The total SWE amount (measured by OTT pluvio weighing precipitation gauge, description available at http://www.ott.com/en-us/products/meteorological-sensors-26/ott-pluvio2-weighing-rain-gauge-963/) was ~7.6 mm. Here, the "event specific" polarimetric relation (denoted as $S_{et}(K_{DP}, Z)$, thus subscript "et") is derived for this particular event and used for comparison. Hence, "general" $S(K_{DP}, Z)$ and $S_{et}(K_{DP}, Z)$ have different multipliers in their bivariate power-

law relations because $S(K_{DP}, Z)$ is derived from the Oklahoma dataset (16 storms), whereas $S_{et}(K_{DP}, Z)$ is obtained from this Canada (Ontario) storm. Also $S_{et}(Z)$ is derived, which along with $S_{et}(K_{DP}, Z)$ provides independent comparison/verification.

The PSDs evolution indicates that the maximum sizes of snowflakes are about 10 mm and the highest concentrations (as indicated by color bar) are recorded between 0900 and 1200 UTC (Figure 3.12a). This event contained multiple snow cells and displayed large variability in PSDs. The highest reflectivities (~30-32 dBZ, Fig. 3.12b) occurred in periods when the largest particles were present. It is evident (Fig. 3.12c) that the $S_{et}(Z)$ overestimates $S$ when larger particles with lower concentrations are present (from 0300 to 0400 UTC, and 1400 to 1800 UTC) and underestimates snow rate

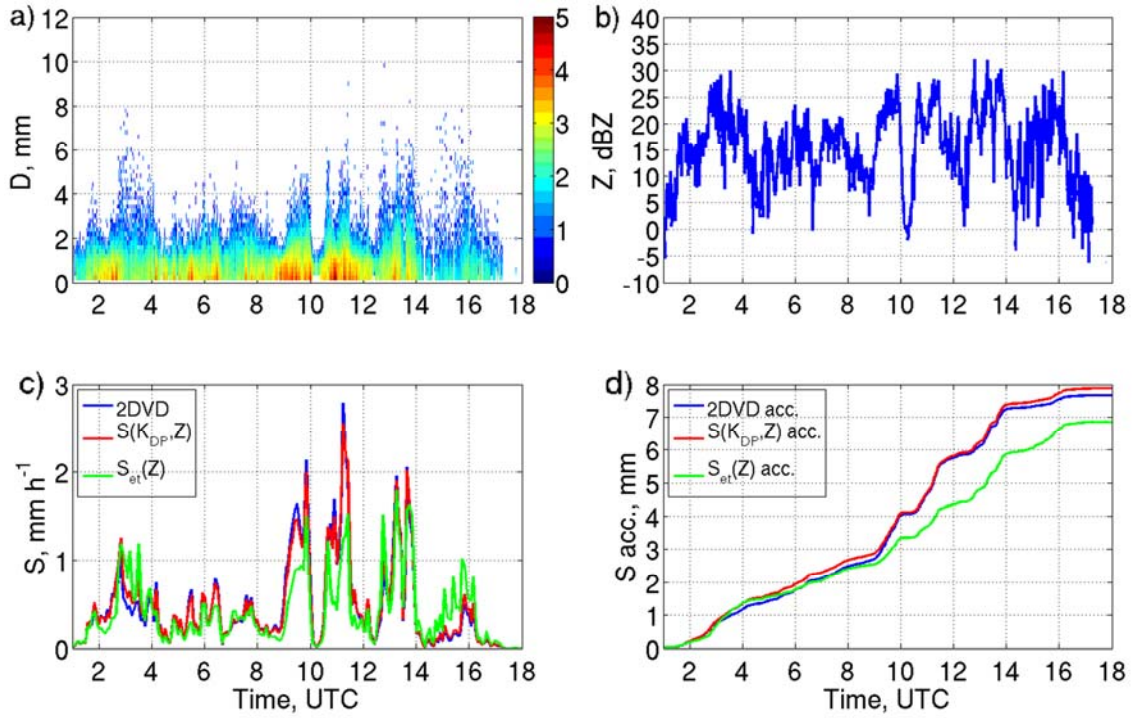



Figure 3.12: Evolution of a) PSD in $\log_{10}$ scale indicated by the color bar [$\log_{10}(m^{-3} mm^{-1})$], where cold to warm color scale represents low to high particle concentrations, b) $Z$, c) $S$(2DVD), $S(K_{DP}, Z)$, and $S_{et}(Z)$ (blue, red, and green lines), and d) snow accumulations measured by 2DVD, and estimated via $S(K_{DP}, Z)$, and $S_{et}(Z)$ (blue, red, and green curves), 25 February 2012.

vice versa (green line), whereas $S(K_{DP}, Z)$ matches almost perfectly the 2DVD measurements. Even though the largest particle sizes are moderate during the periods of high concentrations, $S_{et}(Z)$ underestimates $S$ at these times (from 1010 to 1400 UTC). The $S(K_{DP}, Z)$ closely follows the 2DVD measurements. Accumulations from $S_{et}(Z)$ are underestimated by ~11% (Fig. 3.12d, green line), whereas those from $S(K_{DP}, Z)$ are just ~3% higher (red line) than the reference measurement (blue line).

The scatterplots of $S$(2DVD) vs. $S_{et}(Z)$, $S(K_{DP}, Z)$, and $S_{et}(K_{DP}, Z)$ are in Fig. 3.13. The $S_{et}(Z)$'s (green dots) large dispersion is evident in the scatterplot (correlation coefficient = 0.825). This is in contrast to the $S(K_{DP}, Z)$ vs. $S$(2DVD) scatter diagram

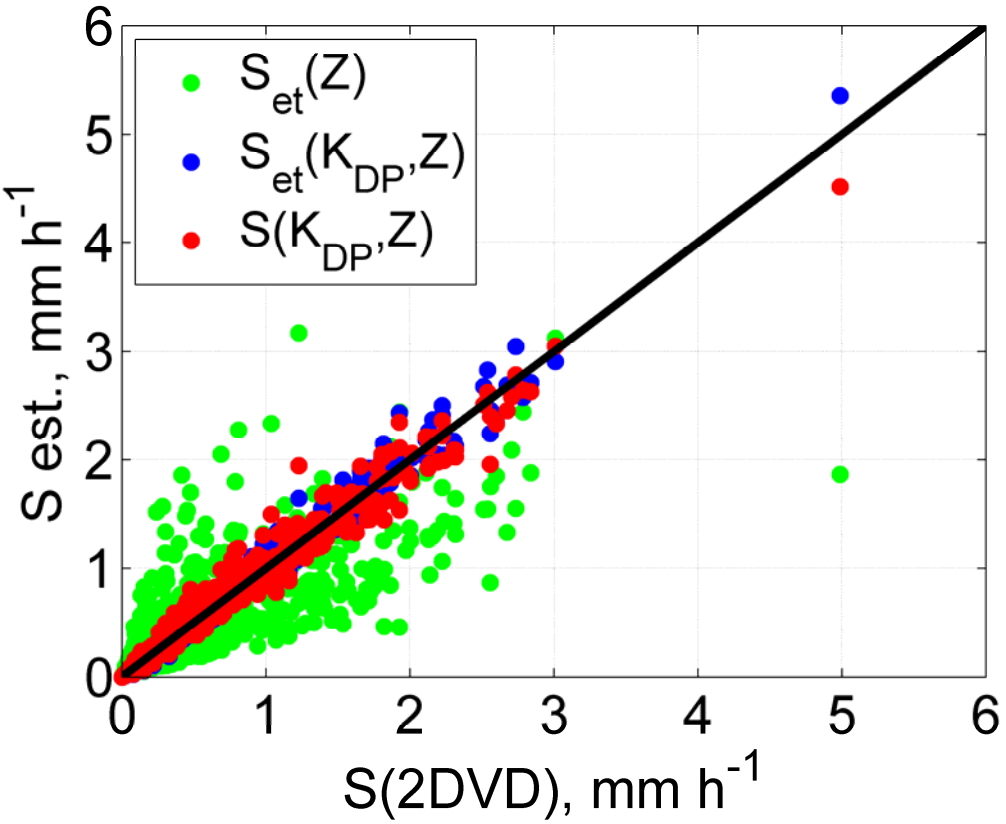



Figure 3.13: Scatterplots of $S$(2DVD) vs. $S_{et}(Z)$ (green dots), $S$(2DVD) vs. $S_{et}(K_{DP}, Z)$ (blue dots), and $S$(2DVD) vs. $S(K_{DP}, Z)$ (red dots), 25 February 2012. Correlation coefficients between $S$(2DVD) and $S_{et}(Z)$, $S_{et}(K_{DP}, Z)$, $S(K_{DP}, Z)$ are 0.825, 0.993, and 0.988.

(correlation coefficient = 0.988) which has a very small dispersion about the 45$^{o}$ line. Furthermore, it is very close to the event specific $S_{et}(K_{DP}, Z)$.

## 6. Discussion

The results of this study demonstrate that the $S(K_{DP}, Z)$ and IWC($K_{DP}$, $Z$) relations for snow measurements dramatically reduce the adverse impact of the snow particle size distribution variability on the snow liquid water equivalent and ice water content estimates compared to traditional $Z$-based relations. The fact that the polarimetric relations derived from the Oklahoma disdrometer dataset perform quite well (with little or no tuning) in different climate regions (Colorado and Ontario) also points to their universal nature. However, these relations have been derived with certain assumptions about snowflake shapes and orientations which may strongly affect the value of specific differential phase $K_{DP}$. In other words, the multipliers $\gamma_1$ and $\gamma_2$ in the $S(K_{DP}, Z)$ and IWC($K_{DP}$, $Z$) relations can be quite different for different assumptions about shapes and orientations.

Eq. (A26) for $K_{DP}$ in Appendix shows that $K_{DP}$ is directly proportional to the difference between shape factors $L_b - L_a$, which depends on the aspect ratio of snowflakes (Fig. 3.14). The computations of $K_{DP}$ in this Chapter were performed for the aspect ratio equal to 0.65. Korolev and Isaac (2003) found that the aspect ratio of irregular or aggregated ice particles varies between 0.5 and 0.7 and does not depend on the particle size within the range between 100 and 1000 microns. Fig. 3.14 shows that if the aspect ratio changes within the interval +/- 0.1 about its *mean*, then the change in $L_b$

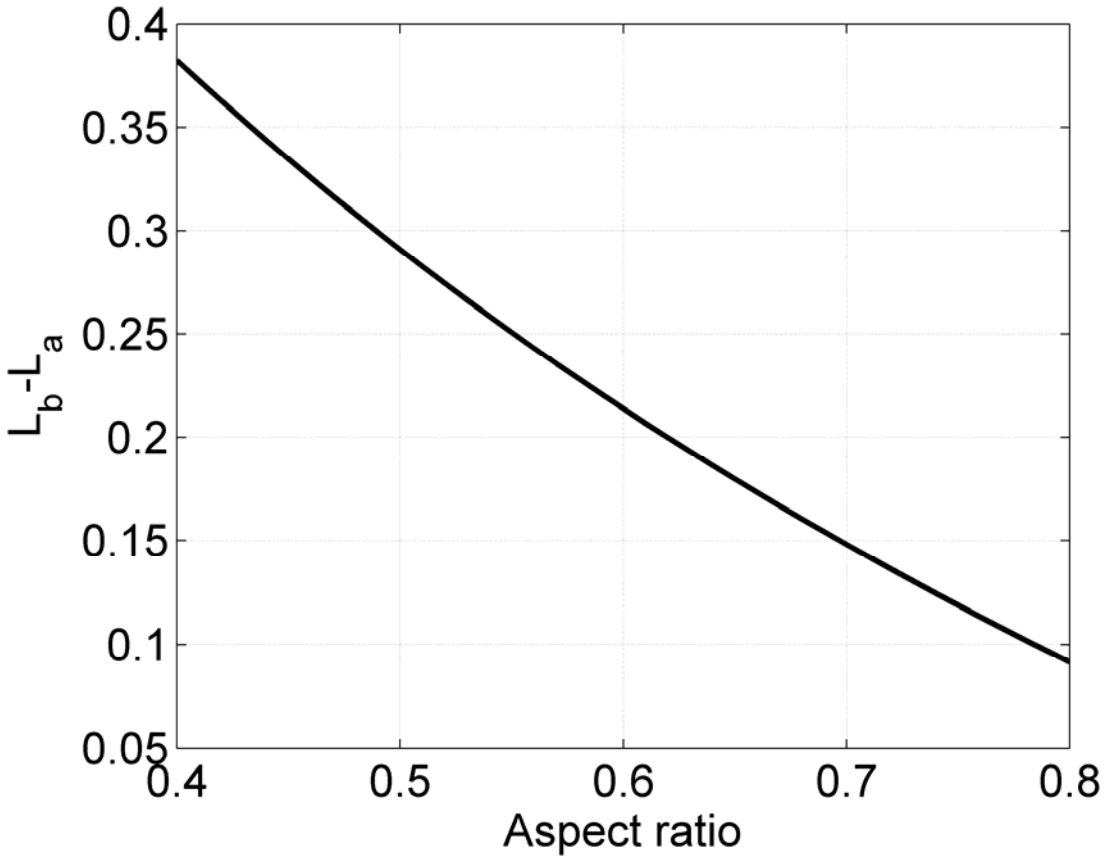



Figure 3.14: Dependence of $L_b - L_a$ on the aspect ratio of oblate spheroids.

$- L_a$ is about 30%. This causes errors of about 18 – 19% in the estimates of $S$ and IWC because $K_{DP}$ enters with the exponents close to 0.6 into the relations for $S$ and IWC.

It is assumed in computations that the snowflakes are equioriented (as justified in Hogan et al. 2012), i.e., the width $\sigma$ of the canting angle distribution is equal to zero. In fact, $K_{DP}$ is quite sensitive to $\sigma$ and the dependence of $K_{DP}$ on $\sigma$ is quantified by the factor $r = \exp(-2\sigma^2)$ in (A26). This means that the coefficients $\gamma_1$ and $\gamma_2$ are approximately proportional to the factor $\exp(-1.2\sigma^2)$. The width of the distribution of snowflake orientations is determined by size (or Reynolds number) and atmospheric turbulence. Matrosov et al. (2005) and Melnikov and Straka (2013) found that the parameter $\sigma$ is close to 10° within a dendritic growth layer (DGL) between air

temperatures of -20°C and -10°C. At higher temperatures below DGL, where intense aggregation usually starts, $\sigma$ may increase and reach values of 40° (Hendry et al. 1987). The corresponding values of $\exp(-1.2\sigma^2)$ are equal to 0.96 and 0.55 for $\sigma$ = 10° and 40°. This means that $\gamma_1$ and $\gamma_2$ should be increased ~1.8 times to account for the more random orientations of snowflakes at $\sigma$ = 40°.

Although the degree of snow riming was accounted for in computations via (3.7), the Oklahoma dataset includes snow events with very light riming. The $\gamma_1$ and $\gamma_2$ are also sensitive to the degree of riming $f_{\text{rim}}$. It follows from Eqs. (A10, A11, A16, and A26) that $S \sim f_{\text{rim}}^{4/3}$, IWC $\sim f_{\text{rim}}$, and $Z$, $K_{\text{DP}} \sim f_{\text{rim}}^2$ for low-density snow. Therefore, the coefficient $\gamma_1$ in the $S(K_{\text{DP}}, Z)$ relation is proportional to $f_{\text{rim}}^{-0.55}$ and $\gamma_2$ in the IWC($K_{\text{DP}}$, $Z$) relation is proportional to $f_{\text{rim}}^{-0.86}$. Hence, both coefficients are lower for rimed snow. At the moment, we do not know a typical variability range of the parameter $f_{\text{rim}}$ in snow. In similar manner, the decrease in particles' density by 20% causes the increase of ~16% in polarimetric relations multipliers for $S$ and IWC, whereas, in the case of the 20% particles' density increase, the multipliers of the polarimetric relations for $S$ and IWC decrease by ~11%. The exponents of $K_{\text{DP}}$ and $Z$ in $S(K_{\text{DP}}, Z)$ and IWC($K_{\text{DP}}$, $Z$) are almost insensitive to the change in particles' density.

The uncertainties in relations' multipliers regarding the changes in $K_{\text{DP}}$ and $Z$ (proxy for forward model error) are explored next. Due to simplicity, only the individual and simultaneous increase/decrease by 20% in $K_{\text{DP}}$ and $Z$ are presented. In the case of $K_{\text{DP}}$ increase (decrease) by 20%, $\gamma_1$ and $\gamma_2$ decrease (increase) by ~11% (~15.5%). This change in relations' multipliers is almost identical as the one caused by the particles' density. There is a linear relation between the $K_{\text{DP}}$ and $\rho_s$ in low density

snow, where the $K_{DP}$ is the first moment of the snow particle size distribution. Similarly, the increase (decrease) of $Z$ by 20%, causes $\gamma_1$ and $\gamma_2$ to decrease (increase) by ~5.5% (~7%). If the $K_{DP}$ and $Z$ increase (decrease) simultaneously by 20%, $\gamma_1$ and $\gamma_2$ decrease (increase) by ~15.8% (~23.5%).

The influence of the observational uncertainty on the polarimetric relations' multipliers is reflected through the observational error of the equivolume diameter $D$. In 2DVD snow particles measurements, the observational error in equivolume diameter $D$ ranges from 0.05 mm to 0.1 mm. If $D$ is measured with accuracy of ± 0.05 mm, $\gamma_1$ decreases (increases) by 3% (2%) whereas $\gamma_2$ is smaller/greater by ~5%. Similarly, for $D$ ± 0.1 mm, $\gamma_1$ changes by about ± 5%, and $\gamma_2$ increases (decreases) by 12% (9%).

Sensitivity of the polarimetric relations for estimation of $S$ and IWC to snowflake shapes, orientations, and degree of riming (density change) is a primary source of uncertainty in the $S$ and IWC estimation. The secondary source of indeterminacy is reflected in model related errors of $K_{DP}$ and $Z$ estimation (which for $K_{DP}$ are almost the same as for the density change, whereas $Z$ is less affected), and (somewhat smaller) observational errors of snow particle sizes. The primary uncertainty could be evaluated using radar observations and snow gauge measurements at the surface or aircraft probes in situ. Thus the suggested polarimetric relations could be "calibrated" experimentally using radar data; this is a subject of ongoing study.

## 7. Summary

Basic principles for polarimetric measurements of snow rate and ice water content are outlined in this study. A combined use of $Z$ and $K_{DP}$ for quantitative

estimation of liquid equivalent snowfall rate $S$ and ice water content IWC is suggested. Analysis of 2D video disdrometer data from dry snow indicates that the combination of $Z$ and $K_{DP}$ dramatically reduces the uncertainty in the estimates of $S$ and IWC caused by the variability of snow size distribution compared to the traditional $Z$-based estimators.

To derive the $S(K_{DP}, Z)$ and IWC($K_{DP}$, $Z$) relations from 2D video disdrometer, a problem of particle mismatching is addressed by filtering out the obviously mismatched particles with discriminating thresholds. These thresholds are determined from the (heated) rain gauges or pluvio total event accumulations. To better represent the impact of snow riming the so-called "adjusted" snow density (obtained from 2DVD terminal velocity measurements) is used in computations of polarimetric variables and microphysical parameters.

The theoretical relations for parameterization of $S(Z)$ and IWC($Z$) by the intercept $N_{0s}$ of the exponential size distribution are verified with the disdrometer measurements. These served as a starting point for the derivation of the $S(K_{DP}, Z)$ and IWC($K_{DP}$, $Z$) relations.

It is shown that snow rate $S$ and ice water content IWC can be obtained from the bivariate power-law relations $S = \gamma_1 K_{DP}{}^{\alpha_1} Z^{\beta_1}$ (Eq. 3.27) and $\mathrm{IWC} = \gamma_2 K_{DP}{}^{\alpha_2} Z^{\beta_2}$ (Eq. 3.28) where the multipliers $\gamma_1$ and $\gamma_2$ depend on the particle shapes, orientations, and degree of riming (snow density). These multipliers can be determined experimentally by comparing radar data with in situ measurements of $S$ and IWC. Multipliers $\gamma_1$ and $\gamma_2$ also depend on the accuracy of the forward model for $K_{DP}$ and $Z$ estimation, and observational error of snow particle sizes. These are secondary sources of uncertainties, smaller than the dependencies on the particle shapes, orientations, and snow density.

In addition to the polarimetric relations for $S$ and IWC, similar relations for the intercept $N_{0s}$ and slope parameter $\Lambda_s$ of the exponential size distribution, $N_{0s}(K_{DP}, Z)$ and $\Lambda_s(K_{DP}, Z)$ are developed. These can be used for direct microphysical retrieval from the polarimetric radar measurements.

Initial $S(K_{DP}, Z)$ and IWC$(K_{DP}, Z)$ relations were obtained from the disdrometer analysis of 16 snow events in Oklahoma. Besides an excellent performance locally (Oklahoma), these relations perform reasonably well for snowstorms in Colorado and very well in Canada, two distinct climate regions, which attests to a potentially universal character of such relations.

The correlation coefficient between the measured and estimated $S(K_{DP}, Z)$ (or IWC$(K_{DP}, Z)$) is much higher (~0.99) than for $S(Z)$ (or IWC$(Z)$) estimate (~0.8 to ~0.89), which increases confidence in the utility of the novel polarimetric relations. Sensitivity tests indicate the exponents of $K_{DP}$ and $Z$ are practically constant, with almost no dependence on the variability in snow density, aspect ratio, and width of the angular distribution. This simplifies the adjustment of these relations. To improve performance of $S(K_{DP}, Z)$ or IWC$(K_{DP}, Z)$ in distinct climate regions such as Colorado, only the multiplier in $S(K_{DP}, Z)$ or IWC$(K_{DP}, Z)$ needs to be adjusted according to the local environmental conditions (temperature, humidity, etc.). This is verified by applying relations $S_{CO}(K_{DP}, Z)$ and IWC$_{CO}(K_{DP}, Z)$ derived from Colorado dataset to the Oklahoma dataset; Colorado polarimetric relations' multipliers are ~27% and 4% higher than their Oklahoma counterparts. Thus, it appears that the derived relations may have fairly wide applicability. This nonetheless needs to be further investigated.

# Chapter 4: Verification of Polarimetric Relations for Snow Quantification with Polarimetric Radar Measurements

## 1. Introduction

The theoretical background, derivation, and verification of polarimetric relations for snow quantification using 2DVD measurements and computations are presented and discussed in Chapter 3 (accepted in JAMC). Because disdrometer is only a point source of information, application extension to polarimetric radar measurements should be made to test operational utility. Thus herein, the applicability of polarimetric relations for snow estimation from polarimetric radar measurements is investigated. The Chapter is structured as follows. The methodology of radar measurements is presented in section 2, whereas the sensitivities of $S(K_{DP}, Z)$ and $IWC(K_{DP}, Z)$ polarimetric relations exponents $\alpha_1$, $\alpha_2$, $\beta_1$, and $\beta_2$, and multipliers, $\gamma_1$ and $\gamma_2$, are discussed in section 3. Section 4 contains description of three snow cases used for verification of polarimetric snow relations, followed by discussion and summary in sections 5 and 6.

## 2. Methodology

Polarimetric radar measurements contain a plethora of information regarding the precipitating environment. But not all measurements are equally useful. For example, specific differential phase, $K_{DP}$, is a range derivative of differential phase $\Phi_{DP}$ and can be very noisy, especially in snow. Also, the values of $K_{DP}$ are close to zero for the irregular or aggregated snow. Fortunately, the emergence of new radar data displaying/processing techniques, such as Enhanced (or more appropriate "Columnar") Vertical Profiles (EVPs, Bukovčič et al. 2017a) or Quasi Vertical Profiles (QVPs,

Ryzhkov et al. 2016, Griffin et al. 2017), can help in reduction of $K_{DP}$ measurement/estimation errors. The QVP product is radar centric and requires 360° azimuthal averaging. It is constructed as follows. For each radial increment (range gate) within the volume scan higher tilt (usually between 10° and 20°), 360° azimuthal averaged value is projected to the radar centered vertical axis. This gives a QVP of one-time interval. Repeating this procedure for all available radar temporal scans, time vs. height format of QVP's is obtained.

Specifically, the QVP of $K_{DP}$ is obtained as follows. Estimates of $\Phi_{DP}$ radial profiles are smoothed and least square fits of a slope at consecutive range locations provides the $K_{DP}$ slant radial profiles; the QVP of $K_{DP}$ is then constructed by azimuthally averaging these profiles to further reduce the statistical errors. Thus, QVP significantly reduces the noise and improves the accuracy of $K_{DP}$, decreasing the measurement error to about 0.01 deg km$^{-1}$. This is more than sufficient for $K_{DP}$ to be used in snow estimation but only in vicinity of the radar. The QVP's, presented in time vs. height format, are the essential data for verification of polarimetric snow relations in this study. For detailed description about the QVPs the reader is referred to Ryzhkov et al. (2016).

Another dependency that needs to be accounted for while using the QVP for snow estimation is the variation of particle's aspect ratio as function of the radar elevation angle (Fig 4.1). For example, if the aspect ratio equals 0.6 at 0° radar elevation angle, its apparent value at 20° elevation would be ~0.645, as depicted in Fig. 4.1. The relation for the dependence of aspect ratio on radar elevation is:

$$(b/a)_\theta = (b/a)_0 \sin^2(90^\circ - \theta) + \cos^2(90^\circ - \theta) = (b/a)_0 \cos^2\theta + \sin^2\theta, \qquad (4.1)$$

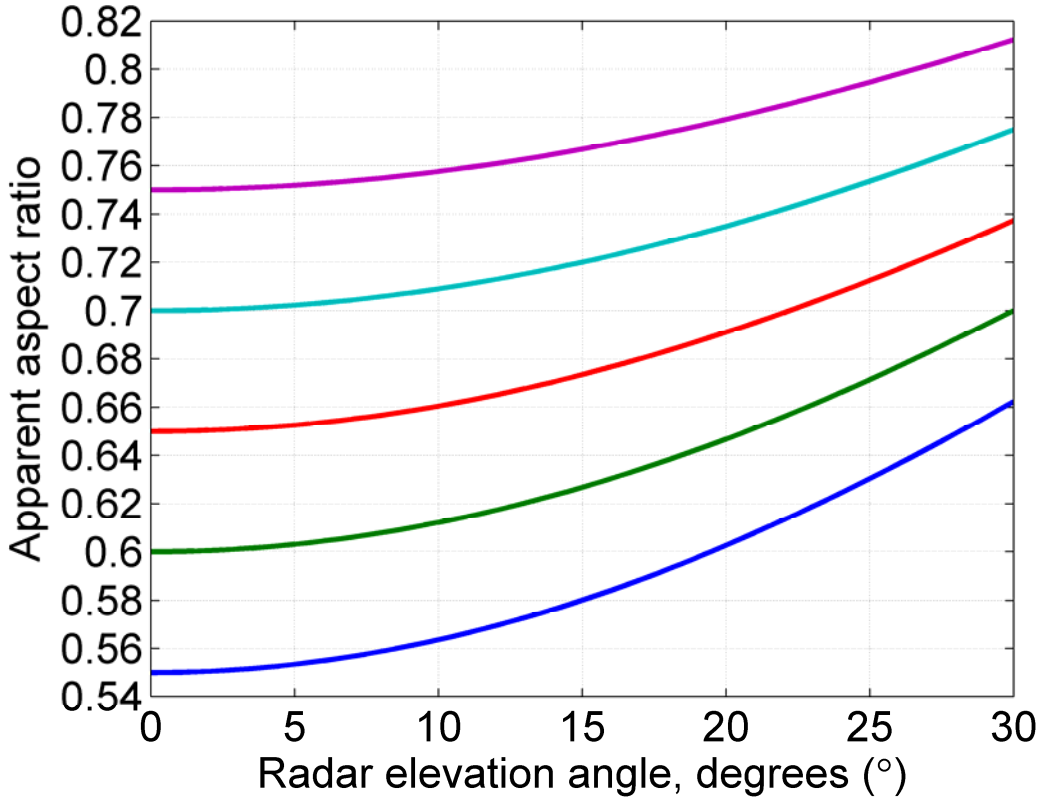



Figure 4.1: Dependence of the particle's aspect ratio on radar elevation angle (for σ = 0° and <canting angle> = 0°, where symbol < > represent mean). Blue, green, red, cyan, and magenta lines represent the change in the apparent aspect ratio $(b/a)_\theta$ = 0.55, 0.6, 0.65, 0.7, and 0.75 for different radar elevation angles, from 0° to 30°.

where $b/a$ is particle's aspect ratio and $\theta$ is radar elevation angle in degrees (subscripts $_\theta$ and $_0$ represent elevation angles $\theta$ and 0° respectively, where $(b/a)_\theta$ is the apparent aspect ratio). This means that the multipliers in $S(K_{DP}, Z)$ and IWC($K_{DP}$, $Z$) relations need to be adjusted for the radar elevation angle according to the Eq. (4.1) because they have been derived for 0° elevation angle.

### 3. Sensitivity of $S(K_{DP}, Z)$ and IWC($K_{DP}$, $Z$) relations on particle's aspect ratio $b/a$ and the width of the canting angle distribution $\sigma$

It is shown in Chapter 3 how the multipliers $\gamma_1$ and $\gamma_2$, and exponents $\alpha_1$, $\alpha_2$, $\beta_1$, and $\beta_2$, of $S(K_{DP}, Z)$ and IWC($K_{DP}$, $Z$) relations depend on particle's density, aspect

ratio, and the width of the canting angle distribution individually. The biggest uncertainty comes from $\sigma$ and $b/a$, whereas the change in the degree of riming (change in snow density) is partially accounted for by the (density) adjustment through the ratio of squares of measured and prescribed empirical velocities (eq. 3.7). Hence, the dependences of $\alpha_1$, $\alpha_2$, $\beta_1$, $\beta_2$, $\gamma_1$, and $\gamma_2$, on the joint influence of $\sigma$ and $b/a$ from 2DVD measurements and computations are presented in Figs. 4.2, 4.3 and 4.4. The rugged

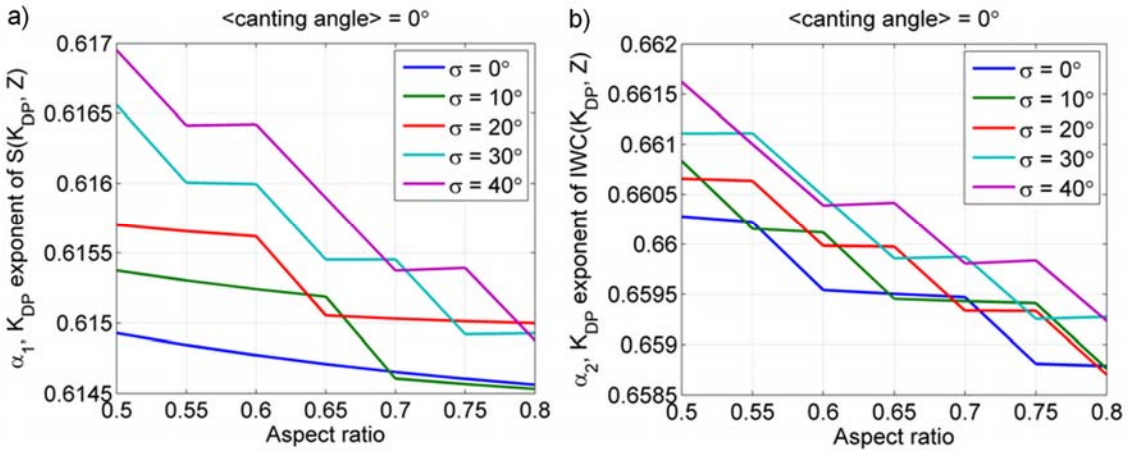



Figure 4.2: Dependence of the $K_{DP}$ exponents $\alpha_1$ and $\alpha_2$ in a) $S(K_{DP}, Z)$ and b) IWC($K_{DP}$, $Z$) on $\sigma$ and $b/a$, computed from 2DVD measurements.

shapes of the curves in Figs. 4.2 and 4.3 are consequence of the polarimetric relations exponents' discretization in an iterative procedure used to obtain exponents' optimal values.

Both $K_{DP}$ exponents, $\alpha_1$ and $\alpha_2$, from the $S(K_{DP}, Z)$ and IWC($K_{DP}$, $Z$) relations are almost constant (decrease very little) as $\sigma$ and $b/a$ simultaneously increase (Fig. 4.2). The largest change in $\alpha_1$ and $\alpha_2$ is 0.3% and 0.6% for $\sigma = 40°$ and increase in $b/a$ from 0.5 to 0.8, thus $\alpha_1$ and $\alpha_2$ can be treated as constants.

Similarly, the dependence of $Z$ exponents, $\beta_1$ and $\beta_2$, from $S(K_{DP}, Z)$ and IWC($K_{DP}$, $Z$) relations are also almost constant (Fig. 4.3). The largest change in $\beta_1$ and $\beta_2$ is 0.4% and 0.5% for $\sigma = 40°$ and increase in $b/a$ is from 0.5 to 0.8, which implies

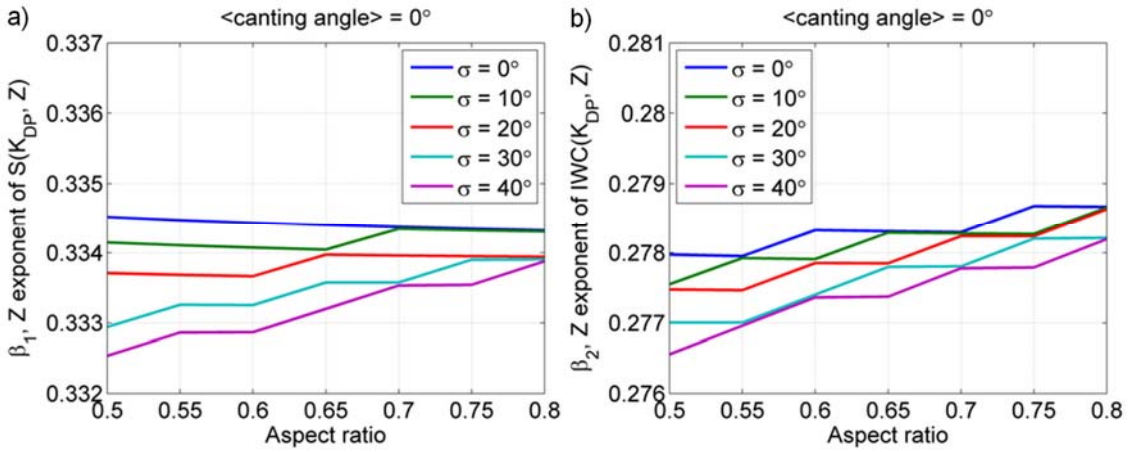



Figure 4.3: Dependence of the $Z$ exponents $\beta_1$ and $\beta_2$ in a) $S(K_{DP}, Z)$ and b) IWC($K_{DP}$, $Z$) on $\sigma$ and $b/a$, computed from 2DVD measurements.

that $\beta_1$ and $\beta_2$ can be regarded as invariant to changes in $\sigma$ and $b/a$.

The situation is dramatically different regarding the $S(K_{DP}, Z)$ and IWC($K_{DP}$, $Z$) relations' multipliers, $\gamma_1$ and $\gamma_2$; their dependence on $\sigma$ and $b/a$ is presented in Fig. 4.4. The multipliers of $S(K_{DP}, Z)$ and IWC($K_{DP}$, $Z$) relations can increase by a factor of 2 and 2.1 for constant $\sigma$ and $b/a$ between 0.5 and 0.8. If $\sigma$ and $b/a$ simultaneously increase

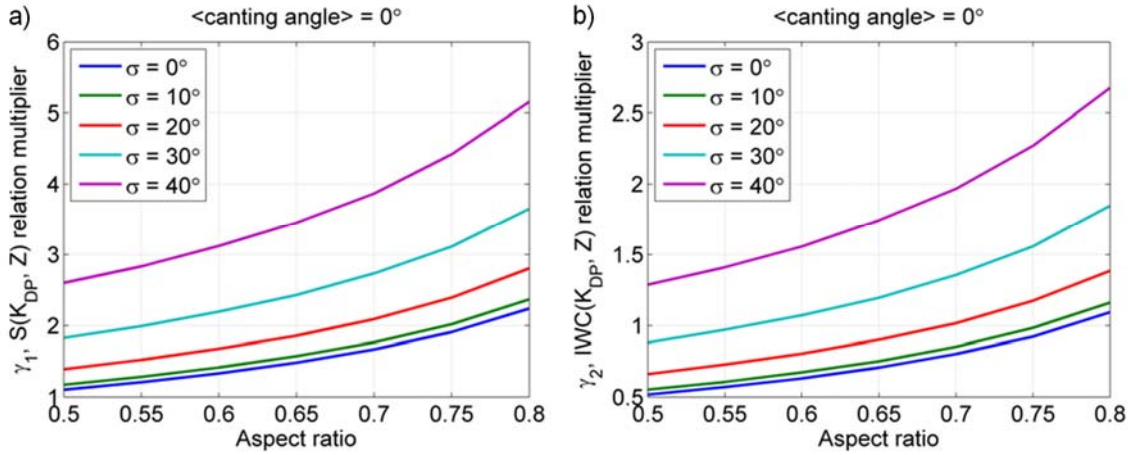



Figure 4.4: Dependence of the a) $S(K_{DP}, Z)$ and b) IWC($K_{DP}$, $Z$) relations' multipliers $\gamma_1$ and $\gamma_2$ on $\sigma$ and $b/a$, computed from 2DVD measurements.

from 0° to 40° and 0.5 to 0.7 (the later values are realistic for aggregated snow) then the increase in $\gamma_1$ and $\gamma_2$ are ~3.5 and 3.8 times, which makes a significant difference in the $S(K_{DP}, Z)$ and IWC($K_{DP}$, $Z$) values.

## 4. Verification of the polarimetric radar relations for snow on polarimetric radar data

It is demonstrated in Chapter 3 that there is significant similarity between the snow liquid-water equivalent $S$ and ice water content IWC. For brevity sake, only the verification of $S(K_{DP}, Z)$ is presented in this section; but the analogous trends and conclusions are applicable to the IWC radar estimates. Three cases are presented for $S(K_{DP}, Z)$ polarimetric radar validation in dry (mostly) aggregated snow, with high (~55 mm), and two medium (~15 mm and ~23 mm) total snow liquid-water equivalent (SWE) accumulations, for three geographical locations, Virginia, Oklahoma, and Colorado. The QVP methodology is used for verification in first two cases whereas Plan Position Indicator (PPI) data is used for Colorado dataset.

*a. 23 January 2016 east coast blizzard case, Sterling, VA*

The first snowstorm used for verification, 23 January 2016 east coast blizzard, produced about 55 mm of snow liquid-water equivalent in 24 hours. The storm disrupted the day's activities and services from New York to Washington DC area, affecting a vast number of people. The maps of total snow liquid-water equivalent obtained by using the standard $S(Z)$ relation on several WSR-88D radars (Ryzhkov 2016 white paper) were unsatisfactory in comparison to the heated gauge total accumulation. Also, many heated rain gauges showed much smaller amounts of

precipitation due to partially melted or windblown snow. It is well known that widely used $S(Z)$ relations are notoriously inaccurate because of inadequate representation of variability in snow PSDs. The inclusion of $K_{DP}$ in $S(K_{DP}, Z)$ may be a partial remedy for inadequate snow PSD variability handling by $S(Z)$, but the downside is reflected in $S(K_{DP}, Z)$'s multiplier dependence on $\sigma$ and $b/a$. The KLWX QVPs (19.5° elevation angle) of $Z$, $K_{DP}$, $Z_{DR}$, and $S(K_{DP}, Z)$ in time vs. height format are presented in Fig. 4.5.

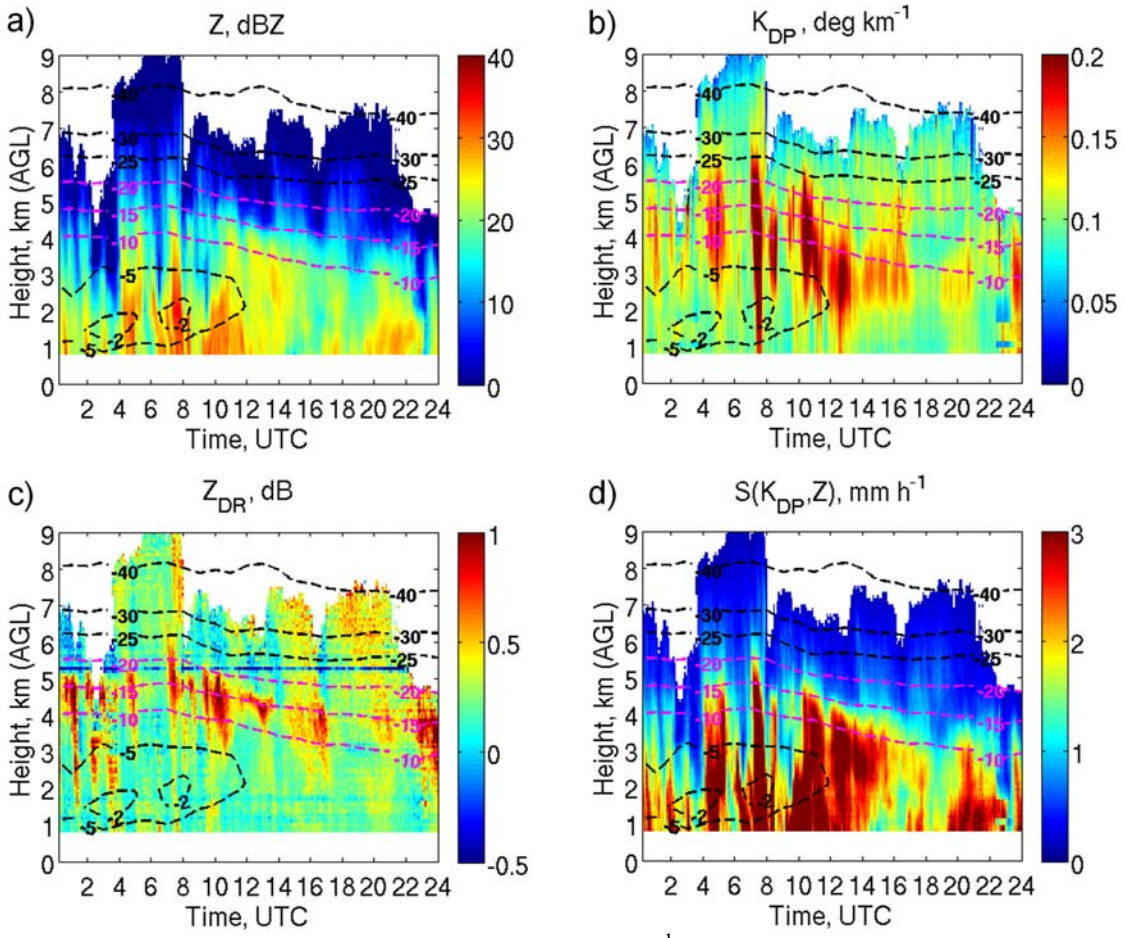



Figure 4.5: QVPs of a) Z in dBZ, b) $K_{DP}$ in deg km$^{-1}$, c) $Z_{DR}$ in dB, and d) S($K_{DP}$, Z) in mm h$^{-1}$, KLWX 19.5° radar elevation angle, Sterling VA, 23 January 2016. The black dashed lines are isotherms, where the layer from -10°C to -20°C highlighted in magenta represents DGL.

The black dashed lines are isotherms estimated from Rapid Refresh (RAP) model, where the dendritic growth layer (DGL) from -10°C to -20°C is highlighted in magenta.

There are some very informative features visible in QVPs of $K_{DP}$ and $Z_{DR}$ within the DGL: the mid-level maxima in both of these variables. The $K_{DP}$ maxima are associated with the higher ice particle concentration ($K_{DP}$ is usually very low in aggregated snow close to the ground). It is known that in DGL (temperature range from -10°C to -20°C) dendrites and plates have the strongest growth (hence DGL – dendritic growth layer) at the expense of the water vapor. About 80% – 90% of total precipitation is formed in this layer, which, as seen from the QVPs of $K_{DP}$ and $Z_{DR}$, has some pronounced signatures. This is mainly because of non-sphericity in ice particles shapes and higher density of particles in the DGL aloft. Further below the DGL aggregation occurs, which decreases the density of the snow particles and redistributes the mass across the size spectrum. Close to the ground, both $K_{DP}$ and $Z_{DR}$ are near zero due to more spherical shapes of the aggregates and low particles' densities.

$S(K_{DP}, Z)$ is almost constant from the bottom of the DGL to the ground; ideally a constant values are expected if the mass flux is conserved through this portion of the atmosphere. Often, $Z$ and $K_{DP}$ complement each other in the vertical column. Reflectivity is rather low in DGL whereas $K_{DP}$ is high. It is the opposite below the DGL towards the ground where $Z$ is increasing, due to increased particle sizes in aggregated snow, and $K_{DP}$ decreases because of particles' increased sphericity and reduction in particles' concentration and aggregates' density.

Verification of the new polarimetric snow measurement concept is presented through comparisons of $S(K_{DP}, Z)$ relations with collocated reference ground measurements and several $S(Z)$ standard WSR-88D relations (Fig. 4.6). The vertical profiles of total snow accumulations (Fig. 4.6) are obtained via multiplying $S(Z)$s and

$S(K_{DP}, Z)$s by the time interval between the radar scans, and at the constant heights, summing the corresponding results throughout the duration of the storm. Both $S(K_{DP}, Z)$ relations used for comparison provide better estimates of total SWE than corresponding $S(Z)$ relations. The two $S(K_{DP}, Z)$ relations are derived for different aspect ratios and

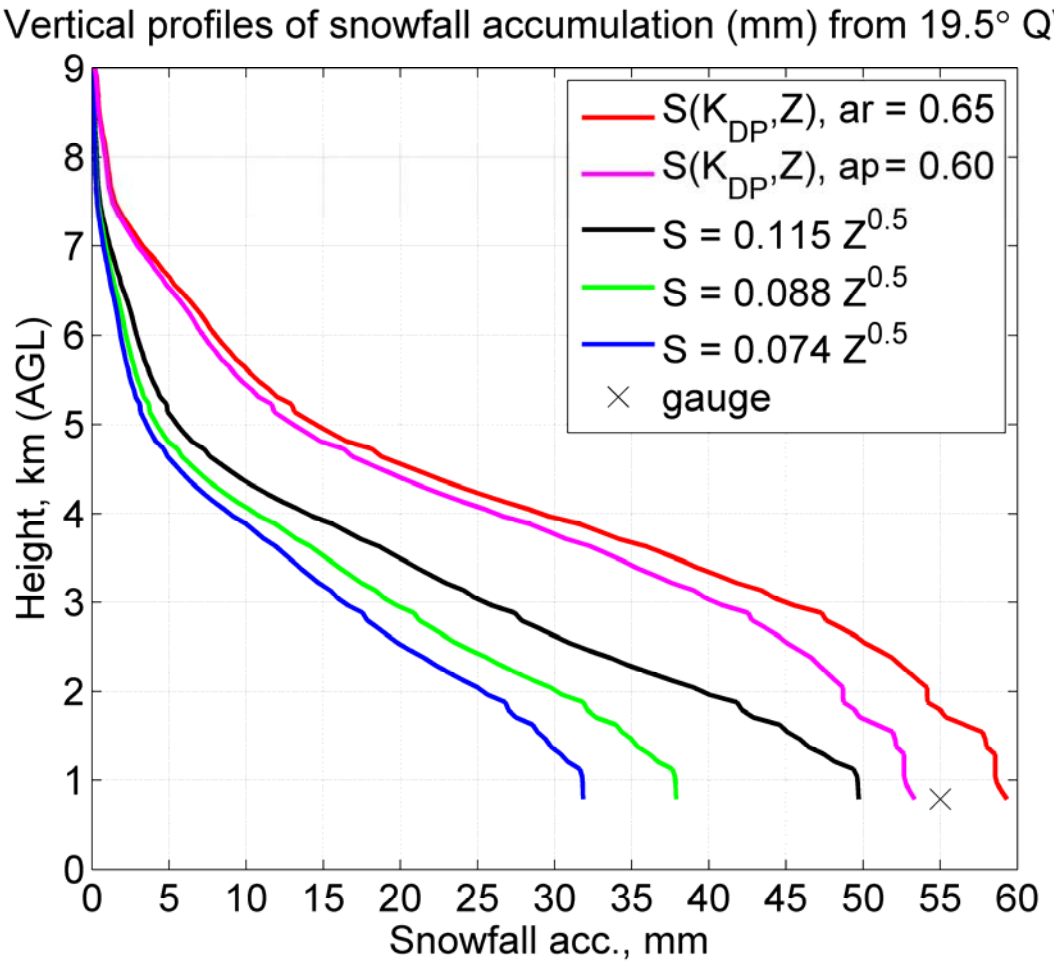



Figure 4.6: Vertical profiles of total snow accumulation obtained from KLWX 19.5° QVPs using various $S(Z)$s and $S(K_{DP}, Z)$ relations (red: aspect ratio – ar = $(b/a)_{0°}$ = 0.65, magenta: apparent aspect ratio – ap = $(b/a)_{19.5°}$ = 0.6, obtained from $(b/a)_{0°}$ = 0.55 via Eq. 4.1) for 23 January 2016. The X represents reference ground measurements of snow liquid-water equivalent presented at the lowest snowfall accumulation height for convenience.

radar elevation angles; the red line corresponds to 0° radar elevation and particle aspect ratio 0.65 (Eq. (3.27) in Chapter 3), whereas magenta line is derived for 0° elevation and $b/a$ = 0.55, but adjusted for 19.5° radar elevation angle. Note that with increasing

radar elevation angle, particle aspect ratio changes via Eq. (4.1), and should be taken into account. In this case $b/a = 0.55$ aspect ratio at 0° radar elevation becomes apparent aspect ratio $(b/a)_\theta = 0.6$ at 19.5°, as shown in Fig. 4.1. Then for practical use, the multiplier $\gamma_1$ of the $S(K_{DP}, Z)$ relation for $b/a = 0.6$ can be estimated from Fig. 4.4 and used for $S(K_{DP}, Z)$ computation adjusted for corresponding radar elevation. The range for the aspect ratios in aggregated snow is typically from 0.5-0.7, and some recent studies (e.g. Garrett et al. 2015) advocate the use of $b/a = 0.55$. Garrett et al. 2015 obtained this value with MASC system at the ground level.

Another notable feature in the Fig. 4.6 is the "nonphysical" slope of the total SWE estimated from $S(Z)$ relations. If saturation with respect to ice occurs below DGL all the way to the ground, then conservation of mass is preserved. As aggregation strengthens – $Z$ increases (as a consequence of aggregation the number of smaller anisotropic particles is deflated in the process – $K_{DP}$ decreases). Thus, it is expected that total SWE estimated from $S(Z)$ have an almost constant profile from below DGL and all the way to the ground because 80% - 90% of snow is produced in the DGL. In this case $S(Z)$s produce ~16, 19, and 25 mm at about 3 km AGL, which is ~50% of their total estimation at the ground level. On the other hand, both of $S(K_{DP}, Z)$ relations produce ~75% - 76% at ~ 3km AGL of their total amount at the ground level. Also, $S(K_{DP}, Z)$ relations estimates of total SWE (Fig. 4.6: magenta and red line) are within ± 4% - 7% of reference ground measurement (55 mm), whereas $S(Z)$s underestimate total SWE by 42%, 31%, and 10% (Fig. 4.6: blue, green, and black lines, respectively). Clearly, $S(K_{DP}, Z)$ relations give physically more realistic profiles and more accurate total SWE amounts than the standard WSR-88D $S(Z)$ relations in this case.

*b. 1 February 2011 case, Norman, Oklahoma*

The 1 February 2011 snowstorm had a big impact on life in Oklahoma. It almost completely shut down central and northwestern parts of the state because of high snow accumulations on the ground, from 12'' to 19'' (~30-50 cm) measured by the ruler. Western parts of Oklahoma saw 1-4 inches (about 2.5-10 cm) of snow depths on the ground. The measurements of total SWE in Norman were between 12 mm and 18 mm (determined from the storm snow depth reports and converted by 10:1 rule), about 15.3 mm on average, which is adopted as one of the ground reference measurements. The Norman Oklahoma Mesonet measurement of total SWE (few days after the storm, when snow melted) was ~ 12.9 mm.

The QVPs of $Z$, $K_{DP}$, $Z_{DR}$, and $S(K_{DP}, Z)$ presented in Fig. 4.7 show very interesting storm structure. There is a prominent bright band at about 1.8 km AGL, evident in $Z$ and $Z_{DR}$ enhancements from ~0300 until ~0845 UTC, but not as much in $K_{DP}$ (most likely due to high elevation tilt of 19.5° used for QVP). There is also refreezing layer below the melting, as indicated by RUC model temperature profiles. The METAR reports (not shown) indicate that for the entirety of the event only snow was present on the ground, another independent confirmation of refreezing, which implies that some other type except the aggregated snow (perhaps rimed) could be present on the ground during that period. The enhancements in $K_{DP}$ from 0300 to 1200 UTC (and also from ~1630 to 1700) are clearly visible in dendritic growth layer, between -10°C and -20°C. Another prominent feature in QVPs is localized moderate reduction in $Z$ and slight enhancement in $Z_{DR}$ (and also small reduction in co-polar correlation coefficient $\rho_{hv}$, not shown) at about 1.8 km AGL from ~0940 until 1340

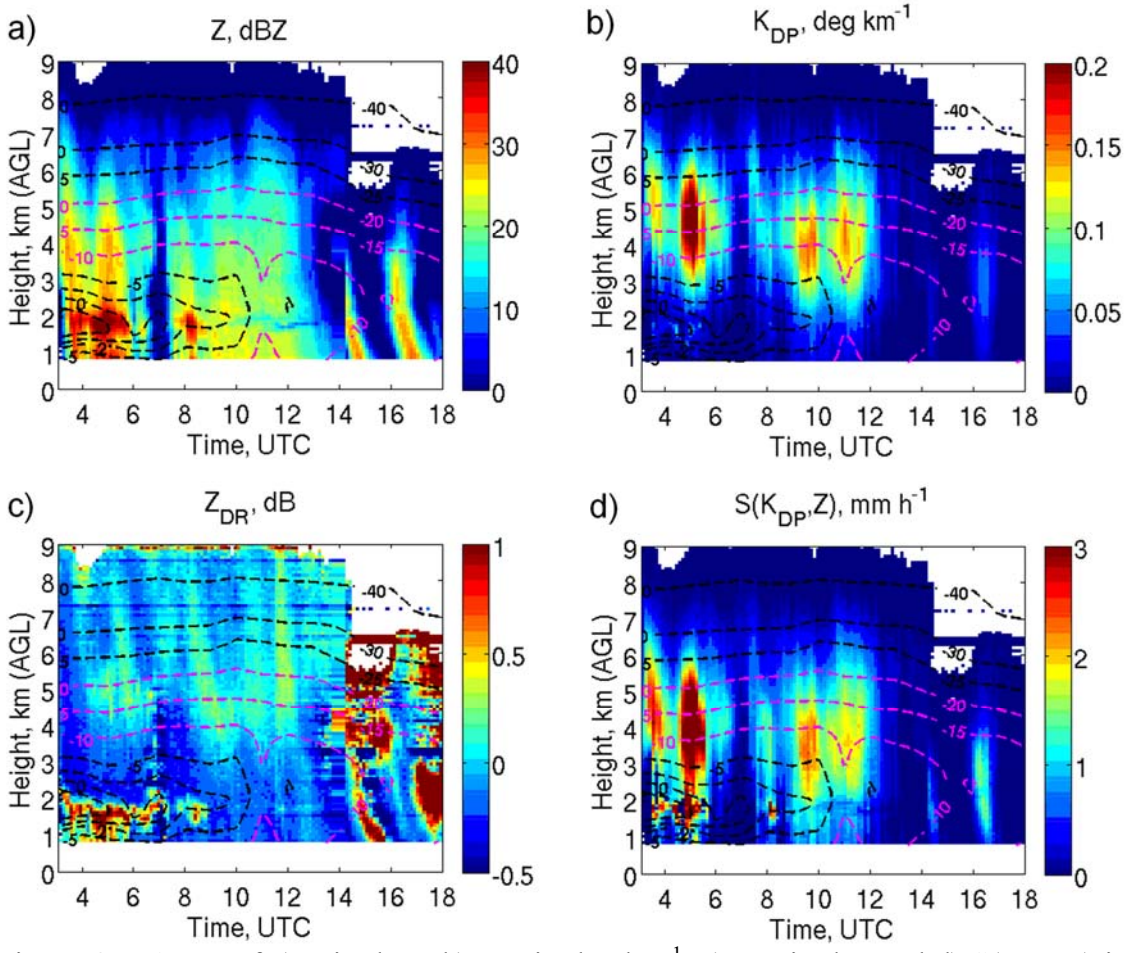



Figure 4.7: QVPs of a) $Z$ in dBZ, b) $K_{DP}$ in deg km$^{-1}$, c) $Z_{DR}$ in dB, and d) S($K_{DP}$, $Z$) in mm h$^{-1}$, KOUN 19.5° radar elevation angle, Norman OK, 1 February 2011. The black dashed lines are isotherms, where the layer from -10°C to -20°C highlighted in magenta represents DGL.

UTC. This is an indication of the refreezing signature. The hypothesis is that partially melted particles from the melting layer may have been sustained at that level with the help of the wind shear and turbulence, which refroze as time progressed.

The QVPs of signal to noise ratio SNR (dB) and spectrum width SW (m s$^{-1}$) are shown in Fig. 4.8. There is a decrease in SNR from ~0930 to 1330 UTC at about 1.5 to 2 km height AGL, but values are well above 30 dB, making the associated structure in SW valid (although this is the QVP, thus the interpretations should be taken with

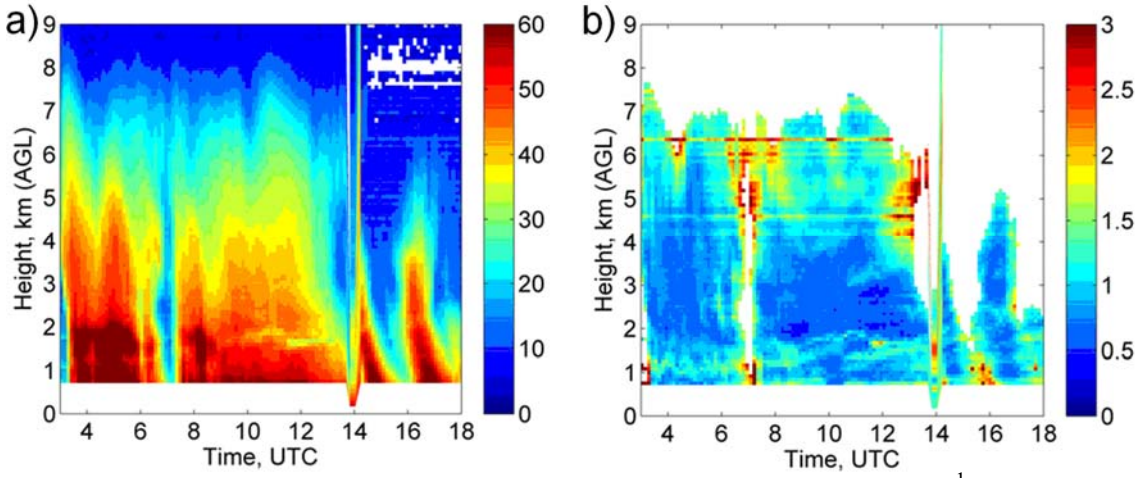



Figure 4.8: QVPs of a) SNR (dB) and b) spectrum width SW (m $s^{-1}$) from 19.5° elevation, KOUN, 1 February 2011. The threshold of 20 dB in SNR is applied to SW.

caution). The high values of SW at the edges of the echo are most likely associated with relatively low SNR but because of azimuthal averaging they are included in graphical representation. From the beginning of the event, the layer centered at ~1 km height AGL (it is bit higher ~1.5 km height from 0930 until 1330 UTC) shows signs of moderate SW values (1.5 m $s^{-1}$), indicating the presence of wind shear and possibly turbulence. This is important because $K_{DP}$ is lower in the wind sheared and turbulent air due to more random particle orientations, and is possibly reflected in reduction in total SWE profile below the DGL, obtained from $S(K_{DP}, Z)$ (see Fig. 4.9).

Comparisons between the three standard $S(Z)$ and two $S(K_{DP}, Z)$ estimates of total SWE, obtained from QVPs, along with the ground reference measurements are shown in Fig. 4.9. First, $S(K_{DP}, Z)$ estimates have primary maximums in DGL as opposed to $S(Z)$ relations (melting layer maxima). This is important if wind shear and turbulence is present because 80% to 90% of snow precipitation is formed in the DGL. The hypothesis that the $S(K_{DP}, Z)$ from DGL can be used for estimation of total SWE amount on the ground seems very plausible for this type of situation (wind shear and

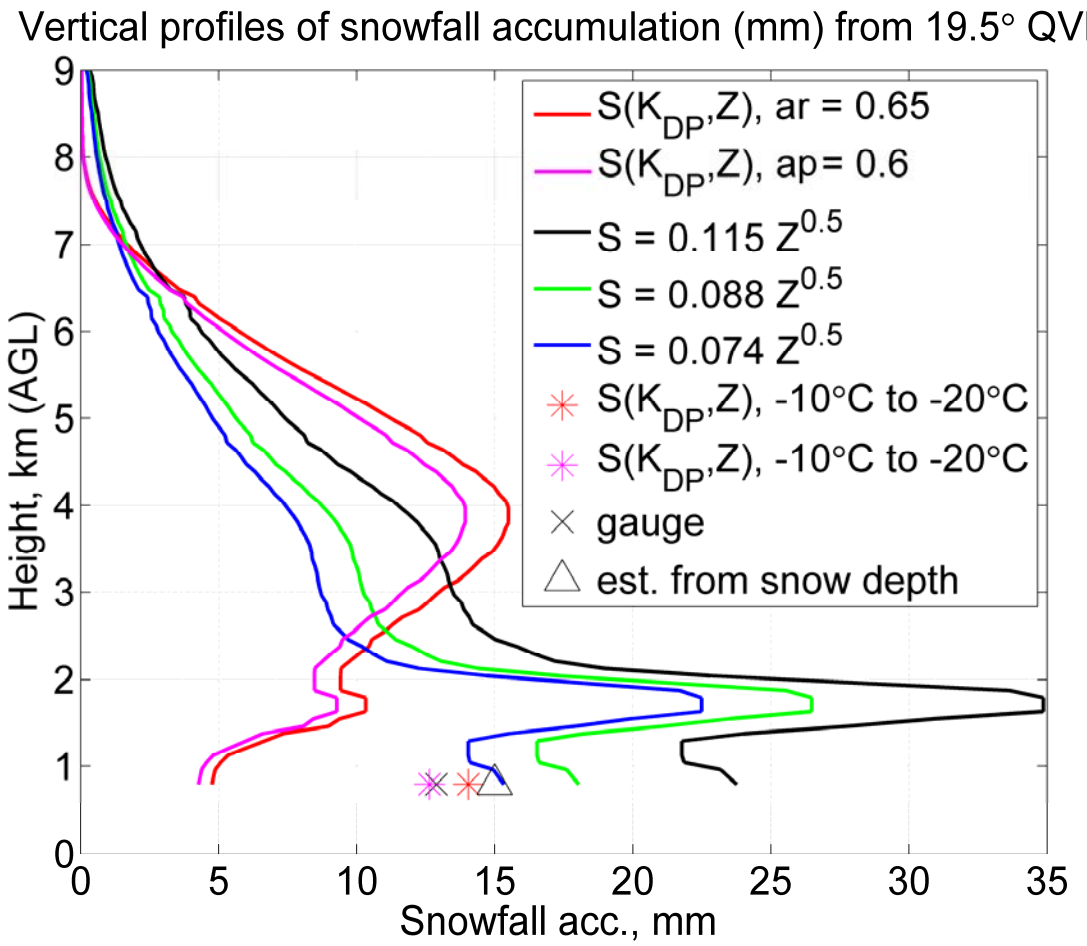



Figure 4.9: Vertical profiles of total snow liquid-water equivalent accumulation obtained from KOUN 19.5° QVPs using various $S(Z)$s and $S(K_{DP}, Z)$ relations (red: aspect ratio – ar = $(b/a)_{0°}$ = 0.65, magenta: apparent aspect ratio – ap = $(b/a)_{19.5°}$ = 0.6, obtained from $(b/a)_{0°}$ = 0.55 via Eq. 4.1) for 1 February 2011. The X represents reference ground measurements of snow liquid-water equivalent from Oklahoma Mesonet, whereas Δ is the estimate form the average snow depth measured by ruler across Norman, OK, using the 10:1 conversion rule, presented at the lowest snowfall accumulation height for convenience. Red and magenta asterisks are $S(K_{DP}, Z)$ estimates using aspect ratios of 0.65 and 0.6 respectively, but from DGL (-10°C to -20°C).

turbulence are mostly below the DGL). Although the total SWE profile amounts estimated from $S(K_{DP}, Z)$ are underestimated close to the ground (~5 mm), their estimates from DGL (12.6 to 14.2 mm) are in excellent agreement with the reference ground measurements (~13 to 15 mm). The $S(Z)$ relations display very unrealistic total SWE profiles due to inclusion of the melting layer. But some of the $S(Z)$s have total

SWE estimates (~15.5 and 18 mm) at the lowest elevations similar to the ground measurements, which in this case is rather fortuitous.

*c. 28 January 2013 case, Grand Mesa, Colorado – Instantaneous snowfall rate verification*

From January until April 2013 the winter precipitation measurement experiment was conducted in the vicinity of Grand Mesa, CO, funded by Water Conservation Board of Colorado. One of the main goals of this experiment was to mitigate the beam blockage of the ~35°-40° azimuthal sector towards the east of the KGJX WSR-88D radar located in Grand Junction, CO. The case chosen for presentation had the largest amount of SWE (22.9 mm) recorded with the heated rain gauge located at about 20.9 km and 97.8° azimuth from the KGJX. The location of the ground instrumentation was in the midst of the beam blockage sector. Because the lowest radar elevations (0.5°, 0.9°) are affected by this blockage, the next available (not affected) elevation (1.29°) is used for verification of $S(K_{DP}, Z)$ relations.

The instantaneous snowfall rate $S$ obtained from 1.29° (450m AGL, 3500m MSL at the instrumentation location) scan is in Fig. 4.10. The data is computed as median value of 5 range gates by 3° azimuth sector (median of 30 data points, about 1.2 km in diameter) extracted directly above the reference ground measurement location. The $S(K_{DP}, Z)$ relation used in this case is the one derived for the Colorado dataset, $S_{CO}(K_{DP}, Z) = 1.88\ K_{DP}^{0.61} Z^{0.34}$, as described in Chapter 3, along with the standard $S(Z)$ relation of Vasiloff (1997); the $S(Z)$ relation from Wolfe et al. (2015) is tuned for this region, but Vasiloff (1997) produces better comparison with the gauge for this case. The relation $S_{CO}(K_{DP}, Z)$ follows more closely and consistently the ground reference

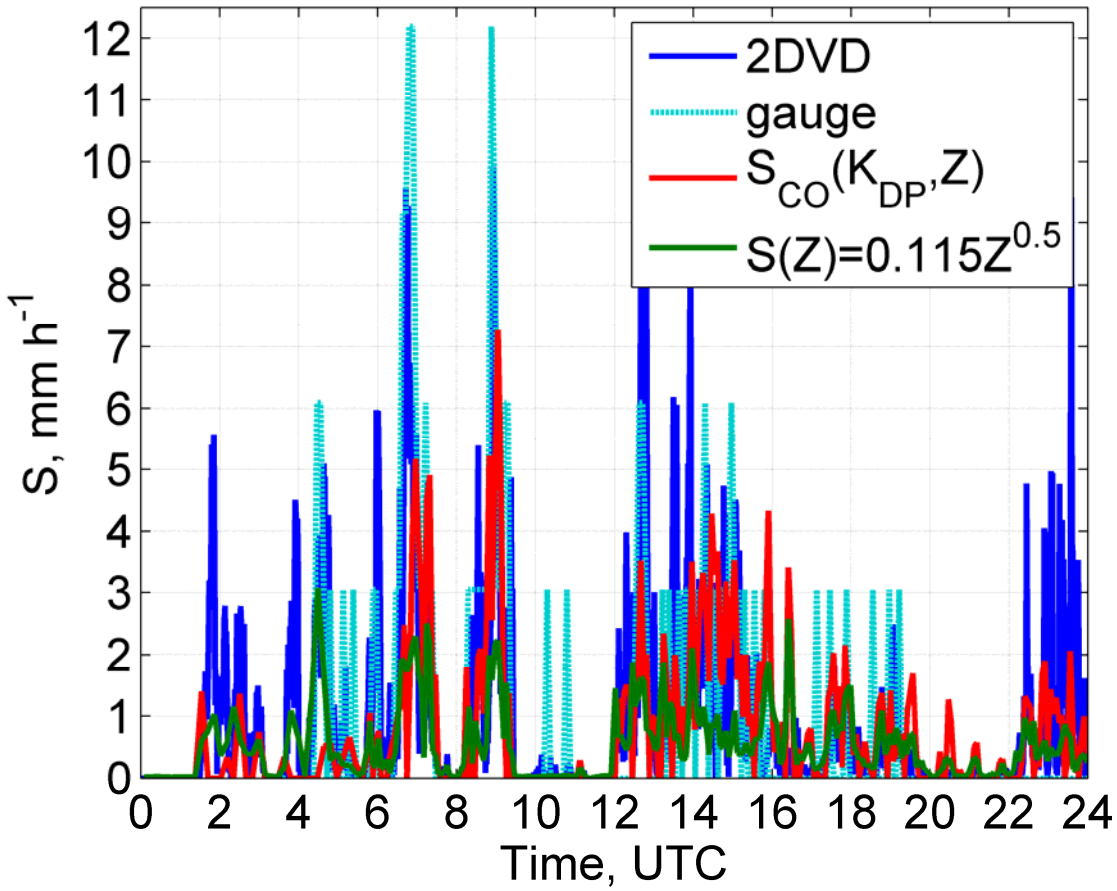



Figure 4.10: Instantaneous snowfall rate from heated rain gauge (dashed cyan line), 2DVD (blue line), $S_{CO}(K_{DP}, Z)$ (red line) and $S(Z)$ (green line) relations; 28 January 2013, Grand Mesa, CO.

measurement compared to $S(Z)$ relation. The only discrepancy occurred at the onset of the precipitation recorded with the heated gauge, from ~0400 to 0430 UTC, when $S(Z)$ produced values closer to the gauge measurements. In this period, there was moderate number of relatively large particles present, which $S_{CO}(K_{DP}, Z)$ couldn't properly address. At the end of the event, from 2200 to 2400 UTC, both $S_{CO}(K_{DP}, Z)$ and $S(Z)$ show some light precipitation, but there was no record from the gauge. A few hours in the next day the gauge recorded ~1.5 mm of SWE, but this amount is not taken into account due to some light precipitation coincidently occurring. The time lag could also be (partially) attributed to low temperatures which dropped below -10°C at this point.

There are some discrepancies between the gauge and 2DVD measurements, but those are attributed to discretization and different temporal resolutions between the instruments. The $S_{CO}(K_{DP}, Z)$ estimate is more consistent with the 2DVD measurements than the $S(Z)$ relations' output.

Snow liquid-water equivalent accumulations from heated gauge, 2DVD, Colorado $S_{CO}(K_{DP}, Z)$, Oklahoma $S(K_{DP}, Z)$ (Eq. 3.27), and standard $S(Z)$ relations are presented in Fig. 4.11. Without taking into account the lagged gauge measurements, the $S_{CO}(K_{DP}, Z)$ relation produced the closest SWE amount (~18 mm) to the reference measurements (~22.9 mm), about 21% smaller. Also, the Oklahoma $S(K_{DP}, Z)$ had

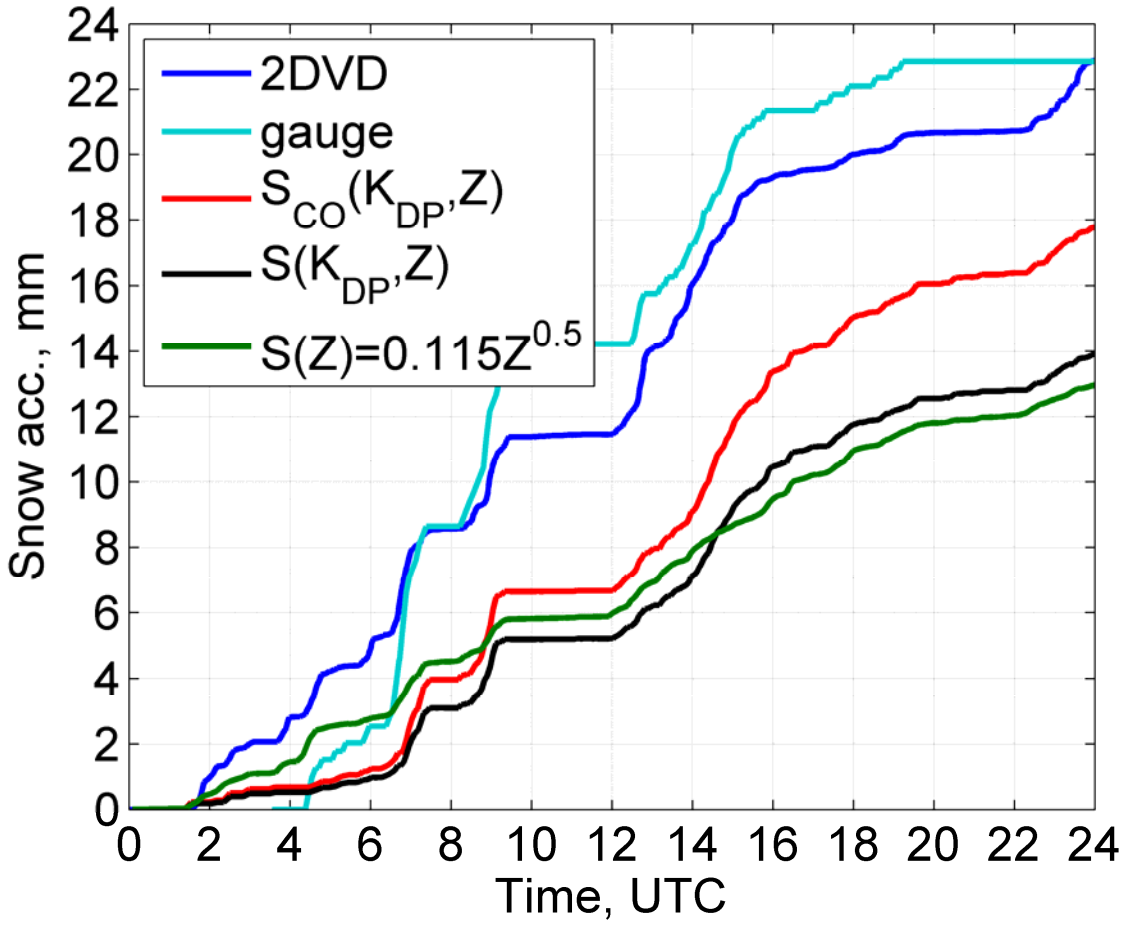



Figure 4.11: SWE accumulations from heated rain gauge (cyan line), 2DVD (blue line), $S_{CO}(K_{DP}, Z)$ (red line), $S(K_{DP}, Z)$ (black line), and $S(Z)$ (green line) relations; 28 January 2013, Grand Mesa, CO.

closer values (~14 mm) than $S(Z)$ (~13 mm), ~39% and 43% smaller in comparison to the ground reference. The estimates from the $S(K_{DP}, Z)$s are in accord with the difference in the relations' multipliers, which is 21% higher for the Colorado relation. The shapes of both $S(K_{DP}, Z)$ curves resemble more the heated gauge, and especially 2DVD accumulations, than the $S(Z)$ counterparts. This is another example of the potentially universal character of the $S(K_{DP}, Z)$ relations, where the application to the radar data above the gauge location produced credible results.

## 5. Discussion

The primary source of uncertainty in the estimation of $S$ (IWC) comes from the sensitivity of the polarimetric snow relations to snowflake shapes, orientations and degree of riming (density change). Snow gauge measurements at the surface, aircraft probes in situ, and polarimetric radar observations can be used to evaluate this uncertainty. Hence using the polarimetric radar data, the "adjustment" of proposed polarimetric relations, and more specifically their multipliers, could be obtained experimentally. Clearly further study of the subject is in order.

Analysis of $K_{DP}$ measurements in snow at S-band indicates that $K_{DP}$ is usually low and noisy in heavily aggregated dry snow and its reliable estimation may require spatial averaging over relatively large areas (Ryzhkov and Zrnic 1998). The situation is better at C and X bands because $K_{DP}$ is inversely proportional to the radar wavelength. Because our computations have been performed for S-band ($\lambda$ = 11.08 cm), the corresponding relations at other wavelengths within this band and at shorter wavelengths can be obtained by wavelength scaling of $K_{DP}$. The C and X band relations

might need additional tuning according to the type of snow and reference ground measurements.

The new polarimetric radar processing techniques, such as Quasi-Vertical Profiles (Ryzhkov et al. 2016; Griffin et al. 2017) and Enhanced Vertical Profiles (Bukovčić et al. 2017a) based on azimuthal averaging to reduce the statistical error of the $K_{DP}$ estimate, can significantly improve the quality of radar snowfall measurements. Oversampling of the differential phase data at spacing considerably lower than the length of the radar pulse could additionally improve the $K_{DP}$ accuracy. Another possibility is to capitalize on the $K_{DP}$ measurements in the dendritic growth layer (DGL) at the temperature interval between -10°C and -20°C where $K_{DP}$ is significantly higher than at warmer temperatures below the DGL (e.g., Kennedy and Rutledge 2011; Bechini et al. 2013) and make projections down to the surface assuming that snow rate or ice water content are conserved in the process of aggregation. These options should be further explored in future research.

## 6. Summary

Verification of polarimetric radar $S(K_{DP}, Z)$ relations in three geographical regions, Virginia, Oklahoma, and Colorado via reference ground measurements and comparison with standard $S(Z)$ relations increase confidence in the applicability of this novel concept. But polarimetric measurements have issues that need to be dealt with. Specific differential phase $K_{DP}$ heavily depends on particle density, aspect ratio $b/a$, and even more on width of the canting angle distribution $\sigma$. Consequently, multipliers of $S(K_{DP}, Z)$ and IWC($K_{DP}$, $Z$), $\gamma_1$ and $\gamma_2$, profoundly depend on these quantities. The $K_{DP}$

and $Z$ exponents of both relations are practically invariant to these changes in snow density, $b/a$ and $\sigma$. The current approach relies on some values of these parameters from the existing literature, but future study is needed to solidify these estimates.

The use of the same $S(K_{DP}, Z)$ relation(s) in three distinct geographical regions (Virginia, Oklahoma, and Colorado) produced encouraging results, implying potentially universal character of these relations. There is an indication that if there is no presence of wind shear or turbulence, polarimetric relations produce more realistic profiles than standard $S(Z)$ estimates. If turbulence and shear are present in lower levels (as indicated by spectrum width), more accurate estimates of $S$ from $S(K_{DP}, Z)$ are obtained from the dendritic growth layer, where 80% to 90% of total precipitation is produced. The use of localized averaging on PPI data may produce adequate accuracy of $K_{DP}$ (as shown in Colorado case) and increase the usability of polarimetric relations. In addition, instantaneous snowfall rate from polarimetric relations obtained from PPI data in Colorado show better agreement with the ground measurements in comparison to the standard $S(Z)$ relation tuned for that region.

The practicality of the newly obtained polarimetric relations for snow measurements is contingent on the reliable estimate of $K_{DP}$ which is notoriously noisy in aggregated snow. Such noisiness can be mitigated by the use of spatial averaging and utilization of $K_{DP}$ measurements aloft in the dendritic growth layer (centered at the -15°C isotherm) where the magnitude of $K_{DP}$ is significantly higher than in heavily aggregated snow near the surface, or just above the freezing level. Under the assumption that the mass flux is conserved, projection of the $S(K_{DP}, Z)$ values from this layer to the ground should produce values in better agreement with ground

measurements. Sensitivity of polarimetric relations to the temperature and relative humidity change are not directly taken into account in the present study, and should be a subject of a future study.

# Chapter 5: Summary of Conclusions and Future work

This dissertation deals with measurements of frozen precipitation in winter storms. It consists of three main parts: 1) case study of polarimetric radar observations of ice pellets and their quantification with disdrometer; 2) the development of polarimetric radar relations in aggregated snow using the disdrometer data from 16 snow storms in Oklahoma (including 2DVD validation in Oklahoma, Colorado and Ontario); 3) verification of these relations with polarimetric radar data (Virginia, Colorado and Oklahoma).

The following summarizes principal findings.

1) It is very challenging to recognize ice pellets with polarimetric radar in localized areas away from radar. By introducing new data displaying techniques, Slanted Vertical Profiles SVPs (and also Enhanced Vertical Profiles EVPs) the recognition of ice pellets (phase transition from liquid to solid precipitation) became doable and more evident.

Polarimetric signatures of particle refreezing are confirmed with collocated 2DVD and other observations, and the amounts of frozen precipitation are quantified. Disdrometer data revealed that there were two types/modes of ice pellets, less frequent slow falling (1 to 3 m $s^{-1}$), and vastly present fast falling, with velocities close to raindrops of similar size.

The patchy, localized structure of the refreezing signature is evident in PPIs, displaying the local enhancement in $Z_{DR}$ and reduction in both $Z_H$ and $\rho_{hv}$, with the small magnitude of $Z_{DR}$ enhancement from 0.1 to 0.3 dB, due to refreezing of relatively smaller particles (ice pellets with diameter up to 4 mm are recorded via 2DVD). It is

rather spatial and temporal changes of $Z_H$, $Z_{DR}$, and $\rho_{hv}$ that reveal the locations of refreezing, whereas their magnitudes per se are not sufficient for this identification.

The refreezing processes occurred much closer to the ground in comparison to previous studies (Ryzhkov et al. 2011a, and Kumjian et al. 2013). The presence of multiple melting and freezing layers and relatively high freezing temperatures (>-3.5°C within refreezing zones), indicated that preferential freezing of smaller drops is most likely the mechanism for producing polarimetric refreezing signatures.

It is shown through model (Marshal-Palmer) simulations and 2DVD observations that the refreezing signature is complex, depending on the particle sizes (smaller drops freeze faster) and the width of the particle size spectra. The refreezing signature of $Z_{DR}$ is especially interesting; $Z_{DR}$ initially increases during the preferential freezing of small drops, but it drops substantially as large drops sequentially start to freeze, as confirmed by 2DVD observations. Thus, the enhancement of the $Z_{DR}$ may be followed by a substantial reduction over a small vertical distance, which indicates that the refreezing signatures are altitude (due to temperature) dependent.

2) Outlined in this study are basic principles for polarimetric measurements, via combined use of $Z$ and $K_{DP}$, of snow liquid-water equivalent $S$ and ice water content IWC. Compared to the traditional $Z$-based estimators, the combination of $Z$ and $K_{DP}$ dramatically reduces the uncertainty in the estimates of $S$ and IWC caused by the variability of snow size distribution, as indicated from the analysis of 2D video disdrometer data in dry snow.

Before the derivation of the polarimetric relations for $S$ and IWC from 2D video disdrometer, a problem of particle mismatching is addressed by filtering out the

obviously mismatched particles with discriminating thresholds (determined from the reference gauges). To mitigate the impact of density variability the so-called "adjusted" snow density (obtained from 2DVD terminal velocity measurements) is used for computations of polarimetric variables and microphysical parameters. The disdrometer measurements are also used for verification of the theoretical relations for $S(Z)$ and IWC($Z$) parameterization by the intercept $N_{0s}$ of the exponential size distribution.

The key finding of this study is that snow rate $S$ and ice water content IWC can be obtained from the bivariate power-law relations $S = \gamma_1 K_{DP}^{\alpha_1} Z^{\beta_1}$ (Eq. 3.27) and $\mathrm{IWC} = \gamma_2 K_{DP}^{\alpha_2} Z^{\beta_2}$ (Eq. 3.28). The multipliers $\gamma_1$ and $\gamma_2$ heavily depend on the particle orientations, shapes, and degree of riming (snow density), whereas the exponents $\alpha_1$, $\alpha_2$, $\beta_1$, and $\beta_2$ are practically invariant. These multipliers can be determined experimentally by comparing in situ measurements of $S$ and IWC with polarimetric radar data. In addition, the polarimetric relations for the intercept $N_{0s}$ and slope parameter $\Lambda_s$ of the exponential size distribution, $N_{0s}(K_{DP}, Z)$ and $\Lambda_s(K_{DP}, Z)$, are derived and can be used for direct microphysical retrievals from the polarimetric radar measurements. As for $S(K_{DP}, Z)$ and IWC($K_{DP}$, $Z$) multipliers and exponents, the similar dependency exists for $N_{0s}(K_{DP}, Z)$ and $\Lambda_s(K_{DP}, Z)$ counterparts.

The disdrometer measurements of 16 (dry, aggregated) snow events in Oklahoma served for derivation of $S(K_{DP}, Z)$ and IWC($K_{DP}$, $Z$) relations. Besides an excellent performance locally (Oklahoma), these relations perform reasonably well for snowstorms in two distinct climate regions, Colorado and especially Canada, giving a rise to a potentially universal character of such relations. To improve performance of $S(K_{DP}, Z)$ or IWC($K_{DP}$, $Z$) in distinct climate regions such as Colorado, only the

multiplier in $S(K_{DP}, Z)$ or IWC($K_{DP}$, $Z$) needs to be adjusted. This is verified by applying relations $S_{CO}(K_{DP}, Z)$ and $IWC_{CO}(K_{DP}, Z)$ derived from Colorado dataset to the Oklahoma dataset where Colorado polarimetric relations' multipliers are somewhat higher than their Oklahoma counterparts. Although it appears that the derived relations may be widely applicable, this needs to be further investigated.

The correlation coefficient is much higher (~0.99) between the measured $S$ (IWC) and estimated $S(K_{DP}, Z)$ (IWC($K_{DP}$, $Z$)) than between the measurements and $S(Z)$ (IWC($Z$)) estimates (corr. coeff. ~0.8 to ~0.89). This indicates that the PSD variability is much better handled in the polarimetric snow relations in comparison to the standard $S$(Z) relations, increasing the confidence of the novel approach. This is because $K_{DP}$ is proportional to the first moment (and thus particle concentration) and $Z$ to the fourth moment of the PSD in aggregated (low density) snow, and their combination in $S(K_{DP}$, $Z$) and IWC($K_{DP}$, $Z$) is close to the second PSD moment. The intrinsic $S$ and IWC are also vey close to the second PSD moment (with $S$ closer to the 2.2 moment) and that explains the success of our method.

In aggregated snow $K_{DP}$ is notoriously noisy, thus the practicality of the newly obtained polarimetric relations for snow measurements is contingent on the reliable $K_{DP}$ estimate. Such noisiness can be mitigated by the use of spatial averaging (e.g. QVPs, EVPs, etc.). Another remedy for $K_{DP}$ noisiness is utilization of $K_{DP}$ measurements aloft in the dendritic growth layer DGL centered at the -15°C isotherm. The magnitude of $K_{DP}$ is significantly higher in the DGL than in heavily aggregated snow near the surface or just above the freezing level.

3) Microphysical properties of precipitation affect differently the polarimetric variables. For example, specific differential phase $K_{DP}$ heavily depends on the width of the particle canting angle distribution $\sigma$, and to a somewhat lesser extent particle aspect ratio $b/a$ and density, thus, multipliers of $S(K_{DP}, Z)$ and IWC($K_{DP}$, $Z$), $\gamma_1$ and $\gamma_2$, are inherently dependant on these parameters. On the other hand, all the exponents of $K_{DP}$ and $Z$ in polarimetric relations are practically invariant to these parameters' variability. The current application of polarimetric relations relies on some values of these parameters from the existing literature, but further refinement is defrayed to future studies.

Polarimetric radar $S(K_{DP}, Z)$ relations applied to radar data are verified with the reference ground measurements in three geographical regions, Virginia, Oklahoma, and Colorado. The use of the same $S(K_{DP}, Z)$ relation(s) in three distinct geographical localities is encouraging, implying potentially universal character of these relations. In the absence of wind shear or turbulence in the atmosphere, polarimetric relations produce more realistic profiles than the standard $S(Z)$. Also, if $K_{DP}$ estimate has small error (e.g. large azimuthal averaging in QVPs, or localized averaging as in Colorado case reduces the statistical uncertainty of $K_{DP}$), polarimetric relations produce more accurate amounts of SWE. In case of wind shear and turbulence presence in lower levels (as indicated by spectrum width), more realistic estimates of $S$ from $S(K_{DP}, Z)$ than from $S(Z)$ are usually produced within the dendritic growth layer (between the -10°C and -20°C; 80% to 90% of the precipitation is formed in DGL). This is because the highest values of $K_{DP}$ are found there due to particle non-sphericity and higher density. If the mass flux through the atmospheric column is conserved, the projection of

the $S(K_{DP}, Z)$ values from DGL to the ground would produce values in better agreement with measurements on the ground. Comparisons with standard $S(Z)$ relations (using QVP methodology) show moderate to significant improvement, affirming the applicability of the novel concept. Even when the localized averaging on the PPI data is used, e.g. the Colorado case, polarimetric relations displayed closer agreement with the ground measurements than the standard $S(Z)$ relations.

Because $S(K_{DP}, Z)$ and IWC$(K_{DP}, Z)$ exhibit very similar dependence, the principal findings of radar verification for $S(K_{DP}, Z)$ should hold to the great extent for IWC$(K_{DP}, Z)$. This notion is yet to be confirmed. Measurements of the actual IWC by the aircraft microphysical probe will be used for IWC$(K_{DP}, Z)$ verification. The sensitivity of polarimetric relations to the temperature and relative humidity change, not directly taken into account in the present study, needs to be explored. The working hypothesis is that if the polarimetric relations' multipliers depend on the crystal growth habits, the temperature and humidity will play a crucial role. Thus the inherited dependence on environmental conditions might be quantified. Practical aspects and demonstration of actual polarimetric radar snow measurements should be further explored; more snow events are needed to obtain statistical significance. Also, because of relatively unreliable snow measurements on the ground, stratiform cases with low melting layer should be used for calibration of polarimetric relations. Namely, if the mass flux is conserved in the air column, the amount of snow liquid-water equivalent directly above the melting layer should be equal to rain accumulation at the ground below if no horizontal advection occurred. The accuracy of microphysical retrievals,

complemented by the visibility in snow storms are important and could be explored using the novel concept of polarimetric snow measurements.

In summary, this study demonstrates possible improvements in remote snow measurements if radar polarimetry is engaged. Utilization of polarimetric radar measurements for snow estimation has not yet been done. This is a humble attempt to engage the meteorological community in exploration of the vast capabilities of the WSR-88D polarimetric radar network, some of which, as this one, could yield significant benefits to society.

# References


Atlas, D., S. Y. Matrosov, A. J. Heymsfield, M.-D. Chou, and D. B. Wolff, 1995: Radar and radiation properties of ice clouds. *J. Appl. Meteor.*, **34**, 2329–2345.

Atlas, D., Ulbrich, C.W., Marks, F.D., Amitai, E., Williams, C.R., 1999: Systematic variation of drop size and radar-rainfall relations. *J. Geophys. Res*., **104**, 6155–6169.

Aydin, K., and C. Tang, 1995: Estimation of ice water content with 94-GHz millimeter wave radar observables. Preprints, *27th Conf. on Radar Meteorology*, Vail, CO, Amer. Meteor. Soc., 550–552.

Bechini, R., L. Baldini, V. Chandrasekar, 2013: Polarimetric radar observations in the ice region of precipitating clouds at C-band and X-band radar frequencies. *J. Appl. Meteor. Climatol.,* **52,** 1147–1169.

Brandes, E. A., G. Zhang, and J. Vivekanandan, 2002: Experiments in rainfall estimation with a polarimetric radar in a subtropical environment. *J. Appl. Meteor.*, **41**, 674–685.
DOI: http://dx.doi.org/10.1175/1520-0450(2002)041<0674:EIREWA>2.0.CO;2

Brandes, E. A., G. Zhang, and J. Vivekanandan, 2003: An evaluation of a drop distribution-based polarimetric radar rainfall estimator. *Journal of Applied Meteorology*, **42**, 652–660.

Brandes, E. A., G. Zhang, J. Vivekanandan, 2004a: Comparison of Polarimetric Radar Drop Size Distribution Retrieval Algorithms. *J. Atmos. Oceanic Tech.*, **21**, 584-598.

Brandes, E. A., G. Zhang, J. Vivekanandan, 2004b: Drop Size Distribution Retrieval with Polarimetric Radar: Model and Application. *J. Appl. Meteor.*, **43**, 461-475.

Brandes, E. A., K. Ikeda, G. Zhang, M. Schonhuber, and R. M. Rasmussen, 2007: A statistical and physical description of hydrometeor distributions in Colorado snowstorms using a video disdrometer. *J. Appl. Meteor. Climatol.*, **46**, 634–650.

Bringi, V. N., V. Chandrasekar, J. Hubbert, E. Gorgucci, W.L. Randeu, M. Schonhuber, 2003: Raindrop Size Distribution in Different Climatic Regimes from Disdrometer and Dual-Polarized Radar Analysis. *J. Atmos. Sci.*, **60**, 354-365.

Brown, P. R. A., and P. N. Francis, 1995: Improved measurements of ice water content in cirrus using a total-water probe. *J. Atmos. Oceanic Technol.*, **12**, 410–414.

Bukovčić, P., D. Zrnić, G. Zhang, 2015: Convective–stratiform separation using video disdrometer observations in central Oklahoma – the Bayesian approach, *Atmospheric Research*, Volume **155**, 176-191, ISSN 0169-8095, http://dx.doi.org/10.1016/j.atmosres.2014.12.002.

Bukovčić, P., D. Zrnić, and G. Zhang, 2017a: Winter Precipitation Liquid-Ice Phase Transitions Revealed With Polarimetric Radar and 2DVD Observations in Central Oklahoma. *J. Appl. Meteor. Climatol*., **56**, 1345–1363. https://doi.org/10.1175/JAMC-D-16-0239.1

Bukovčić, P., A. Ryzhkov, D. Zrnić, and G. Zhang, 2017b: Polarimetric radar relations for quantification of snow based on disdrometer data. *J. Appl. Meteor.* Climatol., accepted. https://doi.org/10.1175/JAMC-D-17-0090.1

Cao, Q., Zhang, G., Brandes, E., Schuur, T., Ryzhkov, A., Ikeda, K., 2008: Analysis of video disdrometer and polarimetric radar data to characterize rain microphysics in Oklahoma. *J. Appl. Meteorol. Climatol*. **47**, 2238–2255.

Cortinas, J., 2000: A climatlogy of freezing rain in the Great Lakes region of North America. *Mon. Wea. Rev.*, **128**, 3574–3588.

Cortinas J. V. Jr., B. C. Bernstein, C. C. Robbins, J. W. Strapp, 2004: An Analysis of Freezing Rain, Freezing Drizzle, and Ice Pellets across the United States and Canada: 1976–90. *Wea. Forecasting*, **19**, 377–390.

Delanoë, J. M. E., A. J. Heymsfield, A. Protat, A. Bansemer, and R. J. Hogan, 2014: Normalized particle size distribution for remote sensing application, *J. Geophys. Res. Atmos.*, **119**, 4204–4227, doi:10.1002/2013JD020700.

Doviak, R. J., and D. S. Zrnic 1993: Doppler Radar and Weather Observations, Second edition, Dover Publications, Inc.

Fujiyoshi, Y., T. Endoh, T. Yamada, K. Tsuboki, Y. Tachibana, and G. Wakahama, 1990: Determination of a Z–R relationship for snowfall using a radar and sensitive snow gauges. *J. Appl. Meteor.*, **29**, 147–152.

Garrett, T. J., S. E. Yuter, C. Fallgatter, K. Shkurko, S. R. Rhodes, and J. L. Endries, 2015: Orientations and aspect ratios of falling snow. *Geophys. Res. Lett*., **42**, 4617–4622. doi: 10.1002/2015GL064040.

Griffin, E., T. Schuur, and A. Ryzhkov, 2017: A polarimetric analysis of ice microphysical processes in snow, using quasi-vertical profiles. Submitted to *J. Appl. Meteorol. Climatol.*

Gunn, K. L. S., and J. S. Marshall, 1958: The distribution with size of aggregate snowflakes. *J. Meteor.*, **15**, 452–461.

Gibson, S. R., and R. E. Stewart, 2007, Observations of ice pellets during a winter storm, *Atmos. Res.*, **85**, 64– 76.

Gibson, S. R., R. E. Stewart, and W. Henson, 2009: On the variation of ice pellet characteristics, *J. Geophys. Res*., **114**, D09207, doi:10.1029/2008JD011260.

Goddard, J. W. F., S. M. Cherry, V. N. Bringi, 1982: Comparison of Dual-Polarization Radar Measurements of Rain with Ground-Based Disdrometer Measurements. *J. Appl. Meteor.*, **21**, 252-256.

Hanesch, M., 1999: Fall velocity and shape of snowflakes. Ph.D. thesis, Swiss Federal Institute of Technology, Zurich, Switzerland, 123 pp. [Available online at http://e-collection.library.ethz.ch/eserv/eth:23207/eth-23207-02.pdf.]

Hendry, A., Y. Antar, and G. McCormick, 1987: On the relationship between the degree of preferred orientation in precipitation and dual-polarization radar echo characteristics. *Radio Sci*., **22**, 37 – 50.

Heymsfield, A., 1977: Precipitation development in stratiform ice clouds: A microphysical and dynamical study. *J. Atmos. Sci.*, **34**, 367–381.

Heymsfield, A., A. Bansemer, P. Field, S. Durden, J. Stith, J. Dye, W. Hall, and C. Grainger, 2002: Observations and parametrizations of particle size distributions in deep tropical cirrus and stratiform precipitating clouds: Results from in situ observations in TRMM field campaigns. *J. Atmos. Sci.*, **59**, 3457 – 3490.

Heymsfield, A., S. Matrosov, and N. Wood, 2016: Toward Improving Ice Water Content and Snow-Rate Retrievals from Radars. Part I: X and W Bands, EmphasizingCloudSat. *J. Appl. Meteor. Climatol.,* **55**, 2063–2090, doi: 10.1175/JAMC-D-15-0290.1.

Hogan, R. J., M. P. Mittermaier, and A. J. Illingworth, 2006: The retrievals of ice water content from radar reflectivity factor and temperature and its use in evaluating a mesoscale model. *J. Appl. Meteor. Climatol*., 45, 301–317, doi:10.1175/JAM2340.1.

Hogan, R., L. Tian, P. Brown, C. Westbrook, A. Heymsfield, and J. Eastment, 2012: Radar scattering from ice aggregates using the horizontally aligned oblate spheroid approximation. *J. Appl. Meteor.*, **51**, 655 – 671.

Huang, G.-J., V. N. Bringi, R. Cifelli, D. Hudak, and W. A. Petersen, 2010: A methodology to derive radar reflectivity-liquid equivalent snow rate relations using C-band radar and a 2D video disdrometer. *J. Atmos. Oceanic Technol.*, **27**, 637-651.

Huang G., V. N. Bringi, D. Moisseev, W. A. Petersen, L. Bliven, D. Hudak, 2014: Use of 2D-video disdrometer to derive mean density–size and Ze–SR relations: Four snow cases from the light precipitation validation experiment, *Atmospheric Research*, **153**, 34-48. doi:10.1016/j.atmosres.2014.07.013.

Ikeda, K., E. Brandes, G. Zhang, and S. A. Rutledge, 2005: "Observations of Winter Storms with a 2-D Video Disdrometer and Polarimetric Radar," *32nd Radar Meteorology Conference*, Albuquerque, New Mexico, 24-29 October.

Ikeda, K., E. A. Brandes, R. M. Rasmussen, 2005: NOTES AND CORRESPONDENCE: Polarimetric Radar Observation of Multiple Freezing Levels. *J. Atmos. Sci*., **62**, 3624–3636.

Islam, T., Rico-Ramirez, M. A., Thurai, M., Han, D., 2012: Characteristics of raindrop spectra as normalized gamma distribution from a Joss–Waldvogel disdrometer. *Atmos. Res*., **108**, 57–73.

Kennedy, P., and S. Rutledge, 2011: S-band dual-polarization radar observations of winter storms. *J. Appl. Meteor. Clim.,* **50,** 844-858.

Koistinen, Y., D. Michelson, H. Hohti, and M. Peura, 2003: Operational measurement of precipitation in cold climates. In Weather Radar, Principles and Advanced Applications, Ed. by P. Meischner, Springer, 78 – 114.

Korolev, A., G. Isaac, and J. Hallett, 2000: Ice particle habits in stratiform clouds. *Quart. J. Roy. Meteor. Soc.*, **126**, 2873 – 2902.

Korolev, and A., G. Isaac, 2003: Roundness and aspect ratio of particles in ice clouds. *J. Atmos. Sci.*, **60**, 1795 – 1808.

Kruger, A., and W. F. Krajewski, 2002: Two-dimensional video disdrometer: A description. *J. Atmos. Oceanic Technol.*, **19**, 602–617.

Kumjian, M. R., A. V. Ryzhkov, H. D. Reeves, and T. J. Schuur, 2013: Dual-polarization radar observations of hydrometeor refreezing in winter storms. *J. Appl. Meteor. Climatol.*, **52**, 2549–2566. doi:10.1175/JAMC-D-12-0311.1

Kumjian, M. R., and A. D. Schenkman, 2014: The curious case of ice pellets over middle Tennessee on 1 March 2014. *J. Operational Meteor.,* **2** (17), 209–213. doi: http://dx.doi.org/10.15191/nwajom.2014.0217.

Liu, C. L., and A. J. Illingworth, 2000: Toward more accurate retrievals of ice water content from radar measurements of clouds. *J. Appl. Meteor.*, **39**, 1130–1146, doi:10.1175/1520-0450(2000)039,1130:TMAROI.2.0.CO;2.

Martner, B.E., R.M. Rauber, R.M. Rasmussen, E.T. Prater, M.K. Ramamurthy, 1992: Impacts of a Destructive and Well-Observed Cross-Country Winter Storm. *Bull. Amer. Meteor. Soc.*, **73**, 169-172.

Matrosov, S., 1997: Variability of Microphysical Parameters in High-Altitude Ice Clouds: Results of the Remote Sensing Method. *J. Appl. Meteor.,* **36**, 633–648, doi: 10.1175/1520-0450-36.6.633.

Matrosov, S., 2007: Modeling Backscatter Properties of Snowfall at Millimeter Wavelengths. *J. Atmos. Sci.,* **64**, 1727–1736, doi: 10.1175/JAS3904.1.

Matrosov, S., R. Reinking, and I. Djalalova, 2005: Inferring fall attitudes of pristine dendritic crystals from polarimetric radar data. *J. Atmos. Sci*., **62**, 241 – 250.

Matrosov, S. Y., C. Campbell, D. Kingsmill, and E. Sukovich, 2009: Assessing snowfall rates from X-band radar reflectivity measurements. *J. Atmos. Oceanic Technol.*, **26**, 2324-2339.

Melnikov, V., and J. Straka, 2013: Axis ratios and flutter angles of cloud ice particles: Retrievals from radar data. *J. Atmos. Oceanic Technol*., **30**, 1691 – 1703.

Mitchell, D. L., R. Zhang, and R. L. Pitter, 1990: Mass-dimensional relationships for ice particles and the influence of riming on snowfall rates. *J. Appl. Meteor.*, **29**, 153-163.

Nagumo, N., and Y. Fujiyoshi, 2015: Microphysical Properties of Slow-Falling and Fast-Falling Ice Pellets Formed by Freezing Associated with Evaporative Cooling. *Mon. Wea. Rev.*, **143**, 4376–4392.
doi: http://dx.doi.org/10.1175/MWR-D-15-0054.1

Nešpor, V., W. F., Krajewski, and A. Kruger, 2000: Wind-induced error of raindrop size distribution measurement using a two-dimensional video disdrometer, *J. Atmos. Ocean. Tech.*, **17**, 1483–1492.

Niu, S., Jia, X., Sang, J., Liu, X., Lu, C., Liu, Y., 2010: Distributions of raindrop sizes and fall velocities in a semiarid plateau climate: convective versus stratiform rains. *J. Appl. Meteorol. Climatol*. **49**, 632–645.

Ohtake, T., and T. Henmi, 1970: Radar reflectivity of aggregated snowflakes. Preprints, *14th Conf. on Radar Meteorology, Tucson, AZ, Amer. Meteor. Soc.*, 209–210.

Puhakka, T., 1975: On the dependence of the Z–R relation on the temperature in snowfall. Preprints, *16th Conf. on Radar Meteorology, Houston, TX, Amer. Meteor. Soc.*, 504–507.

Raga, G. B., R. E. Stewart, N. R. Donaldson, 1991: Microphysical Characteristics through the Melting Region of a Midlatitude Winter Storm. *J. Atmos. Sci.*, **48**, 843-855.

Rasmussen, R., M. Dixon, S. Vasiloff, F. Hage, S. Knight, J. Vivekanandan, and M. Xu, 2003: Snow nowcasting using a real-time correlation of radar reflectivity with snow gauge accumulation. *J. Appl. Meteor.*, **42**, 20-36.

Rauber, R.M., M.K. Ramamurthy, A. Tokay, 1994: Synoptic and Mesoscale Structure of a Severe Freezing Rain Event: The St. Valentine's Day Ice Storm. *Wea. Forecasting*, **9**, 183-208.

Ryan, B., 2000: A bulk parametrization of the ice particle size distribution and the optical properties in ice clouds. *J. Atmos. Sci.,* **57**, 1436 – 1451.

Ryzhkov, A**.,** and D. Zrnic, 1998: Discrimination between rain and snow with a polarimetric radar. *Journal of Applied Meteorology*, **37**, 1228-1240.

Ryzhkov, A. V., D. S. Zrnic, and B. A. Gordon, 1998: Polarimetric Method for Ice Water Content Determination. *J. Appl. Meteor.*, **37**, 125–134. doi: http://dx.doi.org/10.1175/1520-0450(1998)037<0125:PMFIWC>2.0.CO;2

Ryzhkov, A., G. Zhang, S. Luchs, and L. Ryzhkova, 2008: Polarimetric characteristics of snow measured by radar and 2D video disdrometer. *Proc. Fifth European Conf on Radar in Meteorology and Hydrology*, Helsinki, Finland, EUMETSAT, 4 pp. [Available online at http://erad2008.fmi.fi/proceedings/extended/ erad2008-0095-extended.pdf.]

Ryzhkov, A., H. Reeves, T. Schuur, M. Kumjian, and D. Zrnic, 2011a: Investigations of polarimetric radar signatures in winter storms and their relation to aircraft icing and freezing rain. *35th Conference on Radar Meteorology*, September 25 – 30, 2011, Pittsburgh, PA.

Ryzhkov, A., M. Pinsky, A. Pokrovsky, and A. Khain, 2011b: Polarimetric radar observation operator for a cloud model with spectral microphysics. *J. Appl. Meteor. Climatol.*, **50**, 873–894.

Ryzhkov, A., P. Zhang, H. Reeves, M. Kumjian, T. Tschallener, S. Troemel, and C. Simmer, 2016: Quasi-vertical profiles - a new way to look at polarimetric radar data. *J. Atmos. Oceanic Technol.*, in press. doi:10.1175/JTECH-D-15-0020.1

Sassen, K., 1987: Ice cloud content from radar reflectivity. *J. Climate Appl. Meteor.*, **26**, 1050–1053.

Schonhuber, M., G. Lammer, and W. L. Randeu, 2008: The 2D-videodisdrometer. Precipitation: Advances in Measurement, Estimation and Prediction, S. Michaelides, Ed., Springer, 3–31.

Schuur, T., Ryzhkov, A.V., Zrnić, D. S., Schönhuber, M., 2001: Drop size distributions measured by a 2D video disdrometer: comparison with dual-polarization radar data. *J. Appl. Meteorol*. **40**, 1019–1034.

Sekhon, R. S., and R. C. Srivastava, 1970: Snow size spectra and radar reflectivity. *J. Atmos. Sci.*, **27**, 299–307.

Skofronick-Jackson, G., and Coauthors, 2015: Global Precipitation Measurement Cold Season Precipitation Experiment (GCPEX). *Bull. Amer. Meteorol. Soc*., 1719 – 1741.

Stephens, G. L., S. C. Tsay, J. P. W. Stackhouse, and P. Flatau, 1990: The relevance of the microphysical and radiative properties of cirrus clouds to climate and climatic feedback. *J. Atmos. Sci.*, **47**, 1742–1753.

Stewart, R. E., 1992: Precipitation types in the transition region of winter storms. *Bull. Amer. Meteor. Soc.*, **73**, 287–296.

Szyrmer, W., and I. Zawadzki, 2010: Snow studies. Part II: Average relationship between mass of snowflakes and their terminal fall velocity. *J. Atmos. Sci.*, **67**, 3319 – 3335.

Tao, W.-K., Lang, S., Zeng, X., Shige, S., Takayabu, Y., 2010: Relating convective and stratiform rain to latent heating. *J. Clim*. **23**, 1874–1893.

Thurai, M., G. J. Huang, V. N. Bringi, W. L. Randeu, and M. Schönhuber, 2007: Drop Shapes, Model Comparisons, and Calculations of Polarimetric Radar Parameters in Rain. J. *Atmos. Oceanic Technol*., **24**, 1019–1032.

Thurai, M., Williams, C. R., Bringi, V. N., 2014: Examining the correlations between drop size distribution parameters using data from two side-by-side 2D-video disdrometers. *Atmos. Res*. **144**, 95–110.

Tiira, J., D. N. Moisseev, A. von Lerber, D. Ori, A. Tokay, L. F. Bliven, and W. Petersen, 2016: Ensemble mean density and its connection to other microphysical properties of falling snow as observed in Southern Finland, *Atmos. Meas. Tech.*, **9**, 4825-4841, doi:10.5194/amt-9-4825-2016.

Tokay, A., Short, D. A., 1996: Evidence from tropical raindrop spectra of the origin of rain from stratiform versus convective clouds. *J. Appl. Meteorol*. **35**, 355–371.

Trapp, R. J., D. M. Schultz, A.V. Ryzhkov, R. L. Holle, 2001: Multiscale Structure and Evolution of an Oklahoma Winter Precipitation Event. *Mon. Wea. Rev.*, **129**, 486-501.

Ulbrich, C. W., 1983: Natural Variations in the Analytical Form of the Raindrop Size Distribution. *J. Appl. Meteor.*, **22**, 1764-1775.

Van de Hulst, H., 1981: *Light Scattering by Small Particles*. Dover, 470 pp.

Vasiloff, S.V., 1997: Interpretation of radar data during snow events in mountainous terrain. WR Tech. Attachment TA97 -35.

Vivekanandan, J., V. N. Bringi, M. Hagen, and P. Meischner, 1994: Polarimetric radar studies of atmospheric ice particles. *IEEE Trans. Geosci. Remote Sens.*, **32**, 1–10.

Williams, C. R., Bringi, V. N., Carey, L. D., Chandrasekar, V., Gatlin, P. N., Haddad, Z. S., Meneghini, R., Munchak, S. J., Nesbitt, S. W., Petersen, W. A., Tanelli, S., Tokay, A.,Wilson, A.,Wolff, D. B., 2014: Describing the shape of raindrop size distributions using uncorrelated raindrop mass spectrum parameters. *J. Appl. Meteorol. Climatol*. **53**, 1282–1296.

Wolfe, J.P., and J.R.Snider, 2012: A Relationship between Reflectivity and Snow Rate for a High-Altitude S-Band Radar, *J. Appl. Meteor. Climatol.*, 51, 1111–1128.

Wolfe, J.P., and J.R.Snider, 2013: Reply to comments on "A Relationship between Reflectivity and Snow Rate for a High-Altitude S-Band Radar", *J. Appl. Meteor. Climatol.*, 730-731.

Yuter, S. E., D. E. Kingsmill, L. B. Nance, M. Loffler-Mang, 2006: Observations of Precipitation Size and Fall Speed Characteristics within Coexisting Rain and Wet Snow. *J. Appl. Meteor.*, **45**, 1450-1464.

Yuter, S. E., D. A. Stark, M. T. Bryant, B. A. Colle, L. B. Perry, J. Blaes, J. Wolfe, and Gerhard Peters, 2008: Forecasting and characterization of mixed precipitation events using the MicroRainRadar. *Preprints, 5th European Conference on Radar in Meteorology and Hydrology.* 30 June – 4 July 2008, Helsinki, Finland.

Zawadzki, I., W. Szyrmer, C. Bell, and F. Fabry, 2005: Modeling of the melting layer. Part III: The density effect. *J. Atmos. Sci.*, **62**, 3705 – 3723.

Zawadzki, I., E. Jung, G. Lee, 2010: Snow studies. Part I: A study of natural variability of snow terminal velocity. *J. Atmos. Sci.,* **67**, 1591 – 1604.

Zerr, R., 1997: Freezing rain: An observational and theoretical study. *J. Appl. Meteor.*, **36**, 1647-1661.

Zhang, G., J. Vivekanandan, E. Brandes, 2001: A Method for Estimating Rain Rate and Drop Size Distribution from Polarimetric Radar Measurements. *IEEE Transactions on Geoscience and Remote Sensing*, **39**, 830-841.

Zhang, G., Vivekanandan, J., Brandes, E., Meneghini, R., Kozu, T., 2003: The shape–slope relation in observed gamma raindrop size distributions: statistical error or useful information? *J. Atmos. Ocean*. Technol. **20**, 1106–1119.

Zhang, G., Sun, J., Brandes, E.A., 2006: Improving parameterization of rain microphysics with disdrometer and radar observations. *J. Atmos. Sci*. **63**, 1273–1290.

Zhang, G., M. Xue, Q. Cao, and D. Dawson, 2008: Diagnosing the Intercept Parameter for Exponential Raindrop Size Distribution Based on Video Disdrometer Observations: Model Development. *J. Appl. Meteor. Climatol.*, **47**, 2983–2992. doi: http://dx.doi.org/10.1175/2008JAMC1876.1

Zhang, G., S. Luchs, A. Ryzhkov, M. Xue, L. Ryzhkova, and Q. Cao, 2011: Winter Precipitation Microphysics Characterized by Polarimetric Radar and Video Disdrometer Observations in Central Oklahoma. *J. Appl. Meteor. Climatol.*, **50**, 1558–1570. doi: http://dx.doi.org/10.1175/2011JAMC2343.1

Zhang, G., 2016: *Weather Radar Polarimetry*, CRC Press, Boca Raton, FL, pp. 304.

# Appendix: Theoretical Relations

The theoretical $S(Z)$ relation is derived following Rasmussen et al. (2003). The magnitude of $S$ is

$$S = 0.6\,10^{-3}\pi \int_0^{D_{\max}} \frac{\rho_s(D)}{\rho_w} D^3 U_t^{(s)}(D) N(D) dD \tag{A1}$$

where $\rho_w$ and $\rho_s(D)$ are the densities of water and snow expressed in g cm$^{-3}$, $U_t^{(s)}$ is the terminal velocity of snowflakes (m s$^{-1}$), $N(D)$ is the size distribution of snowflakes (m$^{-3}$ mm$^{-1}$), and $D$ is the equivolume diameter in mm. We assume that the density of dry snow decreases with diameter $D$ and degree of riming $f_{rim}$ as specified by Brandes et al. (2007) and Zawadzki et al. (2005),

$$\rho_s(D) = c_\rho f_{rim} D^{-0.922} \text{ (g cm}^{-3}\text{)}. \tag{A2}$$

The $f_{rim}$ changes from 1 for unrimed snow to 5 for heavily rimed snow. According to Zawadzki et al. (2005, 2010), the terminal velocity of snowflakes can be approximated by

$$U_t^{(s)} = a_u f_{rim}^{1/3} D^{0.18}, \tag{A3}$$

where $a_u$ is a function of the temperature $T_s$ at the location of snow and its distance from the cloud top $H_{st}$:

$$a_u = 0.73 + 0.037 H_{st} + 0.011 T_s. \tag{A4}$$

In (A3) and (A4), $D$ is in mm, $U_t^{(s)}$ is in m s$^{-1}$, $H_{st}$ is in km, and $T_s$ is in °C.

The theoretical relation between $Z$ and IWC can be derived starting from the equation for

$$\text{IWC} = \frac{\pi}{6} 10^{-3} \int_0^{D_{\max}} \rho_s(D) D^3(D) N(D) dD. \tag{A5}$$

In (A5), IWC is expressed in g $m^{-3}$.

Size distributions of snowflakes can be well approximated by

$$N(D) = N_{0s} \exp(-\Lambda_s D), \tag{A6}$$

where the slope $\Lambda_s$ usually varies between 1 and 10 $mm^{-1}$ (e.g., Ryan 2000; Heymsfield et al. 2002). The maximal size of dry snowflakes $D_{max}$ commonly changes from 1 to 10 mm and is related to the slope $\Lambda_s$ (Heymsfield et al. 2002):

$$D_{max} = 11.6\, \Lambda_s^{-0.91}, \tag{A7}$$

where $D_{max}$ is in mm and $\Lambda_s$ is in $mm^{-1}$. With such dependence of $D_{max}$ on $\Lambda_s$ integration over size spectrum in (A1) and (A5) between 0 and $\infty$ yields the following expression for $S$ and IWC:

$$S = 3.36 \times 10^{-4} \frac{a_u f_{rim}^{4/3} N_{0s}}{\rho_w} \int_0^\infty D^{2.26} \exp(-\Lambda_s D) dD = 3.36 \times 10^{-4} \frac{a_u f_{rim}^{4/3} N_{0s} \Gamma(3.26)}{\rho_w \Lambda_s^{3.26}}, \tag{A8}$$

and,

$$\mathrm{IWC} = 9.315 \times 10^{-5} f_{rim} N_{0s} \int_0^\infty D^{2.08} \exp(-\Lambda_s D) dD = 9.315 \times 10^{-5} \frac{f_{rim} N_{0s} \Gamma(3.078)}{\Lambda_s^{3.078}}. \tag{A9}$$

These equations simplify to

$$S = 8.65 \times 10^{-4} \frac{a_u f_{rim}^{4/3} N_{0s}}{\Lambda_s^{3.26}}, \text{ and} \tag{A10}$$

$$\mathrm{IWC} = 2 \times 10^{-4} \frac{f_{rim} N_{0s}}{\Lambda_s^{3.08}}. \tag{A11}$$

Here, $S$ is in mm $h^{-1}$, IWC is in g $m^{-3}$, $\Lambda_s$ is in $mm^{-1}$, and $N_{0s}$ is in $m^{-3}mm^{-1}$.

Following Eq. (3.12) and assuming spherical shape of snowflakes (the spheres are used to roughly estimate the exponent and for quick comparison with other relations), radar reflectivity of dry snow can be expressed by

$$Z = \frac{4\lambda^4}{\pi^4 \mid K_{\mathrm{w}} \mid^2} \int_0^{\infty} \mid s_{\mathrm{a}}^{(\pi)} \mid^2 N(D) dD \,. \tag{A12}$$

In the Rayleigh approximation,

$$s_{\mathrm{a}}^{(\pi)} = \frac{\pi^2 D^3}{2\lambda^2} \frac{\varepsilon_{\mathrm{s}} - 1}{\varepsilon_{\mathrm{s}} + 2}, \tag{A13}$$

where $\varepsilon_{\mathrm{s}}$ is the dielectric constant of snow. If snow density is relatively low then

$$\frac{\varepsilon_{\mathrm{s}} - 1}{\varepsilon_{\mathrm{s}} + 2} = \frac{\rho_{\mathrm{s}}(D)}{\rho_{\mathrm{i}}} \frac{\varepsilon_{\mathrm{i}} - 1}{\varepsilon_{\mathrm{i}} + 2} \quad \text{(Debye formula)} \tag{A14}$$

and the equation for $Z$ can be rewritten as

$$Z = \frac{\mid K_{\mathrm{i}} \mid^2}{\mid K_{\mathrm{w}} \mid^2} \int_0^{D_{\max}} \frac{\rho_{\mathrm{s}}^2(D)}{\rho_{\mathrm{i}}^2} D^6 N(D) dD, \tag{A15}$$

where $K_{\mathrm{i}} = (\varepsilon_{\mathrm{i}} - 1)/(\varepsilon_{\mathrm{i}} + 2)$, $K_{\mathrm{w}} = (\varepsilon_{\mathrm{w}} - 1)/(\varepsilon_{\mathrm{w}} + 2)$, $\varepsilon_{\mathrm{i}}$ and $\varepsilon_{\mathrm{w}}$ are dielectric constants of solid ice and water respectively and $\rho_{\mathrm{i}} = 0.917$ g cm$^{-3}$ is the density of solid ice. Using (A2) and (A6) and substituting upper limit of integration $D_{\max}$ with infinity (similar to derivation of $S$) one obtains

$$Z = 0.219 \frac{f_{\mathrm{rim}}^2 N_{0\mathrm{s}}}{\Lambda_{\mathrm{s}}^{5.16}}. \tag{A16}$$

In (A16), $Z$ is in mm$^6$m$^{-3}$. The $S(Z)$ relation follows from (A10) and (A16) and is

$$S = 2.26 \times 10^{-3} a_{\mathrm{u}} f_{\mathrm{rim}}^{0.07} N_{0\mathrm{s}}^{0.37} Z^{0.63}, \tag{A17}$$

whereas the IWC($Z$) is obtained from (A11) and (A16) and it is

$$\mathrm{IWC} = 4.95 \times 10^{-4} f_{\mathrm{rim}}^{-0.19} N_{0\mathrm{s}}^{0.4} Z^{0.6}. \tag{A18}$$

It follows from (A17) and (A18) that the coefficients $a_{\mathrm{s}}$ and $c_{\mathrm{s}}$ in the relations $S = a_{\mathrm{s}} Z^{b_{\mathrm{s}}}$, and $\mathrm{IWC} = c_{\mathrm{s}} Z^{d_{\mathrm{s}}}$, are almost entirely dependent on the intercept of the

exponential size distribution $N_{0s}$. The coefficient $a_s$ is practically insensitive to the degree of snow riming $f_{rim}$ whereas, $c_s$ is marginally sensitive to $f_{rim}$. Indeed, a change of $f_{rim}$ from 1 to 5 causes only an 11% increase in $a_s$ and 27% decrease in $c_s$. The inversion of (A17) and (A18), $Z(S)$ and $Z(\mathrm{IWC})$, often used in practical applications can be written as

$$Z(S) = 1.52 \times 10^4 a_u^{-1.58} N_{0s}^{-0.58} S^{1.58}, \tag{A19}$$

and,

$$Z(\mathrm{IWC}) = 686.3\, f_{rim}^{0.32} N_{0s}^{-0.68} \mathrm{IWC}^{1.68}. \tag{A20}$$

Eq. (A18) is consistent with the relation between IWC, $Z$, and $N_{0s}$ that was empirically derived by Delanoë et al. (2014) using very large dataset of in situ aircraft measurements of ice

$$\mathrm{IWC} = 2.36 \times 10^{-4} N_{0s}^{0.42} Z^{0.58}. \tag{A21}$$

Similar to the radar reflectivity factor, specific differential phase

$$K_{DP} = \frac{0.18\lambda}{\pi} r \int_0^\infty \mathrm{Re}(s_a^{(0)} - s_b^{(0)}) N(D) dD \tag{A22}$$

in snow can be obtained as a function of the parameters of the snow size distributions ($N_{0s}$ and $\Lambda_s$) and the factors characterizing snowflake shapes and orientations. In the Rayleigh approximation,

$$s_a^{(0)} - s_b^{(0)} = \frac{\pi^2 D^3}{6\lambda^2} \left( \frac{\varepsilon_s - 1}{L_a(\varepsilon_s - 1) + 1} - \frac{\varepsilon_s - 1}{L_b(\varepsilon_s - 1) + 1} \right). \tag{A23}$$

For snow with low density, the magnitude of dielectric constant of snow $\varepsilon_s$ is very close to 1 and $L_{a,b}|\varepsilon_s - 1| << 1$, therefore,

$$\frac{\varepsilon_s - 1}{L_a(\varepsilon_s - 1) + 1} - \frac{\varepsilon_s - 1}{L_b(\varepsilon_s - 1) + 1} \approx (\varepsilon_s - 1)^2 (L_b - L_a) = 9 \frac{\rho_s^2}{\rho_i^2} \left( \frac{\varepsilon_i - 1}{\varepsilon_i + 2} \right)^2 (L_b - L_a). \quad \text{(A24)}$$

This yields the following equation for $K_{DP}$:

$$K_{DP} = \frac{0.27\pi r}{\lambda \rho_i^2} \left( \frac{\varepsilon_i - 1}{\varepsilon_i + 2} \right)^2 \int_0^\infty (L_b - L_a) \rho_s^2(D) D^3 N(D) dD \quad \text{(A25)}$$

which can be further simplified after integration if exponential size distribution (A6) is assumed:

$$K_{DP} = 0.192 \frac{c_\rho^2 f_{rim}^2 r (L_b - L_a) N_{0s}}{\lambda \, \Lambda_s^{2.16}}. \quad \text{(A26)}$$

Eq. (A26) shows that similarly to $Z$, $K_{DP}$ is proportional to the product of $f_{rim}^2 N_{0s}$ but also strongly depends on the shape of snowflakes represented by the factor $L_b - L_a$ and the width of the canting angle distribution $\sigma$ through the factor $r = \exp(-2\sigma^2)$.

Due to the inverse dependence of snow density on equivolume diameter, radar reflectivity factor is close to the fourth moment of snow size distribution whereas specific differential phase is close to its first moment if snow is aggregated and has low density. Note that for pristine crystals with high density which do not exhibit strong size dependence, $Z$ is still close to the sixth moment and $K_{DP}$ to the third moment of size distributions. In other words, $K_{DP}$ is directly proportional to ice water content for pristine and lightly aggregated crystals as claimed by Vivekanandan et al. (1994) and Ryzhkov et al. (1998).